

SCANNING PROBE STUDIES OF THE PILUS NANOWIRES IN *GEOBACTER*
SULFURREDUCTENS

By

Joshua P. Veazey

A DISSERTATION

Submitted to
Michigan State University
in partial fulfillment of the requirements
for the degree of

DOCTOR OF PHILOSOPHY

Physics

2011

ABSTRACT

SCANNING PROBE STUDIES OF THE PILUS NANOWIRES IN *GEOBACTER SULFURREDUCTENS*

By

Joshua P. Veazey

In microbial organisms like bacteria, pili (singular: pilus) are filament-like appendages that are nanometers in diameter and microns long. The sizes and structures of the different types of pili found in nature are adapted to serve one of many distinct functions for the organism from which they come. The pili expressed by the bacterium *Geobacter sulfurreducens* act as electrically conductive nanowires that provide conduits for electrons to leave the cell during its respiratory cycle. Biological experiments have suggested that long range electron transfer across micron distances may proceed along the protein matrix, rather than by metal cofactors (metal atoms bound to the protein). Protein conductivity across such distances would require a novel transport mechanism. In an effort to elucidate this mechanism, our lab has used two electronically sensitive scanning probe techniques: Scanning Tunneling Microscopy (STM) and Conductive Probe Atomic Force Microscopy (CP-AFM).

I employed the high resolution imaging and electronic sensitivity of STM to resolve the molecular sub-structure and local electronic density of states (LDOS) at different points above pili from purified preparations, deposited onto a conducting substrate. The significant and stable tunneling currents achieved for biologically relevant voltages, in the absence of metal cofactors, demonstrated conduction between tip and substrate via the protein matrix. We observed periodicity of roughly 10 nm and 2.5 nm in topographs of the pili. In our acquisition of LDOS, we observed gap-like asymmetric energy spectra that were dependent upon the location of the tip above the pilus, suggestive of easier current flow out of one

side of the cylindrical pilus and into the opposite side. Voltage-dependent STM imaging, which also contains information about the LDOS at each pixel, was consistent with this interpretation. The asymmetry in spectra observed on one pilus edge had a slightly larger magnitude than the other edge, by a factor of 1.3. The width of the gap-like feature was roughly 1 V.

For direct observation of the long range electron transport, we developed a method whereby a conductive AFM tip measured current flowing to a surface electrode via the longitudinal axis of a deposited pilus. These samples also lacked embedded metal atoms. We achieved a proof-of-principle measurement of conductivity across a 200 nm distance. The upper bound of the resistance at this distance was 40 M Ω , suggesting a preliminary upper bound on the longitudinal resistivity of 0.4 Ω -cm, comparable to that of the basal plan of graphite. I will place these results in context with continuing work in our lab to optimize the protocols for reproducible deposition quality on the electrodes.

Copyright by
JOSHUA P. VEAZEY
2011

For Mom, Dad, Kim, Kass, and Chris.

ACKNOWLEDGMENT

This work was graciously supported by a Strategic Partnership Grant from the Michigan State University Foundation, as well as a grant from the National Science Foundation (MCB-1021948).

I would like to express my sincere gratitude to the numerous individuals who provided support for this work and for my education. I only have room here to address a few of them in particular.

First, I am thankful to my advisor Stuart Tessmer, who has provided both endless encouragement and ample room to work and make my own mistakes. Not only did I learn a great deal scientifically, but I also learned by observing many of his invaluable soft skills (humility, communication, etc.), of which I had very little when I started. He is a wonderful teacher and excellent burger chef. I am also very grateful to Gemma Reguera, a creative thinker and talented researcher, who was at times like a second advisor. I learned more from her than I ever expected in the beginning. I cannot close this opening nod to advisors without acknowledging Sanela Lampa-Pastirk, my friend and mentor who will probably deny the incredible amount she taught me about biology, chemistry, science, and life. Even aside from her scientific contributions, I would not have made it to this point without her.

I am also very thankful for the friendliness and support I received from my colleagues in the lab and in our collaborations. Professor Mark Worden's curiosity and intellect were always a pleasure at SPG meetings. Cemil Kayis and Aleksandra Tomic were very generous in spending time teaching me STM. Aleksandra allowed me to observe and participate in some of her final data runs. Likewise, thank you to the other great individuals with whom I

worked: Irma Kuljanishvili, Morewell Gasseller, Megan Romanowich, Matt DeNinno, Kathy Walsh, Mike Manzella, Becky Steidl, Allison Speers, Dena Cologgi, Jenna Young, Blair Bullard, Prof. Kaz Kashefi, and Angelines Castro. I have also worked with some talented undergraduate students who had the power to challenge my assumptions and teach me a great deal. Jessie Muir worked very hard with me in the early days of the pili and artifacts studies. John Raguse involuntarily taught me effective inquiry and networking skills. I also had valuable interaction with Sean Wagner, John Claybrook (NC State), and Kerry Sisson (Hartwick).

Thanks to Professor Mahanti and Zsolt Rak for their collaboration in studying CeTe_3 , and to Professor Zhang and Jiebing Sun for their collaboration in CP-AFM measurements of the pili. Thank you to fellow graduate students Eric Gingrich and Yixing Wang, both of whom have immense teaching and scientific talent, which they employed to help me quickly learn basic photolithography skills just over one year ago. Thank you also to those who helped so much by reading and commenting on various versions of this manuscript: Stuart, Gemma, Sanela, Mike, and Caroline.

Our physics department is lucky to have such great faculty and staff who enrich research and teaching. The hard work of Reza Loloee, Baokang Bi, and Mark Olsen keeps us afloat. Also, Debbie Barratt and Kim Crosslan have been sources of endless support for me and other students.

I would like to thank a few of my peer mentors that helped me make it through so many difficult intellectual and personal challenges: Megan McCullen, Josh Savory, Jon DeLauter, Harold Barry, Micha Kilburn, Dan Brown, Steve Waldauer, Caroline Martin, Allison Powers, and the very lovely Hilary Schmid. Hilary's support and patience have not ceased to

dumbfound me.

I wish to give special thanks to Professor Dan Watson at the University of Rochester for being a fantastic mentor even to this day. His equally impressive gifts of teaching and research are unmatched. When I was second semester junior undergraduate who had no idea how to start a research career, he gave me a position in his lab and never acted like I was anything less than qualified. While I worked there, Mike Thomas taught me how to have fun in the lab.

Finally, thank you to Dan Grosso. He set aside three weeks of his high school Algebra II class that I took from him in 1998 to teach basic algebra and factoring to me and 30 other students who were supposedly in an advanced math trajectory. With this and his talented teaching throughout the year, he prevented a class of enthusiastic math students from falling through the cracks. Without him, these pages may very well not exist.

PREFACE

The interdisciplinary nature of my main research project turned out to be an effective means through which I learned values critical to conducting research of any kind. Humility, the most important of these values, proves extremely important when working with those from different backgrounds. Colleagues with training in different disciplines not only have different knowledge sets, but they also often have different perspectives. For example, while I initially understood the pilus nanowires as proteinaceous analogues of carbon nanotubes, someone with a training in microbiology may have seen them as large structures built from smaller proteins to extend the spatial reach of a cell's energy transduction. While both are accurate, the different perspectives define how data are interpreted and even the proposal for how data are initially sought. Only a synergistic interdisciplinary effort has the capacity to fully understand such a complicated object. The physicist interpreting the electronic energy spectrum of this apparent proteinaceous nanotube must accept that it does not necessarily obey the systemic bulk simplifications that have been successful in other solid state systems. Likewise, the biologist must be open to incorporating, if appropriate, adaptations of those systemic simplifications to models for energy transduction that apply to smaller molecules. Where we demonstrated humility, we succeeded.

The value of humility does not necessitate that one constantly bend and break, but rather it necessitates constant self-evaluation so that one is aware when opinions influenced by gut-feelings, rather than science, drive the investigative process. This does not preclude attention to one's tacit knowledge, for the examined scientific life should learn to distinguish such insight from closed mindedness. In this way, it is the scientific rigor that can drive

one's work rather than stubbornness or simple arrogance. Physicists seem to be particularly susceptible to this arrogance, perhaps due to the substantial quantitative rigor of their disciplines.

As role models, I chose physicists who seemed not to suffer from this trap, such as my advisor, Stuart. Unintended lessons on humility were perhaps the most valuable I learned. Humility should prove important as I strive to keep an open mind in future scientific endeavors—even those that may not necessarily involve interdisciplinarity.

TABLE OF CONTENTS

List of Figures	xiv
1 Introduction	1
2 Scanning Probe Microscopy	7
2.1 Scanning Tunneling Microscopy Theory	8
2.1.1 Tunneling Current: Perturbation Theory	14
2.1.2 Imaging	16
Spatial Resolution	16
Voltage-dependent Imaging	17
Imaging Summary	18
2.1.3 Spectroscopy	19
Normalization	21
Energy resolution at finite temperature	22
2.2 Practical considerations for STM	22
2.2.1 Tip material and fabrication	22
2.2.2 Imaging of large adsorbates with STM	23
2.2.3 Multi-tip artifacts	25
2.2.4 Vibration isolation	26
2.3 STM Experimental Setup	28
2.3.1 Nanosurf Easyscan STM	29
2.3.2 Besocke style cryogenic STM	32
High Vacuum Chamber	34
2.3.3 Preamp and Feedback loop	35
2.4 Atomic Force Microscopy	36
2.4.1 Modes of Imaging	38
Tapping Mode	40
2.4.2 Conductive Probe AFM	41
3 <i>Geobacter sulfurreducens</i>	42
3.1 Elementary cell respiration	43
3.2 <i>G. sulfurreducens</i> respiration	44
3.3 A primer on protein structure	46
3.4 Possible mechanisms of electron transfer	47
3.4.1 The structure of <i>G. sulfurreducens</i> pili	49
3.4.2 Electron transfer in metalloproteins	49
3.4.3 Electron transfer in protein matrix	50

3.4.4	Experimental potential	54
4	Filament-like artifacts on graphite	56
4.1	Materials & Methods	58
	Experimental Procedure	58
4.2	Common artifacts	59
4.3	Fiber Artifact	63
4.4	Zipper Artifact	67
4.5	Conclusions	70
5	STM study of pilus nanowire electronic properties	72
5.1	Materials & Methods	73
	5.1.1 STM and AFM Measurements	73
	5.1.2 Sample Preparation	74
	Growth and Deposition	74
	Substrate	78
5.2	Pilus Imaging	80
	5.2.1 Analysis of observed structure	81
5.3	Voltage-dependent Imaging	83
5.4	Point Spectroscopy	85
5.5	PAK Pilus Negative Control	90
5.6	Discussion	94
	Topographic structures	95
	Electronic structures	96
6	CP-AFM study of pilus long distance electron transfer	98
6.1	Materials & Methods	100
6.2	Preliminary Results	101
	6.2.1 Native oxide substrate	101
	6.2.2 Thermal oxide substrate	103
6.3	Discussion and Future Directions	105
7	Conclusions	107
	Future Directions	110
Appendix A Tip-adsorbate distortions		115
Appendix B AFM characterization of pilus height		120
Appendix C Subsurface atom contribution to tunneling current in CeTe₃		122
C.1	Materials and Methods	123
	C.1.1 Cryogenic operation of Besocke STM	125
C.2	Results and Discussion	126

C.2.1	Secondary square lattice	129
References	135

LIST OF FIGURES

1.1	Transmission electron micrograph of <i>Geobacter sulfurreducens</i> cell expressing visible pilus nanowires. The lead author on the study that produced this image was our collaborator, Gemma Reguera. Scale bars are 200 nm. (Adapted by permission from Macmillan Publishers Ltd: NATURE (nature.com/nature) [1], copyright 2005).	3
2.1	Schematic for the STM experimental setup. A voltage is applied between a sharp metallic tip and surface as they are brought to within angstroms of each other. At this distance scale, a small tunneling current flows. Scanning of the tip proceeds by applying appropriate superposition of voltages to each of the four quadrants of the piezoelectric scanning tube. (Creative Commons Attribution ShareAlike 2.0 Austria License, Authors Michael Schmid and Grzegorz Pietrzak) For interpretation of the references to color in this and all other figures, the reader is referred to the electronic version of this dissertation.	9
2.2	One-dimensional approximation of the tunnel junction. (a) Energy diagram of the one dimensional tip-vacuum-sample configuration with an applied voltage, corresponding to the energy difference eV . Dashed lines denote the locations of the electron energy, $\epsilon = E - E_F$, and the average barrier height, U . An electron wave function ψ is superimposed. (b) Cartoon of the states probed in STM. Depending on the polarity of the applied voltage, either unoccupied or occupied states of the sample are probed.	11
2.3	(a) Atomically resolved carbon atoms from the surface of graphite. The image had minimal processing. The color scale of each line was set to the same average value, but there was no smoothing of adjacent pixels. (b) I - V and dI/dV curves obtained on the surface near the area imaged in (a). The dI/dV curve is characteristic of the surface density of states for HOPG. ($I=250$ pA; $V=50$ mV)	13
2.4	Example from the literature of voltage-dependent real space STM imaging of the surface of Si(111)-(7x7) [2]. The left and right images were taken at opposite polarities.	19

2.5	Examples of geometric distortions due to finite tip geometry. (a) Filament (black) of diameter D is broadened when scanning with a tip of finite radius R_{eff} , which includes the tunneling gap width. (b) Broadening of a step edge due to finite tip radius. L is the apparent length over which the step edge rises. This may be used to quantify the effective tip radius.	24
2.6	Cartoon of a multitip imaging artifact, in this case a double tip. For imaging of a flat surface and adsorbates with short height, only one tip images, resulting in the predicted topograph. (b) For a larger adsorbate protruding high enough for the second tip to image, the topograph shows the adsorbate imaged twice.	26
2.7	Schematic of the Nanosurf Easyscan STM design out of the box and with vibration isolation in our lab. The compact size and stability allow convenience and high resolution.	30
2.8	Schematic of the homemade Besocke-style STM in our lab and vibration isolation scheme. The design is mechanically and thermally stable. It possesses a larger scan range and much less thermal drift than the x - y - z block design. Our scan head may be mounted on the end of a long stick and advanced to the center of a helium-3 refrigerator under high vacuum.	33
2.9	Basic schematic of an atomic force microscope having a laser-reflected detection mechanism.	37
2.10	(a) Sketch of the potential versus distance between the AFM cantilever and sample surface. Depending on mode, the microscope may be operated at $z > z^*$ (non-contact mode); $z < z^*$, $U > 0$ (contact mode); $z < z^*$, $U < 0$ (tapping mode). (b) Sketch of cantilever deflection and phase as a function of frequency. Amplitude deflection mode (Point 1) is operated slightly off resonance so that the direction of deflection may be detected. Frequency modulation (Point 2) and phase modulation modes are operated on resonance.	40
3.1	Simplified cartoon of the electron transport chain in <i>Geobacter sulfurreducens</i> . Establishment of proton gradient for ATP production results in shuttling of electrons outside the cell through a series of metalloproteins and quinones in the periplasm. The terminal electron acceptor, in this case Fe(III), accepts an electron from either an outer membrane bound cytochrome or the electronically conductive pilus.	45

3.2	Hierarchy of protein structure. (a) Primary structure consisting of a linear polymer of amino acids. Highlighted is tyrosine, which has an aromatic side chain. (b) An example of secondary structure, in this case an α -helix. An atomic stick model is superposed with the ribbon representation. (c) Examples of tertiary structure. PAK pilin subunit (upper) and horse heart cytochrome C (lower). (d) Quaternary structure. Pictured here is the PAK pilus, assembled from multiple pilin subunits. (Part (d): Adapted by permission from Macmillan Publishers Ltd: NATURE REVIEWS MICROBIOLOGY (nature.com/nrmicro) [3], copyright 2004)	48
3.3	Schematic of two-site biological electron transfer reactions in the form of a double-well electronic potential. Upper: symmetric; Lower: asymmetric. . .	52
4.1	(a) STM topograph of a rough step edge. As evident in the profile in (b), the edge is several layers in height. To produce the plot, a best fit line in the direction of the cut was subtracted to correct for the background slope. This subtraction makes the step edge easier to identify. A cartoon of the step edge is also shown in (b). (c)-(e) Grain boundaries on HOPG. (c) Representative topograph of grain boundaries encountered during our studies. (d) Grain boundary resembling that in (c) [4]. (e) Atomic resolution topograph of the same grain boundary at the location of the box in (d). (inset): Lattice planes at shifted angles superimposed over a simulated STM image for a grain boundary.	60
4.2	Series of STM topographs of buckled graphite sheets. (a) and (b) are examples of these oft-observed filament-like features. (c)-(e) One particular buckle examined in more detail. (d) Buckle cartoon and profile taken at the location of the line cut denoted in (e). (e) Atomic resolution topographs of the buckle. The inset is sized to scale and is placed at the approximate location at which it was taken subsequently at higher resolution.	62
4.3	Series of scanning tunneling microscopy topographs of a region of the HOPG surface having disturbed graphite sheets ($V=-400$ mV, $I=-50$ pA). STM image taken before (a) and immediately after (b) the tip pushed one of the fibers across the surface (denoted by arrows). Both (c) and (d) were taken in the vicinity of the region in (a) and (b). (c) Higher resolution STM topograph of filament junctions. The sharp angles and rigid structure are more characteristic of HOPG artifacts than biological material. (d) Another high resolution topograph. The structure follows or originates from the step edge.	64

4.4	STM topographs of fibrous artifacts on the surface of HOPG. (a) High resolution image of an artifact observed on the surface of an inoculated and fixed sample in the same region shown in Figure 4.3 ($V=-400$ mV, $I=-60$ pA). The line denotes the location of the profile plotted in (b). A multi-tip effect may be contributing to the observed width of ~ 80 nm. (c) Representative normalized $I-V$ spectroscopy curves. Each is an average of ~ 40 curves with 13-point S-G smoothing. The darker line is a curve taken on the section of the fiber marked in (a). The lighter line is an $I-V$ curve of the flat HOPG next to the filament. The two curves do not have any distinguishable differences. (d) STM topograph of a similar artifact observed on the surface of a bare freshly cleaved graphite control sample ($V=50$ mV, $I=1$ nA).	66
4.5	STM topograph of a zipper structure. The box in (a) denotes the region scanned in (b) and (c) ($V=1$ V, $I=100$ pA). The structure appears different in (b) and (c), presumably due to changes in the tip configuration while scanning. This structure was observed just once, and due to its rarity, it has not been observed on HOPG controls that were bare or exposed to solvents only. It also does not resemble the <i>G. sulfurreducens</i> pilus nanowires that we have observed on multiple inoculated samples (e.g. Chapter 5). The object appears to be pinned to a step edge and is straight and rigid, in contrast to the observed appearance of the pili.	69
5.1	Schematic for deposition of samples in STM study of (a) cells and pili and (b) purified pili.	75
5.2	(a) Atomic force microscopy image of cells expressing pili deposited onto the surface of HOPG. The white box indicates the nominal maximum scan range of the STM. An increase in density of pili comes with increase in debris and cells. For reference, an STM topograph of a sample prepared in a similar way is also shown. A double tip, which often developed while scanning these dirty samples, complicates the interpretation ($V=900$ mV; $I=70$ pA). (b) AFM image of purified pili deposited at high concentration onto the surface of HOPG. With purified pili, we may exert much more control over the concentration and achieve sub-monolayer coverage for use in STM, as shown in (c). Both (b) and (c) are the same scan size as the maximum scan range of the STM.	77
5.3	(a) STM topograph of a pilus from purified pili sample. (b) Axial (black) and transverse (grey) line profiles obtained for the same image at the locations marked in the inset. Offset on y-axis is arbitrary. Large pitch of ~ 14 nm measured over three periods denoted by filled arrows. Small pitch of ~ 3 nm measured over two periods (open arrows), consistent when measured at other locations (0.5 V, 110 pA).	81

5.4	Voltage-dependent imaging of the pilus nanowire shown in Fig. 5.3. The apparent height is proportional to the integral of density of states (Chapter 2.1.2). (a) Topographs of the same pilus section obtained at different sample voltages. (b) Three-dimensional rendering of the topographs at +1.0 V and -1.0 V to highlight differences in apparent height on the left edge versus the right edge. (c). Representative line profiles taken at the same location for +1.0 V (dark blue) and -1.0 V (light blue).	84
5.5	Voltage dependent imaging in 100 mV increments for the pilus from Fig. 5.2. (a) The white box denotes the location at which all images in (b) were cropped ($V=900$ mV; $I=70$ pA). (b) Topography development with voltage changing in 100 mV increments between +1.0 V and -1.0 V. Images near +1.0 V have a larger apparent height on the right edge while images near -1.0 V have a larger apparent height on the left edge, qualitatively consistent with the observation for purified pili in Fig. 5.4. Here, a large pitch of 6–8 nm is constant with voltage and a small pitch of 2–2.5 nm shifts from right to left with voltage. ($ I =70$ pA)	86
5.6	Position dependent tunneling spectra for a purified pilus. Red: I - V spectroscopy curves at left edge, center, and right edge locations denoted in the topograph. Each is an average of 100 I - V curves obtained in sequence. Blue: dI/dV spectroscopy curves at the left edge, center, and right edge locations denoted in the topograph. Each is an average of 20 curves obtained with a lock-in amplifier, followed by 19-point Savitzky-Golay smoothing. The blue and yellow circles are added to the dI/dV curves at ± 1.0 V and ± 0.3 V, respectively, as visual aids for observing the asymmetries at those voltages. (Topograph: $V=1.0$ V; $I=150$ pA)	88
5.7	(a) dI/dV tunneling spectroscopy for fourteen curves spanning the diameter of the same pilus under the same conditions as in Fig. 5.6; locations marked in (b). Right edge to left edge is top to bottom. A short red line denotes an omitted curve due to anomalous noise, inconsistent among the 20 averaged curves. Major tick marks in (a) are each $0.21 \text{ G}\Omega^{-1}$. (c) Asymmetry factors for each of the fourteen dI/dV curves in (a). (Topograph: $V=1.0$ V; $I=150$ pA)	89

5.8	Purified PAK pilus control sample. (a) AFM characterization of purified PAK pili. (b) STM topograph of purified PAK pili, indicative of unstable tunneling current and insulating behavior ($V=3.0$ V; $I=50$ pA). (c) I - V tunneling spectrum taken at the point denoted in (b). Voltages had to be high to obtain appreciable signal. The curve has a flat (insulating) region that extends well outside the bounds where significant tunneling current was obtained for <i>G. sulfurreducens</i> pili (Fig. 5.6), and well outside the bounds of biologically relevant electron transfer energies.	92
6.1	Schematic of the experiment. Purified pili suspended in water are deposited onto a surface electrode. For electronic measurement, the pilus bridges the electrode to a conductive AFM tip. <i>Upper right</i> : Photograph of one of the electrode geometries we use.	100
6.2	Representative STM I - V spectroscopy taken at a point above a clean silicon wafer like that used in the electrode of Fig. 6.3, plotted on a log scale. Arrows mark the edges of the band gap, well outside the region probed in Fig. 6.3.	102
6.3	I - V curves obtained with CP-AFM at points from the AFM topograph at right. The nanowire and substrate curves were taken with the tip placed roughly 200 nm away from the electrode. We have not speculated here on the origin of the finite current at zero voltage. While the electrode curve appears vertical and overlaps the current-axis, it has finite slope consistent with gold conductivity.	103
6.4	AFM characterization of a deposition onto 300 nm SiO ₂ . The larger, 7 μ m x 7 μ m topograph shows widespread coverage of pili, and the inset shows pili lying across the electrode edge. The inset is an amplitude signal topograph taken following the larger image.	104
A.1	Examples of geometric distortions due to finite tip geometry. (a) Filament (black) of diameter D is broadened when scanning with a tip of finite radius R_{eff} . (b) Broadening of a step edge due to finite tip radius. L is the apparent length over which the step edge rises. This may be used to quantify the effective tip radius. (c) Geometric distortion for large filament where tip is approximated as a cone. The apparent radius is broadened due to imaging before apex reaches the filament. (d) Schematic of tunneling junctions for tip-surface and tip-molecule-surface configurations. The interface between the molecule and the surface acts as a second tunneling junction.	119
B.1	Representative AFM line profile of several pili. The white line marks the location of the cut.	121

- C.1 The average (undistorted) crystal structure of CeTe_3 consisting of CeTe slabs corrugated as shown, separated by a double layer of a 3.1 \AA square Te net. The side view shows two complete unit cells repeated along the \vec{b} axis (vertical, perpendicular to the cleavage plane). The top view shows the exposed surface upon cleaving, displaying the square Te net and positions of the subsurface Te and Ce atoms. The subsurface Ce atoms are 2.53 \AA below the Te net, while the Te atoms are 3.44 \AA below. 124
- C.2 Room temperature STM topography. Raw topography (a) and reverse FT (b) clearly showing both the square surface Te net and the CDW oriented 45° relative to the net. (b) was obtained by filtering noise below a certain threshold magnitude in the Fourier transform. This image also shows the location of the \vec{a} and \vec{c} lattice vectors. (c) FT image obtained by adding the square root sum of six topographs taken consecutively. The color scale is the relative Fourier magnitude, where blue to white corresponds to low to high magnitude. Two of the peaks corresponding to the surface Te net are labeled L , and the other two were lost when filtering out noise lying along the vertical axis that was an artifact of the scan direction. One of the peaks corresponding to the CDW wave vector is marked, along with two of the four peaks corresponding to the larger square lattice rotated 45° relative to the surface Te net. (sample voltage=800 mV; $I=50 \text{ pA}$) 127
- C.3 Low temperature STM topography (77 K). (a) Topograph again showing the surface Te and several periods of the CDW. The image is the average of four images that were obtained consecutively. The bright irregular features indicate surface contamination. A lattice grid, where line intersections indicate surface Te locations, is superimposed on the $2 \text{ nm} \times 2 \text{ nm}$ inset. The grey lines on the left side of the topograph indicate CDW maxima. (b) Fourier transform of the low temperature data in (a). The color scale is the relative Fourier magnitude, where blue to black corresponds with low to high magnitude. The same peaks are labeled as in (a), but are much more clearly distinguished in the low temperature data, where STM is more thermally stable. (sample voltage=100 mV; $I=0.6 \text{ nA}$) 128

- C.4 (a) Cartoon showing the locations of dimers observed with STM for the related material TbTe_3 in Reference [5], as well as the locations of the subsurface Ce and Te atoms. Because the Fourier transform lacks phase information, the square net rotated at 45° relative to the Te net observed in our Fourier transforms of CeTe_3 (Figs. C.2 and C.3) could be due to either these dimers or to the subsurface Ce or Te net. (b) STM topography of CeTe_3 at room temperature and sample voltage -800 mV, the same used when dimerizations were observed in Ref. [5]. The current set point here was 140 pA, which was necessary to achieve quality comparable to that of [5]. We did not observe evidence of dimerizations in CeTe_3 under these conditions. Lower quality images at 50 pA also lacked evidence of dimerizations. The image is raw data, aside from line by line subtraction. (c) Low-pass ($|k| < 26 \text{ nm}^{-1}$) Fourier filtered image of the same data as in (a), given in high contrast for comparison with [5]. 130
- C.5 Simulation of STM image to investigate the relative contributions of the subsurface Ce and Te to the topography that results in the square lattice rotated 45° to the surface Te net. The image here is a contour plot of the charge density projected onto a plane at 3.0 \AA above the surface (roughly the distance to the tip), in the energy range of 0.0-0.1 eV. The subsurface Ce atoms contribute more to the charge density than the subsurface Te atoms. The Fermi level corresponds to 0.0 eV. Moreover, the subsurface modulation is of comparable magnitude to the signal from the surface Te net. 132

Chapter 1

Introduction

The potential for applications of nanotechnology today exceeds the realms of ever smaller devices and ever cleverer materials. It will likely transform how communities produce energy, how engineers build computers and devices, and how doctors treat and detect diseases. The diverse community comprising that described by the popular term nanotechnology is not limited to scientists and engineers from the physical sciences. Indeed, nano is also bio. Nanomedicine gives doctors hope that one day they may detect disease much earlier than they are able to today with the aid of molecular sensors, and when required, treat diseases much more efficiently with molecular machines that target drug delivery. Nano-scale biomolecules are not limited to the field of medicine. Researchers in the field of microbiology continue to discover new and understand old molecular machines grown inside of living microbes. For instance, a set of anaerobic microbes naturally produce molecules that manipulate electron flow in such a way to neutralize toxic materials. Thus, the modern study of these mechanisms has brought bioremediation under the roof of nanotechnology. Moreover, these electrically active molecules may be engineered for other applications, such as current production in fuel

cells or information conduits in biosensors and biocompatible devices.

One family of microbes in particular, bacteria from the family *Geobacteraceae* produce extracellular appendages called pili that effectively act as nanowires, transferring electrons outside the cell and to external electron acceptors. This has been explicitly confirmed in one extensively studied species from this family, *Geobacter sulfurreducens*. Figure 1.1 shows a transmission electron micrograph of the cell and pili of *G. sulfurreducens*, a frequently studied species because it is genetically tractable. Key to a fundamental understanding of how these biological processes work is an understanding of the fundamental process of electron transfer in the microbial nanowires. The postulated transport across distances on the order of microns would require a novel mechanism of biological electron transfer. Naturally, scanned nano probes, so frequently used in the physical sciences, are suitable for studying nano scale properties such as molecular and electronic structure. The scanning tunneling microscope (STM) and the conductive probe atomic force microscope (CP-AFM) are particularly sensitive to electronic properties and may probe states at the nano scale, in addition to facilitating high resolution imaging of these tiny molecules.

Instead of internally respiring oxygen and carbon dioxide, *Geobacter* species couple the oxidation of hydrocarbons with the reduction of external oxides. The most common oxide reduced in the organism's native environment is Fe(III) oxide. Acetate is an effective electron donor in the process, and its oxidation is coupled to Fe(III) reduction via



The discovery of these species altered the notion that metal reduction in sedimentary environments happened exclusively without microbes. In fact, reduction by *Geobacter* species is

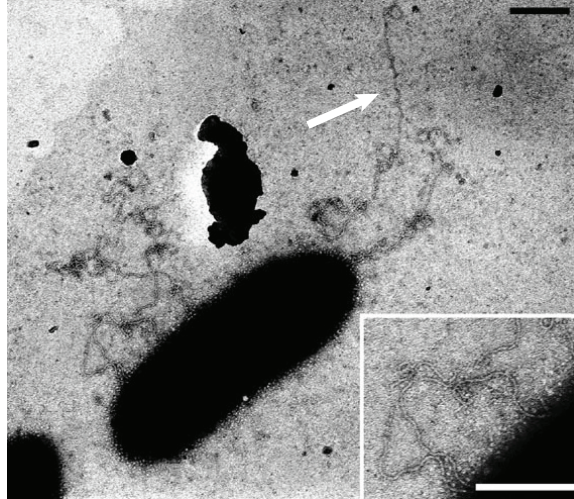


Figure 1.1: Transmission electron micrograph of *Geobacter sulfurreducens* cell expressing visible pilus nanowires. The lead author on the study that produced this image was our collaborator, Gemma Reguera. Scale bars are 200 nm. (Adapted by permission from Macmillan Publishers Ltd: NATURE (nature.com/nature) [1], copyright 2005).

sometimes more efficient than abiological means [6].

In addition to acetate and Fe(III), *Geobacter* species may metabolize other substances, including some that are toxic to humans and other organisms. One notable example is that soluble uranium (VI) oxide may replace Fe(III) as the terminal electron acceptor. This reaction reduces soluble U(VI) to insoluble U(IV) [6]. While U(IV) is still chemically toxic to living things, its insolubility prevents it from entering the water table and traveling from the contamination site. Moreover, its insolubility makes it much more difficult for the human body to absorb even if it is present. In addition to remediation of toxic substances by reduction, *Geobacter* species also have the ability to oxidize toxic aromatic hydrocarbons, like those found in crude oil pollution [7, 8].

In order to actively enhance bioremediation in sites contaminated with either of these types of pollutants, additives to the aquifers can stimulate these metabolic processes. Researchers demonstrated that injection of acetate into uranium-contaminated aquifers resulted

in a reduction in the ratio of U(VI) to U(IV) that was coupled to an increase in populations of *Geobacter* species [9]. For accelerated oxidation of aromatic hydrocarbons like benzene and toluene, reduction of Fe(III) may be stimulated with the addition of chelators that make it more accessible [10] or graphite electrodes that increase the surface area for electron donation [11]. It has been shown that the pilus nanowires in *Geobacter sulfurreducens* allow more efficient reduction of U(VI) and Fe(III) [1, 12], indicating that they are likewise important in bioremediative processes. Optimization of these nanowires through genetic modification or selective pressure could further improve *Geobacter*'s capacity for bioremediation.

Another application resulting from the conductive nature of the *Geobacter* pili emerges when cells form biofilms on fuel cell electrodes. The fuel cells produce current when *Geobacter* oxidizes electron donors in the organic fuel and transfers the electrons to electrodes, which act as the terminal electron acceptors. Experiments growing *Geobacter sulfurreducens* biofilms on electrodes demonstrated that the pili were necessary for biofilm formation [13] and maximum current measured from the electrodes [14]. The average thickness of these biofilms was 40 μm with the *Geobacter* cells farthest away from the electrode still being metabolically active. Because they need to donate electrons to an acceptor to survive, this means that they had electrical access to the electrode despite being 40 μm away, likely from a series of interconnected nanowires. Since there is no known evolutionary pressure to transfer so much current to an electrode, the authors of the report suggested that the electron transport system may not yet be optimized. Indeed, selective pressure, where the same culture was grown for weeks, resulted in a new strain identified near the electrodes that was capable of current production that was roughly a factor of five larger than wild type *G. sulfurreducens* [15]. Further optimization of the pili, resulting in an understanding of their

electron transport mechanisms may further enhance the current. While these fuel cells only produce current on the order of milliamps, they may be used as low power sources in remote locations and use organic waste matter as electron donors.

From a physical perspective, we may examine the fundamental mechanisms of *Geobacter*'s electron transport to gain understanding that may lead to better control and application. As Chapters 3 and 5 will discuss, evidence thus far suggests that electrons are transferred over micron distances along the protein matrix. This realization would require a novel conduction mechanism, as fundamental understanding of protein conductivity limits the distance of tunneling or multistep hopping to 35 Å [16]. Recent observations of 120 Å conductivity in α -helical peptides suggest multistep hopping [17], but this is still two orders of magnitude less than the postulated distance for *Geobacter* pilus electron transfer.

Scanned probes are natural local probes for these nano scale effects. The STM and CP-AFM in particular are sensitive to both morphological and electronic structures. These techniques have been successfully applied to study the electronic structure of other electrically active biological molecules, such as c-type cytochromes [18, 19, 20], the blue copper metalloprotein azurin [21, 22, 23, 24], and in sequencing DNA through differentiation of electronic signatures of different nucleosides [25].

For the research discussed in this dissertation, we primarily used these conductive probes to study the electronic properties of the pilus nanowires in *Geobacter sulfurreducens*. For this reason, Chapter 2 gives an introduction to the theory of the STM and AFM scanned probe techniques, along with practical considerations for implementation in general and in our own lab. Next, Chapter 3 gives a more detailed description of the *Geobacter* respiratory system. Additionally, I discuss important biological principles and electron transfer mech-

anisms directed toward the reader with a physical science background. We used STM to examine the local density of states of *G. sulfurreducens* pili deposited onto the surface of a conducting substrate. Because graphite, our ideal substrate for STM study of deposited pili, expresses artifacts on its surface that mimic filament-like biological molecules like pili, Chapter 4 discusses our experimental work in identifying common and new artifacts. This helped us differentiate artifacts from pili during STM experiments with pili. In Chapter 5, I discuss the result: that we were able to study the spatial dependence of the local electronic structure. The STM observations of pilus electronic structure do not alone prove long range conductivity. In Chapter 6, I will discuss an experiment using a CP-AFM tip to measure axial conductivity of a pilus nanowire to a surface electrode. I conclude, in Chapter 7, with a discussion of our current and future scanning probe studies of *G. sulfurreducens* pilus nanowires.

Chapter 2

Scanning Probe Microscopy

In 1981, Binnig and Rohrer invented the scanning tunneling microscope (STM) [26], providing the powerful capabilities of atomically resolved real space imaging and electron energy spectroscopy of conductive surfaces. Today, a variety of scanning probe microscopes (SPM) has opened up numerous imaging and physical measurement schemes with nanometer or better resolution. Soon after the arrival of STM, the atomic force microscope (AFM) [27] enabled high resolution imaging of insulating surfaces, along with the capability of performing force spectroscopy. In the years since, other varieties of SPM have granted nano scale access to numerous physical properties for imaging and spectroscopy. These include electrostatic forces [28, 29], magnetic forces [30], friction [31, 32], capacitance [33, 34] and more.

The research described in this thesis pertained primarily to the structure and electronic properties of nanometer sized molecules. The STMs in our lab facilitated high resolution imaging and electronic spectroscopy, and we utilized AFM for imaging and—when equipped with a conducting probe—electronic measurements. In this chapter, I give a theoretical

basis for these techniques, as well as practical considerations for design and operation, giving special attention to the equipment we used. The great majority of my research was based on STM experiments, and I therefore discuss it first and in the most detail, in Sections 2.1–2.3. Section 2.4 describes AFM theory and design with more brevity.

2.1 Scanning Tunneling Microscopy Theory

Two decades before the invention of the STM, Ivar Giaever observed the tunneling current flowing between two electrodes separated by a thin (\sim nm) insulating oxide barrier. In such a configuration, the oxide acts as a potential tunneling barrier for electrons in the two electrodes, and application of a voltage difference allows a net tunneling current to flow that gives information about the densities of states of the two electrodes. In Giaever’s experiment, one of the electrodes was a superconductor, and he observed the energy gap in its density of states, an important verification of the BCS microscopic theory of superconductivity [35, 36].

When one of the two electrodes is a mobile sharp probe, and the insulator is a vacuum gap, the spatial variation of the density of states of the second electrode may be probed with atomic precision. This was the invention of Binnig and Rohrer [26], called the scanning tunneling microscope. A simple representation of the STM apparatus is shown in Fig. 2.1. A voltage difference is applied across a very sharp conducting tip and a conducting surface as they are carefully brought toward each other with a spatially sensitive piezo motor. A quantum tunneling current is detected when the separation closes to just a few angstroms. Physically, the system resembles a classic bulk tunneling junction, the additional technological challenges notwithstanding. The insulating gap need not be a vacuum; the technique also works well in air and liquid. The image is a topograph resulting from the tunneling

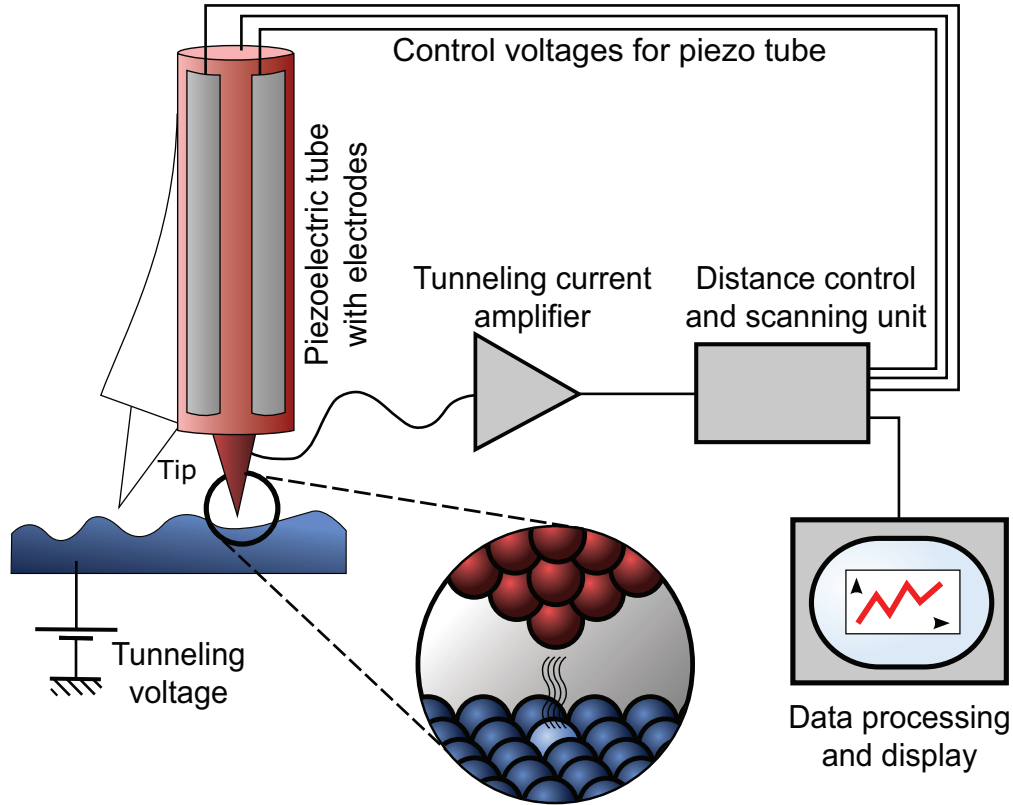


Figure 2.1: Schematic for the STM experimental setup. A voltage is applied between a sharp metallic tip and surface as they are brought to within angstroms of each other. At this distance scale, a small tunneling current flows. Scanning of the tip proceeds by applying appropriate superposition of voltages to each of the four quadrants of the piezoelectric scanning tube. (Creative Commons Attribution ShareAlike 2.0 Austria License, Authors Michael Schmid and Grzegorz Pietrzak) For interpretation of the references to color in this and all other figures, the reader is referred to the electronic version of this dissertation.

current, which is quite sensitive to variations in height from surface topography. Ideally, the tip has an atomic apex, allowing atomic spatial resolution in concert with the height sensitivity. In the three decades since its invention, STM has also enabled spectroscopy of surface electronic states distinguishable from atom to atom. It has allowed researchers to probe states of localized phenomena such as vortices in superconductors [37, 38] and to probe molecular spectra of biological [39] and other [40, 41, 42] organic molecules.

In a simple approximation, the gap between the tip and sample with an applied voltage may be modeled as an elementary one-dimensional trapezoidal barrier (Figure 2.2). To

understand the character of the tunneling current, we may begin by writing down the forms of the solutions to the one-dimensional time-independent Schrödinger equation:

$$-\frac{\hbar^2}{2m} \frac{\partial^2 \psi_n(z)}{\partial z^2} + U\psi_n(z) = E\psi_n(z) \quad (2.1)$$

where $\psi_n(z)$ is the wave function of the n^{th} electron, m is the mass of the electron, U is the average height of the barrier above the Fermi level (E_F), and E is the electron energy. The z -axis is perpendicular to the surface. Outside the barrier the solutions to the differential equations are sinusoidal in z . Inside the barrier, which is classically forbidden, the solutions to the equation are exponential in z . The solutions in these three regions are summarized here for a tunneling gap (barrier width) d , and $z = 0$ defined at the surface of the sample:

$$\psi_n(z) = \begin{cases} \psi_n(0)e^{\pm ikz}; k = \frac{\sqrt{2m(E - E_F^{\text{tip}})}}{\hbar} & z > d \\ \psi_n(0)e^{\mp \kappa z}; \kappa = \frac{\sqrt{2m(U - E)}}{\hbar} & 0 < z < d \\ \psi_n(0)e^{\pm ikz}; k = \frac{\sqrt{2m(E - E_F^{\text{sample}})}}{\hbar} & z < 0 \end{cases} \quad (2.2)$$

Given that the wave function must be continuous at $z = d$, the probability of an electron to tunnel across the barrier is then the square of the wave function within the barrier at a distance d , the width of the gap:

$$P \propto |\psi_n(0)|^2 e^{-2\kappa d} \quad (2.3)$$

In the preceding discussion, we made no assumptions as to whether the electron tunneled from the tip to the sample or from the sample to the tip. In reality, it is only when one

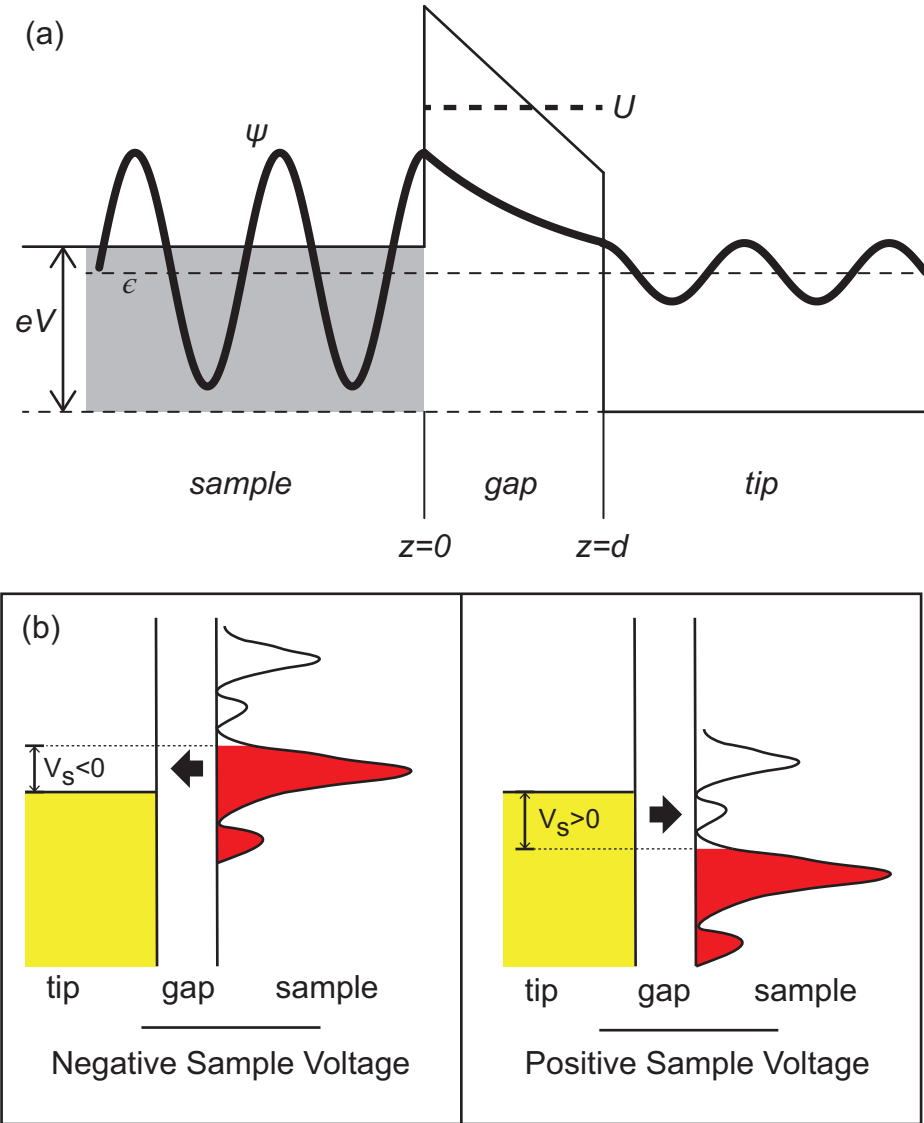


Figure 2.2: One-dimensional approximation of the tunnel junction. (a) Energy diagram of the one dimensional tip-vacuum-sample configuration with an applied voltage, corresponding to the energy difference eV . Dashed lines denote the locations of the electron energy, $\epsilon = E - E_F$, and the average barrier height, U . An electron wave function ψ is superimposed. (b) Cartoon of the states probed in STM. Depending on the polarity of the applied voltage, either unoccupied or occupied states of the sample are probed.

applies a bias voltage between the tip and the sample that the probability increases for one direction over the other, and the system achieves a net tunneling current. On average, when a negative voltage is applied to the sample, electrons tunnel from occupied states of the sample into the tip, while at positive sample voltage, electrons tunnel from the tip into unoccupied states of the sample (see Fig. 2.2(b)). Thus, the STM may probe both occupied and unoccupied states of the sample (as well as those of the tip, incidentally). The current is proportional to the probability of electron tunneling, which decays exponentially with tip-sample separation. All states between E_F and $E_F - eV$ may tunnel, and the current may be written as:

$$I \propto \sum_n |\psi_n(0)|^2 e^{-2\kappa d} \quad (2.4)$$

where κ was defined in Eqn. 2.2. This assumes zero temperature and that the tunneling matrix element is the same for all states (Section 2.1.1). It is clear from this expression that the magnitude of the tunneling current itself also depends exponentially on the separation between the tip and sample. In fact, it depends on distance quite significantly as we shall now see. When the electron energy is much smaller than the average work function, ϕ (i.e. pure tunneling regime), then $(U - E) \approx \phi$, and the exponential factor simplifies to $e^{-1.025\sqrt{\phi}d}$. Here, the other dimensions in the exponent have also been absorbed into the coefficient, 1.025. Typical values for work functions are ~ 5 eV, leading to typical decay constants of $\sim 1 \text{ \AA}^{-1}$. Thus, when the tip is pulled back just one angstrom ($d = 1 \text{ \AA}$), the tunneling current is reduced by an order of magnitude.

This high z -resolution also leads to very good lateral resolution because the tip atom closest to the surface receives most of the tunneling current. For many surfaces, atomic resolution is possible (see Section 2.1.2), including graphite, for which an example of resolved

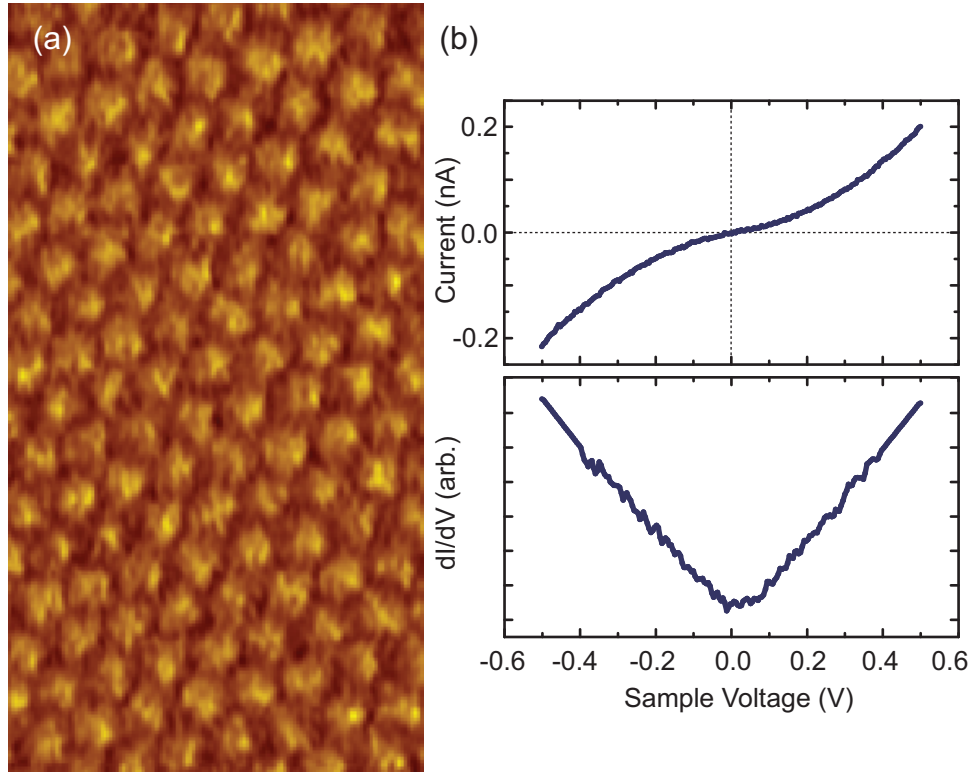


Figure 2.3: (a) Atomically resolved carbon atoms from the surface of graphite. The image had minimal processing. The color scale of each line was set to the same average value, but there was no smoothing of adjacent pixels. (b) I - V and dI/dV curves obtained on the surface near the area imaged in (a). The dI/dV curve is characteristic of the surface density of states for HOPG. ($I=250$ pA; $V=50$ mV)

surface atoms is shown in Figure 2.3(a). In addition to atoms, the STM may easily resolve larger surface structures, including step edges, pits, and trenches. Nanometer resolution is possible on virtually every conducting surface, which makes the STM an attractive tool for imaging and probing electronic states of nanometer scale phenomena and nanometer sized molecular adsorbates. In addition to sensitive imaging, Equation 2.4 also suggests that we may study a spectrum of electronic surface states, many of which come from bulk properties. The general theory of STM spectroscopy will be discussed in Section 2.1.3.

2.1.1 Tunneling Current: Perturbation Theory

The expressions in the previous section gave the critical result that the magnitude of the tunneling current in STM is exponentially dependent upon the distance between the tip and sample. However, we ignored the time dependence of the solution. A more complete solution incorporates the tunneling rate, but the Schrödinger equation is much more difficult to solve analytically in its time-dependent form. Using time-dependent perturbation theory, though, we may derive an expression for the tunneling current incorporating the time dependence.

Following the formulation of Bardeen [43] for the tunneling current in a metal-insulator-metal junction (MIM), we consider the surface wave functions of the two planar electrodes as separate systems, calculated from the stationary Schrödinger equations. When the electrodes are brought into close proximity, the rate of transfer may be calculated using time-dependent perturbation theory. The transition probability per unit time is given by Fermi's golden rule,

$$t = \frac{2\pi}{\hbar} \left| \langle \psi_\mu | H' | \chi_\nu \rangle \right|^2 \delta(E_\nu - E_\mu) = \frac{2\pi}{\hbar} |M_{\mu\nu}|^2 \delta(E_\nu - E_\mu) \quad (2.5)$$

where ψ_μ and χ_ν are the states of the two electrodes (the surface and the tip in the case of STM). H' is the first order perturbed Hamiltonian, and M is the tunneling matrix element. The delta function in the equation dictates that electrons may only tunnel into states of equal energy. Bardeen's integral gives the expression for the tunneling matrix element in this configuration:

$$M_{\mu\nu} = -\frac{\hbar}{2m} \int_{\Sigma} (\chi_\nu^* \nabla \psi_\mu - \psi_\mu \nabla \chi_\nu^*) d\vec{\mathbf{S}} \quad (2.6)$$

where the integration is taken over an arbitrary surface Σ between the two electrodes. The tunneling current may be expressed by summing over all electron energies, and in standard

STM situations, the energy states may be considered a continuum between the Fermi level and eV . The net tunneling current is then:

$$I = \frac{4\pi e}{\hbar} \int_{-\infty}^{\infty} [f(\epsilon - eV) - f(\epsilon)] \rho_S(\epsilon - eV) \rho_t(\epsilon) |M|^2 d\epsilon \quad (2.7)$$

where $f(\epsilon)$ is the Fermi-Dirac distribution for fermions, $f(\epsilon) = [1 + \exp(\epsilon/k_B T)]^{-1}$. Here, ρ_S and ρ_t are the densities of states of the sample and tip, respectively, and ϵ is the energy of the electron, relative to the Fermi level ($\epsilon = E - E_F$). For very low temperature, the Fermi distribution becomes a step function, and Equation 2.7 simplifies to

$$I = \frac{4\pi e}{\hbar} \int_0^{eV} \rho_S(\epsilon - eV) \rho_t(\epsilon) |M|^2 d\epsilon \quad (2.8)$$

Of course, STM experiments take place at finite temperatures, some of which are room temperature or higher. The effect of thermal broadening in the spectral resolution will be discussed in Section 2.1.3. Equation 2.8 is a good approximation at very low finite temperatures, as well as other situations where spectral features are larger than the thermal smearing.

Equation 2.7 was derived for a tip and surface separated by a vacuum tunneling gap. In the case where a molecule is situated between the two electrodes (see Fig. A.1(d) in Appendix A), it has been shown, for carbon nanotubes [44], that the effect of the substrate and tip on the electronic states of the adsorbate is negligible. Shifts in energy of intrinsic features were on the order of 0.01%-1%, corresponding to typical shifts on the order of 1 mV. For these magnitudes, the system may still be considered to be in the weak coupling limit, and Equation 2.7 should still be valid.

2.1.2 Imaging

While STM topography depends upon tunneling current and thus is sensitive to the charge density on the surface, the image typically follows the surface structure very closely. This is because the magnitude of the tunneling current is exponentially dependent on the tip-sample separation (Eqn. 2.4). This incredible resolution in the direction perpendicular to the surface also results in very good resolution laterally. In addition, the sensitivity of the tunneling current to the applied voltage and density of states allows for voltage-dependent imaging that gives information about the electronic structure of the sample. Both of these issues will be addressed below.

Spatial Resolution

By approximating the tip wave functions as spherical (the so-called s-wave tip approximation), Tersoff and Hamann [45] deduced the lateral resolution on a flat surface to be $\sqrt{2k^{-1}(R+d)}$, where R is the radius of curvature of the tip, d is the tip-sample separation, and k is the wave number of the tunneling electron. In practice, idealized spherical tips may have radii of curvature as large as 1,000 Å, leading to a resolution of 50 Å for typical $2k^{-1}$ value of ~ 1.6 Å. Real tips, however, often have protruding atoms that become the effective tip when imaging flat surfaces. The radius of curvature in this case is typically $(R+d) \sim 5$ Å, leading to a resolution of ~ 3 Å. This is sufficient to image atoms in a solid, which are usually spaced 2–3 Å apart.

Voltage-dependent Imaging

In practice, the STM is most often operated in constant current mode. The applied voltage difference between the tip and sample is fixed, and a feedback loop applies a voltage to the scanning piezo (see Sec. 2.3) that adjusts the tip-sample separation to keep the tunneling current constant. The control electronics produce a topographic map of the feedback voltage applied to the scanning piezo element to adjust the separation at each pixel. The result is a real space image of the surface, constructed from the surface structure and its electronic states.

The challenge in determining the tunneling current described by Equation 2.7 is in calculating the matrix elements, M (Eqn. 2.6). The calculation becomes much more manageable when the tip is modeled as a point source of current, an approximation that is valid as long as the tip wave functions may be approximated as spherically symmetric (the s-wave tip model) [45]. As the radius R becomes very large, nonzero values of angular momentum quantum number ℓ (non s-wave functions) become more influential. In the s-wave tip approximation, and for low temperature and voltage, Equation 2.7 simplifies to:

$$I \propto \int_0^{eV} \rho_S(\epsilon) d\epsilon \quad (2.9)$$

Thus, the STM in constant current mode follows a contour of constant density of states (integrated between 0 and eV) of the sample at the position of the tip. The zero here is the Fermi level. Therefore, the STM image is determined not only by the surface profile, but also by the density of states, the tip radius, and as we shall see, the associated geometric convolutions (Section 2.2.2) [46].

For voltages above 1 V, thermal excitations of electrons over the barrier and the voltage dependence of the transmission probability are no longer negligible at room temperature. In this regime, the transmission probability may be approximated using the WKB approximation (see, for example [47]). Here I will restrict the discussion to voltages $\lesssim 1$ V, the regime in which our experiments were performed.

Because the STM image depends on the integrated sample density of states (DOS), it may change if states probed by different voltages have different spatial dependence and relative magnitude. Voltage dependent images have been obtained on many surfaces [48, 49, 50]. The GaAs(110) surface is a simple demonstrative example of how the spatial variation of different energy states may be resolved by imaging at different voltages. Valence band states lie near the As atoms, while conduction band states lie near the Ga atoms. Thus, in the work of Ref. [48], when a negative voltage was applied to the sample, the STM imaged the As atoms, and when a positive voltage was applied, it imaged the Ga atoms. A superposition of two images at opposite polarities results in an image closely resembling a model of lattice at the surface [48]. Likewise, Hamers *et al.* observed voltage dependent images of Si(111)-(7x7) and Si(001) surfaces [49]. By subtracting images obtained simultaneously at voltages slightly above and below the onset voltage for a given electronic state, the visibility of the spatial dependence of that state is greatly enhanced. Multiple images at both positive and negative polarities on the Si(111)-(7x7) surface show varying electronic structure with applied voltage (Fig. 2.4).

Imaging Summary

The STM is capable of high spatial, often atomic, resolution imaging. Even in the real space topographic imaging, information on electronic structure is evident in the way the

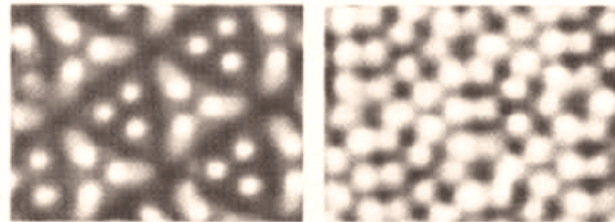


Figure 2.4: Example from the literature of voltage-dependent real space STM imaging of the surface of Si(111)-(7x7) [2]. The left and right images were taken at opposite polarities.

topographic structure changes with varying applied voltage. Different applied voltages probe different electronic states, and since the image is a convolution of the surface profile and the sample density of states (Equation 2.9), voltage dependent imaging gives spectroscopic information.

2.1.3 Spectroscopy

It is clear from expressions for the tunneling current that the STM has access to a wide spectrum of electron energy states. The current is proportional to an integral of the sample density of states over the energy range corresponding to the applied voltage (Eqn. 2.9). At zero temperature where the Fermi distribution is a step function, and at low voltages where the tunneling matrix element is a constant, differentiation of Equation 2.8 gives

$$\frac{dI}{dV} \propto \rho_s(eV) \quad (2.10)$$

An important consideration in arriving at Equation 2.10 is that the tip density of states is assumed to be constant for metallic tips. In practice, local tip states may convolve with the sample states, so it is prudent to test the tip on a calibration sample. In samples with deposited molecules on a well understood substrate such as graphite, this is especially useful

because spectra of the surrounding substrate may easily test the tip states.

At higher voltages, the voltage dependence of the transmission probability becomes more significant, but it is typically a smoothly increasing monotonic function. Thus, it contributes only a background (voltage-dependent) offset in the experimental density of states, the magnitude of which may be reduced by choice of normalization (see page 21). This effect becomes more significant above 1 V. Thus in practice, although Equation 2.10 is a good approximation, the constant of proportionality is somewhat voltage-dependent. A good visualization of this may be found in Reference [47].

Experimentally, in a straightforward representation called point spectroscopy, the tip is stopped at the point of interest, and the current (I) is recorded as the voltage difference (V) is swept within the desired range, corresponding to a range of energy states. These data may be represented in a plot of I vs. V . The derivative, dI/dV , may be obtained by either numerically differentiating the tunneling I - V curve or direct acquisition with the use of a lock-in amplifier. For direct acquisition, a small sinusoidal voltage is added to the tip-sample voltage. The tunneling current, which consequently has a sinusoidal modulation as well, is converted to a voltage and connected to an input of the lock-in, where it is compared with the source of the sinusoidal signal. The in-phase component of the current signal is approximately dI/dV . The amplitude of the sinusoidal signal added to the tip-sample voltage limits the energy resolution of dI/dV . Lock-in data presented in this thesis were obtained at room temperature. We kept the amplitude of the sine wave at 24 mV, which is roughly $k_B T$ at room temperature and less than the spectral energy resolution (~ 100 meV, see page 22). An example of an experimentally obtained spectrum for graphite appears in Figure 2.3(b).

With the output of the lock-in amplifier we may also construct a topographic map of the

magnitude of dI/dV at a fixed voltage, such as a peak in the spectrum. This method, called scanning tunneling spectroscopy (STS), maps the magnitude of dI/dV pixel by pixel. STS may be extended beyond the mapping of spectral features at a single voltage by extracting information from maps taken at different voltages simultaneously. An example of this is the practice of mapping the high temperature superconducting energy gap [51, 52].

Normalization

We know that the differential conductance (dI/dV) across the tunneling barrier depends on the sample density of states (Eqn. 2.10). In addition, the tunneling current and thus its derivative, depend exponentially on the distance between the tip and sample (Eqn. 2.4). Because this z -dependence is a separate factor from the sample density of states, differences in tip distance affect the experimentally acquired magnitude of dI/dV . Simply stated, the magnitude of dI/dV is arbitrary because of this dependence on gap width. Comparison of *relative* magnitudes, rather, is what is useful.

Thus, to directly compare spectroscopy taken at different tip distances, the data must be normalized. Common normalizations for low voltages invoke simple scaling factors for the dI/dV or current curves. For higher voltages, the choice of normalization is often $(dI/dV)/(I/V)$, which also reduces the background from the voltage-dependence of the transmission probability and thermal excitation of electrons over the barrier [53]. Thus, a side by side comparison of I - V and dI/dV curves is inappropriate without a normalization that considers the distance between the tip and sample at the time of acquisition.

Energy resolution at finite temperature

At finite temperature, interpretation of spectroscopy must consider the thermal width of the Fermi-Dirac distribution. Now, differentiation of Equation 2.7 gives, assuming again that the density of states of the tip is independent of energy:

$$\frac{dI}{dV} \propto \rho_t \int |M|^2 \rho_s(\epsilon) \frac{\partial f(\epsilon - eV)}{\partial \epsilon} d\epsilon \quad (2.11)$$

This integral is a convolution of the sample density of states and the derivative of the Fermi-Dirac distribution, which smears the energy resolution in STM spectroscopy by $3.5k_B T$, the full width at half maximum of the derivative of the Fermi distribution. At room temperature, this results in a spectral energy resolution of about 100 meV. For operation at liquid nitrogen and liquid helium-4 temperatures, the resolution is about 25 meV and 1 meV, respectively.

2.2 Practical considerations for STM

2.2.1 Tip material and fabrication

The choice of tip material is important for physical and practical reasons. We need a material with a constant density of states so that tunneling spectra are easy to interpret with regard to the sample density of states. In addition, the tip material must be fairly strong and inert, minimizing damage from and chemical interactions with the sample and surrounding environment. Two common materials used for STM experiments are the metals tungsten and platinum. Tungsten is desirable because it is relatively strong and resistant to damage, but its utilization is generally limited to UHV environments. This is because in ambient atmospheric

conditions it develops a thin oxide layer that complicates interpretation of spectra. A more inert metal that is more desirable in ambient atmosphere and modest vacuums is platinum. In order to fortify the rather soft platinum tips, a platinum-iridium alloy is often used, with Pt:Ir ratios equal to or near 80:20.

Tips originate from metal wire that is less than a millimeter in diameter, and fabrication proceeds by mechanically cutting with hand cutters or electrochemically etching with acids. Though tip materials are metal and have constant bulk densities of states, the electronic properties of the tunneling region are what ultimately matter. Because the actual configuration of the tip orbitals at the apex are not in general reproducible and may cause the tip to deviate from metallic behavior, one must test the tip *in situ* on a calibration sample (e.g. gold or graphite). The tip should achieve desired spatial resolution and reproduce the expected density of states of the calibration sample without noticeable convolution with tip states.

2.2.2 Imaging of large adsorbates with STM

Quite often, STM examines very flat surfaces for investigation of bulk and surface states of large crystalline solids (see for example Appendix C). As such, the introduction to the imaging mechanism in Section 2.1.2 assumed this configuration. However, when features or adsorbates protrude from the otherwise flat surface, geometric convolutions between the tip and sample affect the image. If the radius of curvature of the tip, R , is much smaller than the imaged object, then geometric convolutions of the tip shape and feature shape are negligible. For flat surfaces where atomic corrugations are studied, the imaging mechanism is often a single protruding atom or orbital, leading to an effective tip radius of ~ 3 Å. By contrast,

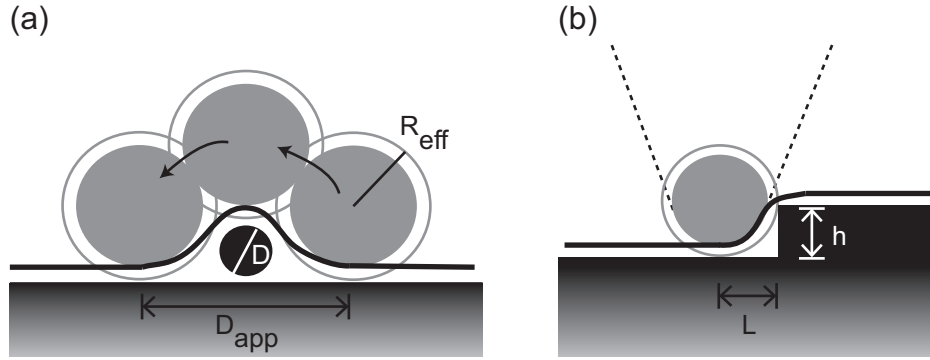


Figure 2.5: Examples of geometric distortions due to finite tip geometry. (a) Filament (black) of diameter D is broadened when scanning with a tip of finite radius R_{eff} , which includes the tunneling gap width. (b) Broadening of a step edge due to finite tip radius. L is the apparent length over which the step edge rises. This may be used to quantify the effective tip radius.

when imaging large molecular adsorbates or other surface structures, a protruding atom is not the sole imaging site. The geometry of the larger tip apex, approximated as a sphere, causes a convolution of the tip shape with the object in the resulting image. Here I discuss the effects more qualitatively, while leaving a more detailed discussion for Appendix A.

The lateral broadening of a molecular adsorbate is illustrated in Figure 2.5(a). Because of its large radius of curvature, the tip detects tunneling current much sooner than an infinitesimally small tip would. The edges of the adsorbate thus convolve with the tip radius. In practice, we would like to fabricate a tip that has as small of a radius of curvature as possible. Sharp step edges on calibration samples such as graphite serve as test features for the tip (Fig. 2.5(b)). The height of the step edge is not susceptible to geometric convolutions, so it serves as an accurate parameter. If the step edge is the height of a single atomic layer, then it may be assumed that the top of the step is atomically sharp and at a right angle to the bottom of the step. Now, the step edge is sharper than the tip, and the step edge images the tip, rather than vice versa. The radius of curvature may be calculated from this (Appendix A).

In addition to straightforward geometric considerations when imaging adsorbates, the effective tunneling gap changes from substrate to adsorbate, causing the tip to move closer or farther to maintain the constant current. Two reasons for this are the different conductivity for the adsorbate and a second tunneling gap between the adsorbate and substrate. The quantitative analysis is more involved, but careful experiments with carbon nanotubes (CNT) adsorbed on graphite have shown lateral broadening by as much as 50% for 10 nm CNT and as much as 300% for 1 nm CNT [54]. In addition, this change in effective tunneling gap may cause a change in the apparent height of the adsorbate. For this effect, CNT is again a well studied system [55, 56], with typical observations of flattening being roughly 10% [44]. A more detailed discussion of these and related tip issues is given in Appendix A.

2.2.3 Multi-tip artifacts

In the above discussion, we considered STM tips of spherical and conical symmetry, but in practice, tips are imperfect and may have multiple apexes separated laterally by a few or tens of angstroms. This leads to multiple imaging of the same atom or structure for each tip (so-called ghost images), and the problem is particularly problematic when imaging molecular adsorbates rising nanometers above the flat surface. Figure 2.6 shows a cartoon representation of the phenomenon. Such height differences in adsorbates allow access to multiple tips that may be located nanometers vertically up the tip cone where they would not be accessible by flat surfaces. When the multiple tips are located close enough laterally, the multiple images of the same object can overlap, appearing more as a single image distortion rather than separate images. Also, if the multiple tips have different geometries or electronic properties, ghost images can appear to be slightly different.

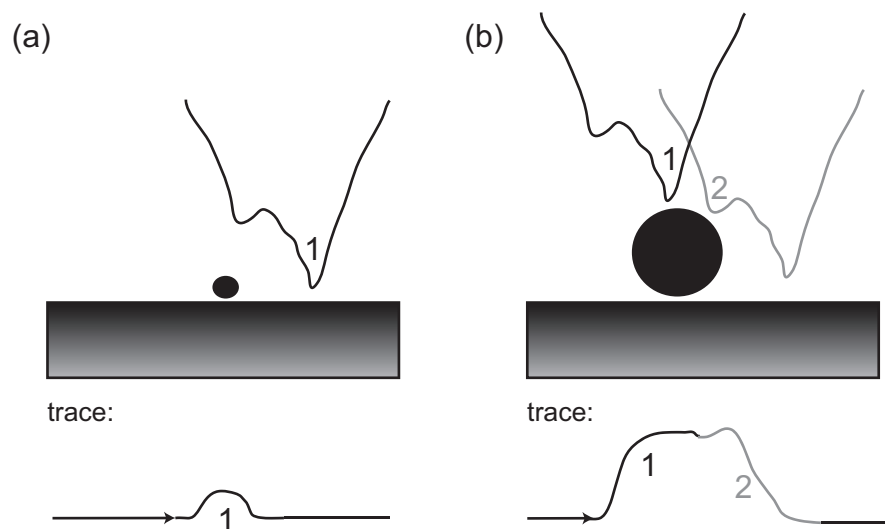


Figure 2.6: Cartoon of a multitip imaging artifact, in this case a double tip. For imaging of a flat surface and adsorbates with short height, only one tip images, resulting in the predicted topograph. (b) For a larger adsorbate protruding high enough for the second tip to image, the topograph shows the adsorbate imaged twice.

Tip fabrication methods that promote smooth and narrow tip cones reduce the probability of this effect. Usually the problem is less prevalent for electrochemically etched tips than mechanically cut tips, particularly if the etched tip has a subsequent smoothing stage of ion beam milling. For the majority of tips that we used to scan microbial nanowire adsorbates, we used electrochemically etched Pt:Ir tips and found the occurrence of multi-tips to be reduced versus mechanically cut tips. In addition, this reduces the broadening effect discussed in Section 2.2.2.

2.2.4 Vibration isolation

During STM operation, the position of the tip relative to the sample should remain stable. Vibrations of the tip and sample compromise the high resolution of the technique, as relative tip motion due to vibration is misinterpreted by the controller as physical topography. Because of the current's exponential dependence on distance, even very small amplitude vi-

brations are problematic. To maintain good surface topography, the amplitude of vibrations that reach the tip and sample should be an order of magnitude less than the required amplitude of height differences on the sample. In atomic resolution, for example, the corrugation amplitude is ~ 10 pm, requiring vibration amplitudes on the order of 1 pm [57].

The primary sources of vibrations in STM experiments are those transferred to the microscope from the building, which vibrates from human activity, such as walking and shutting doors, as well as from machinery operating at frequencies near line AC voltage. These types of vibrations are typically 5–100 Hz, and express higher amplitudes on higher floors of the building, where the bending of the walls of the building amplifies the vibration. Additional vibration sources from human activity include acoustic vibrations. Human speech in normal conversation is ~ 250 Hz, the same order of magnitude as building vibrations. Higher frequency acoustic vibrations from machinery or other activity may also be present in the lab.

The implementation of vibration isolation for a model STM system considers the global coupling of the tip-sample distance to external vibrations. Common isolation techniques divide this coupling into two stages. In the first stage, a rigid scan head connects the tip and sample, thereby isolating their separation from low frequency vibrations. The scanning mechanism is also attached to this rigid support and retains control over the relative tip-sample motion. The second stage isolates the rigid scan head itself from excitations of its high resonance frequencies. Consequently, this also isolates the tip and sample from their respective high frequency resonances. The best designs for this stage have supports with excitation frequencies lower than building vibrations, which are in turn much lower than the resonance frequencies of the rigid scan head. This means the support ought to be quite

massive and isolated from the building by a spring-like system with a small spring constant. Visualizations of these suspension systems may be found for our specific microscopes, in Figures 2.7 and 2.8. As a quantitative example, a scan head lowest frequency normal mode of 2,000 Hz coupled with a support frequency of 2 Hz leads to a transfer function of -120 dB, sufficient for atomic resolution [58]. Furthermore, scanning probe microscopes often reside on the bottom level of the building, where vibration amplitudes are smallest to begin with.

Each of the two primary stages here may have additional stages to improve isolation. For example, the rigid scan head sometimes integrates an Eddy dampener. For cryogenic experiments, the low resonance support may require enhancement via a double spring stage for sufficient dampening, rather than a single. Pneumatic spring stages can reduce the resonance frequency of the support to as low as 1–2 Hz. Finally, to isolate the microscope from acoustic vibrations transmitted through the air, it is often sufficient to place the experiment in a sound proof room.

2.3 STM Experimental Setup

Primary goals for any design of a scanning tunneling microscope system are good signal amplification with low vibrational and electrical noise. Atomic resolution imaging and precise tip placement require angstrom scale lateral control over the relative tip and sample motion. The exponential dependence of the current magnitude requires dynamic control over the tip-sample spacing that is an order of magnitude better, and implementation of a vibration isolation system minimizes external perturbation of this distance (Section 2.2.4). The careful and precise approach and scan mechanisms invoke piezoelectric elements, materials for which a voltage drop occurs when the material is compressed or stretched. Conversely,

the application of a voltage to a piezoelectric material induces compression or stretching. Voltage-controlled piezo elements are common ways of manipulating relative tip and sample motion with high precision. Design characteristics addressing vibrations, approach, and scan environment are addressed in separate sections for the two STMs used in my experiments. A third section discusses the nature of the tunneling feedback loop, which is schematically the same for the two microscopes.

2.3.1 Nanosurf Easyscan STM

Though the Nanosurf was not my primary STM, I used it for much of the investigation of graphite artifacts described in Chapter 4 and work with CeTe_3 discussed in Appendix C. A schematic of the commercial Nanosurf Easyscan is shown in Figure 2.7. The sample is affixed to a conducting cylinder that rests on very smooth rails, while the tip is held in place by a conductive clamp that doubles as the tunneling current lead. A linear piezo motor slowly approaches the sample holder toward the fixed tip via a slip-stick vibration waveform. In a slip-stick approach mechanisms, one direction of oscillation is fast enough to overcome static friction, thus slipping along the sample holder. The motor slips along the sample holder in the part of its period that moves away from the approach direction. In the other direction of oscillation, the speed is such that the motor sticks to the sample holder pushes the sample forward. The smooth rails on which the sample holder rests allow it to glide smoothly as the motor pushes it along toward or away from the tip. Electrical contact via the rails and sample holder keeps the sample at ground, and the voltage is applied to just the tip.

The compact size and rigidity of this design are advantageous for high resolution. Three piezoelectric blocks—one for each coordinate—scan the tip in the x and y (lateral) and

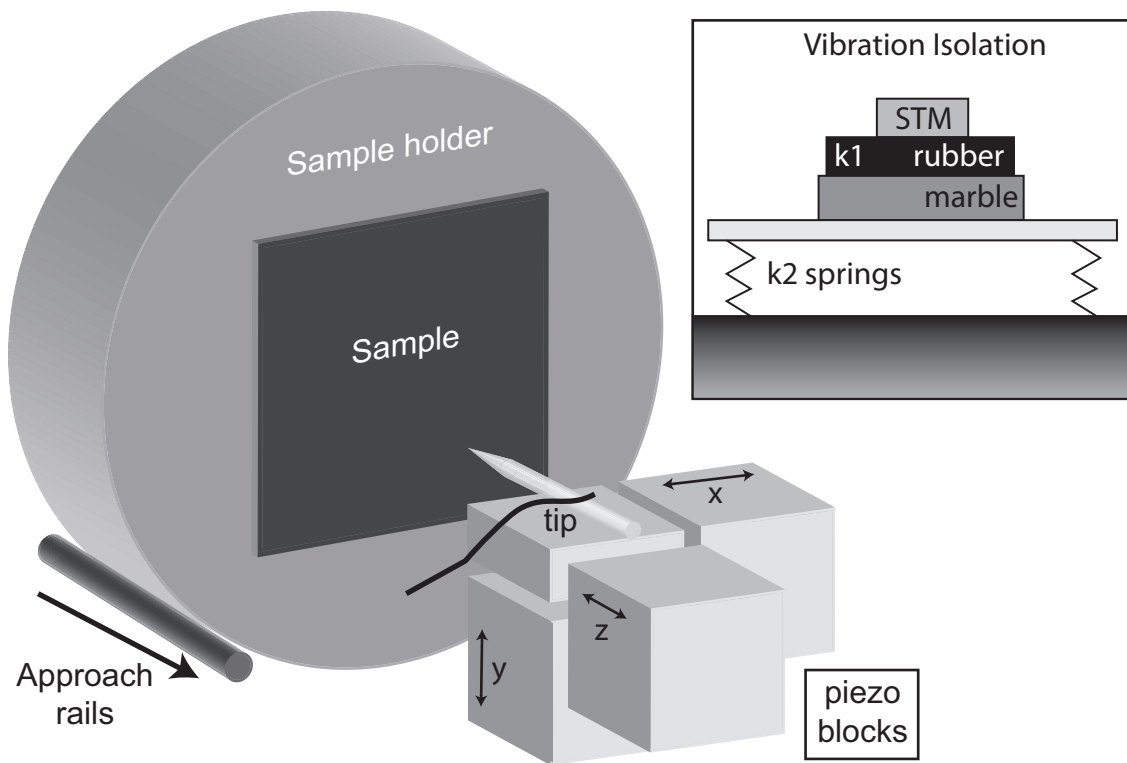


Figure 2.7: Schematic of the Nanosurf Easyscan STM design out of the box and with vibration isolation in our lab. The compact size and stability allow convenience and high resolution.

z (transverse) directions. The geometry of the piezo blocks means that their vibrational excitation modes are very high, and the spatial resolution is thus quite good. The trade-off is a scan range that is limited to just 500 nm x 500 nm. Another disadvantage is that the three independent piezo blocks in x , y , and z experience thermal fluctuations independently of each other and of the sample. The inhomogeneous expansion and contraction from this causes the microscope image to have a high propensity for thermal drift, in which the tip drifts in an uncontrollable way. Thus the image is not reproducible from one scan to the next when the rate of thermal drift is significant. Isolation from convection with the ambient environment via a small plastic cover reduces this effect somewhat.

The Nanosurf Easyscan is a so-called pocket or table-top device because of its compact size. Vibration isolation may be implemented on the table top surface (see inset, Fig. 2.7). We do so with two stages. The first stage is a rubber stack, included from the manufacturer. Typically, rubber damping stages suppress high frequencies but are unreliable for frequencies below 50 Hz [59]. The suppression of lower frequencies may be achieved with an additional, single spring suspension stage. For this, we place the microscope on a platform supported by four equivalent springs on each corner. The mass of the provided marble block reduces resonant frequencies of the entire system, and we add mobile lead weights to further dampen vertical oscillations in the system as well as oscillations in the platform itself.

In order to control the experimental environment, we place the STM in a plastic glove bag through which we flow a steady stream of dry nitrogen. This allows us to use this conveniently located and quick-loading microscope to study some materials that otherwise react to the presence of oxygen or moisture. To cleave surfaces such as CeTe_3 in a clean environment (Appendix C), we installed an optical microscope in the glove bag to assist in

cleaving *in situ*.

2.3.2 Besocke style cryogenic STM

While the table-top STM discussed above is convenient for quick sample characterizations as well as some experimental data runs, its small scan range and pervasive thermal drift limit its applicability. Moreover, cryogenic and room temperature experiments under vacuum are impossible with the table-top device. Therefore, we performed most of our STM experiments with a Besocke [60, 61] style scan head in a system with cryogenic capabilities (Fig. 2.8).

In Besocke's design, the sample is attached to a sample disk that rests upside down on three carrier piezo tubes. These tube-shaped piezos move by application of voltages through separate metal contacts to each of the four circumferential quadrants of the tube. A voltage on one side contracts that quadrant, while a voltage of opposite polarity on the opposite quadrant stretches it. The net effect is that the tube bends, and superposition of voltages among the four quadrants allow 360° of motion. A rough schematic of the way the tubes bend is shown as part of Figure 2.1. Each carrier tube supports the disk on one of three ramps machined into the disk. The approach mechanism is again a slip-stick waveform. In this configuration, the carrier piezo tubes are oscillated in a direction following a tangent to the circular sample disk. The net effect is that the disk rotates, and because of the ramps, it also moves vertically. The length of the ramp is much greater than its maximum height, so large rotational motion translates into much smaller vertical motion. Thus, the sample approaches the tip quite slowly. Electrical contact to the sample via a wire running through the center of one piezo tube applies a voltage to the sample relative to the grounded tip. In addition to approach, the carrier piezo tubes may also be used for coarse lateral positioning

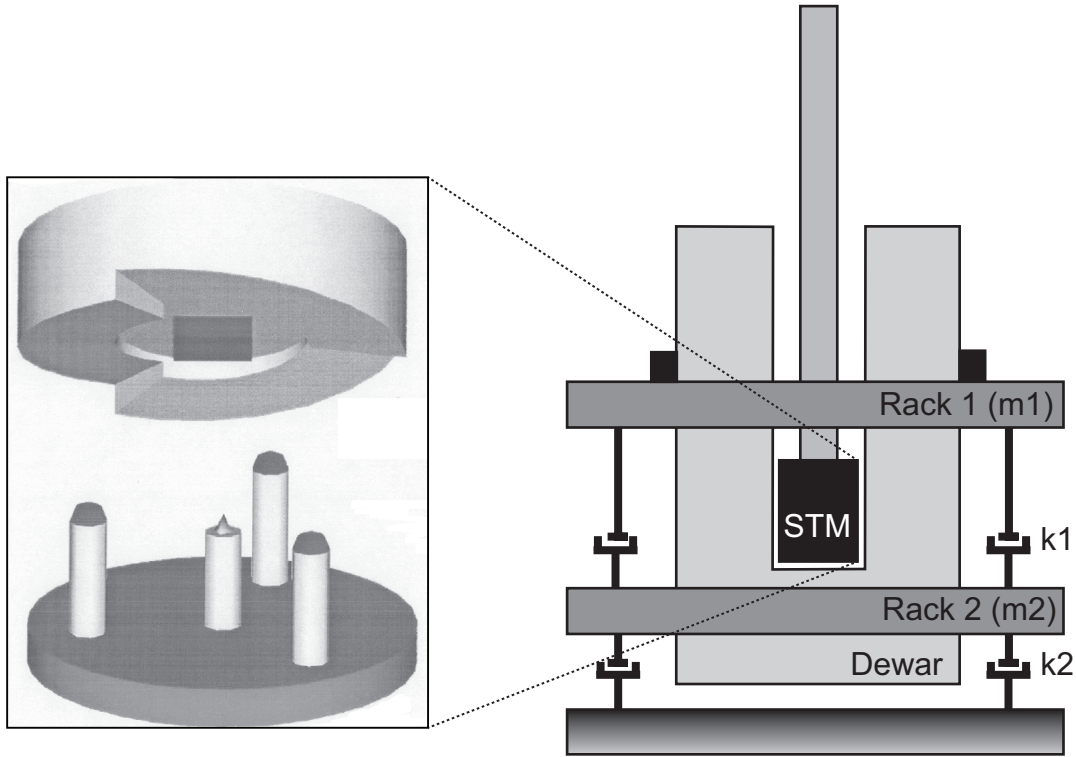


Figure 2.8: Schematic of the homemade Besocke-style STM in our lab and vibration isolation scheme. The design is mechanically and thermally stable. It possesses a larger scan range and much less thermal drift than the x - y - z block design. Our scan head may be mounted on the end of a long stick and advanced to the center of a helium-3 refrigerator under high vacuum.

of the sample relative to the tip when the sample is not in scan range.

The tip is attached to a fourth, identical piezo tube beneath the disk, pointing up towards the sample. Four-quadrant voltages scan this center piezo tube in the way voltages move the carrier piezo tubes. To adjust the tunneling gap, a uniform voltage applied to both the inner and outer radii of the scanning tube on all quadrants moves the tip perpendicularly to the sample. The sensitivity and length of the piezo tubes used in our home made Besocke scan head allow a maximum scan range of about $5 \mu\text{m} \times 5 \mu\text{m}$. Thermal drift is quite small, even when operating in ambient environment. Because the three carrier piezo tubes and the fourth scanning piezo tube are all the same size, material, and orientation, any expansion

or contraction from thermal fluctuations is roughly the same for all four tubes. Thus, drift in the tip compensates a matching drift in the sample. Operation in vacuum decreases the drift even more, as this impedes convection currents from reaching the scan head.

High Vacuum Chamber

The scan head is placed in a high vacuum chamber integrated with a cryogenic Dewar. It attaches to the end of a long stick that extends down to the center of the Dewar, which houses a helium-3 refrigerator. I will not give any data from experiments performed on pilus nanowires while the STM operated at low temperature. However, in Appendix C, I show low temperature data for the charge density wave material, CeTe_3 , and I also give a more detailed discussion of the helium-3 refrigerator there.

We can pump the sample space down to high vacuum for operation at any temperature. Under ideal conditions, we can reach 10^{-7} torr with the use of a turbo pump. Often, for room temperature experiments, the scan head remains sealed atop the Dewar for easy access, rather than pushed down to the center. This does not compromise the quality of the vibration isolation. For some experiments at room temperature, we operate under inert dry nitrogen gas. In this case, the chamber may be purged of oxygen with nitrogen and operated with a constant, low flow of nitrogen gas.

A two stage pneumatic spring mechanism isolates the Dewar from building vibrations. The Dewar rests on one rack, coupled via the first pneumatic spring stage to a separate rack loaded with lead bricks. The second rack is coupled to the second pneumatic spring stage. The addition of mobile lead bricks allows adjustments for balance and added weight. Placement of the suspension in a sound proof room reduces higher frequency acoustic vibrations, and the Dewar itself helps dampen acoustic modes when the microscope is inside.

2.3.3 Preamp and Feedback loop

The picoamp and nanoamp tunneling currents require a current amplifier to amplify and convert the small current to an appreciable voltage. Input capacitance from the coaxial cables is a significant source of noise, so the preamp should be located as close to the tip as possible. For cryogenic STM, it is not possible to place most amplifiers right next to the tip because they freeze out at low temperature. Vibrations in the cables connecting the tip to the preamp cause small changes in capacitance and thus an emf source for noise. Additionally, input noise exists at the coaxial connections themselves. For this reason, very low noise preamps or preamps with active elements that operate at cryogenic temperatures are used [62]. The preamp sensitivity of our home made Besocke STM is 10^9 V/A.

Following amplification, the feedback electronics compare the output voltage of the preamp with the tunneling current set point. After evaluating the difference between these two signals, the feedback applies an appropriate output voltage to the scanning piezo. This feedback voltage adjusts the z offset to bring the error signal down to zero. If the current is higher than the set point, the tip retracts; if it is lower than the set point, the tip advances.

Two gain modes in the feedback circuit adjust the error signal—proportional gain and integral gain, or time constant. The proportional gain amplifies the error signal to improve the response of the feedback voltage. However, transient effects in the electronics do not allow for immediate compensation. At high gain, and thus larger error signal, the rapid response may cause the feedback voltage to oscillate. To prevent this, the feedback also integrates the signal over a period of time determined by the time constant. While the response is best for independently highest proportional gain or smallest time constant, the dual necessity of quickest response to topography and stable feedback voltage requires these

to remain finite. The user controls both proportional and integral gains during operation of the experiment.

2.4 Atomic Force Microscopy

The high resolution imaging capabilities of the scanning tunneling microscope are often powerful enough to image atomic lattices, but the requirement of a conducting surface bounds its applicability. For high resolution imaging of insulating surfaces, Binnig *et al.* [27] developed the atomic force microscope (AFM). Much of the practical implementation, such as the scan head and vibration isolation, is similar to STM. Sensitive to the *forces* between a sharp tip and surface, it is also capable of force spectroscopy, in analogy to the STM's sensitivity to electronic energy spectroscopy. Forces detected include van der Waals (vdW) forces, electrostatic forces, magnetic forces, and friction. The most widely used application, however, is topographic surface imaging, which has found widespread use as a characterization tool for samples from many fields of science.

The AFM apparatus (Figure 2.9) consists of a hard sharp tip attached to the end of a cantilever. Because the tip need not be conductive, it is made of much stronger non-metallic materials, such as silicon nitride. The tip is brought toward the sample surface where it experiences the interaction forces mentioned above. For routine topographic imaging, the tip is 1–10 nm away from the surface, and the forces that dominate here are the attractive van der Waals interaction and then, as the tip comes very close to contact, the repulsive atomic force between atoms (Fig. 2.10(a)). These forces range from 10^{-9} N at 1 nm separation down to 10^{-13} N at 100 nm [57]. The minimum amount of force required to displace a typical cantilever is 10^{-18} N [27], so vdW forces provide sufficient and significant deflection of the

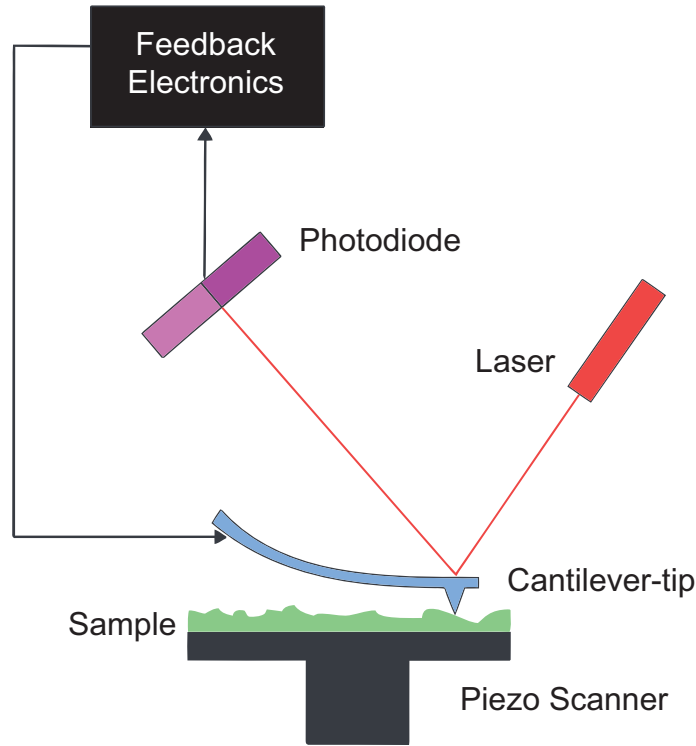


Figure 2.9: Basic schematic of an atomic force microscope having a laser-reflected detection mechanism.

tip for imaging even at large separation. Other, long range forces, such as the electrostatic or magnetic may be present, but at distances on the order of 10 nm the van der Waals force dominates. For the related electrostatic force microscopy and magnetic force microscopy, the tip is situated much farther away, in the 100 nm range where these forces dominate over short range forces.

For all experimental modes, the interaction forces between the tip and sample deflect the cantilever. While several deflection detection schemes exist, we used a quite common design. A laser beam bounces off a mirror attached to the back of the cantilever, into a four-quadrant photo detector that senses the motion of the beam. Typically, laser deflections of less than an angstrom may be detected. For routine imaging, we used a commercial AFM and controller from Dimension Instruments, in the Keck Microfabrication Facility at MSU.

For electronic transport experiments we used an AFM equipped with a conductive probe (see Section 2.4.2, Chapter 6), from Asylum, in the lab of Professor Pengpeng Zhang at MSU.

2.4.1 Modes of Imaging

Images in AFM topography may be constructed in a few different ways. The choice of imaging mode depends on the properties of the sample and the desired signal quality. Common imaging modes are discussed in the following paragraphs. First is contact mode, which, though less common now than in the early days of AFM, serves as an illustrative example of how cantilever deflection and feedback interact. Then we will discuss types of non-contact mode. First is amplitude detection, where the cantilever is driven slightly off-resonance, and changes in amplitude of the deflection determine the image. Thereafter, we will discuss tapping mode, which minimizes tip and sample interactions.

To first consider contact mode imaging, recall that the interaction mechanism in AFM is the force the tip experiences from the sample, and the detection mechanism measures cantilever deflection caused by this force. The most straightforward imaging mechanism—though not the most widely used—is analogous to constant current STM. As the tip scans the surface topography, the photo detector measures the deflection of the cantilever, and a feedback mechanism retracts or advances the tip to compensate for these deflections. Similar to constant current STM, a topograph of the constant force feedback voltage represents the surface topography. Because surface features effectively reduce the tip-sample distance, a corresponding increase in the interaction force causes the feedback mechanism to retract the tip to compensate. The opposite happens for dips in the surface topography. This mode of imaging is referred to as contact mode or dc mode. It is limited by the fact that

the signal to noise ratio (SNR) is quite low for the small surface deflections on the sample. Moreover, maximizing the SNR requires the tip to be very close to the surface, increasing the interactions and often damaging the tip and possibly the sample. For soft organic samples, the tip can tear the molecules or become contaminated.

By contrast, the AFM cantilever's vibrational characteristics provide a more sensitive metric for the interaction. In non-contact mode, or ac mode, the cantilever is modeled as a one-dimensional beam, weighted with the tip, and it is driven at or near its resonance frequency (Figure 2.10(b)). When using amplitude detection as the feedback signal, the cantilever is driven slightly off resonance. The force between the tip and the sample dampens the oscillation. Changes in the damping force, due to changes in topography, shift the resonance frequency so that the drive frequency becomes off-resonance. This causes a significant reduction in the amplitude of oscillation. Because the frequency is near resonance, the amplitude change detected by the photo detector is quite large (Fig. 2.10(b)), larger than a deflection caused by the surface topography directly in contact mode. Thus, the SNR is much greater than in contact mode. Because the cantilever was driven off resonance, the feedback can distinguish increases or decreases in height as either an increase or decrease in the amplitude, respectively (Fig. 2.10). In practice, the feedback mechanism keeps the oscillation amplitude constant, and it is important to find a sharp resonance peak before beginning the experiment, a process called tuning. An alternative implementation of non-contact mode is frequency modulation [63], where the feedback adjusts the drive frequency to keep the phase constant. For the imaging in this work, however, we used amplitude detection in tapping mode.

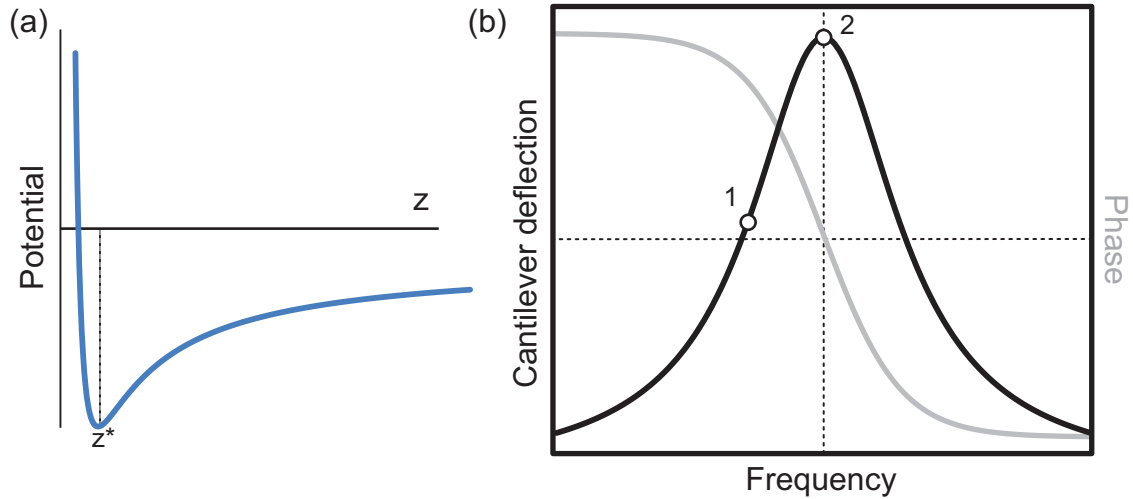


Figure 2.10: (a) Sketch of the potential versus distance between the AFM cantilever and sample surface. Depending on mode, the microscope may be operated at $z > z^*$ (non-contact mode); $z < z^*$, $U > 0$ (contact mode); $z < z^*$, $U < 0$ (tapping mode). (b) Sketch of cantilever deflection and phase as a function of frequency. Amplitude deflection mode (Point 1) is operated slightly off resonance so that the direction of deflection may be detected. Frequency modulation (Point 2) and phase modulation modes are operated on resonance.

Tapping Mode

A modification of non-contact mode called tapping mode is useful when the sample is sensitive to lateral dragging forces from scanning (such as for soft, biological molecules) or when operating the AFM in ambient conditions, where thin layers of water develop over most samples [64]. This water layer may cause the tip to stick to the surface while scanning, behaving in an unpredictable way. In tapping mode, the amplitude of the driving force is large enough that the tip only interacts with the surface near the bottom of its oscillation cycle. As the tip nears the sample, it feels the damping force, and the feedback mechanism keeps this constant as in the non-contact modes discussed previously. This technique provides high signal to noise ratio and minimizes lateral forces on the tip and sample. For routine imaging on the Dimension Instruments AFM, we have carried out experiments in ambient environment and have employed tapping mode.

2.4.2 Conductive Probe AFM

An atomic force microscope equipped with a conductive probe (CP-AFM) adds electronic measurement capability. Cantilevers are fabricated in the usual way and then coated with a metal, such as gold or platinum. A voltage is applied across the tip and sample, and the current is read through a current-voltage preamplifier. The ability to spatially resolve changes in electronic properties is limited by the resolution of the AFM itself, which is in general poorer than STM for experiments in ambient conditions and for laser-reflected AFM designs. However, the CP-AFM does have an advantage in that the forces between the tip and sample during electronic spectroscopy are quantifiable and controllable [65]. The force feedback mechanism allows the pressure applied by the tip to be held constant, which is especially useful for soft samples, such as biological samples, that are sensitive to tip forces.

STM is preferable for experiments on homogeneously conducting samples in which high resolution of the spatial variation of the sample density of states is desired (Chapter 5). If the sample has both conducting and insulating regions, or the resolution of STM is unnecessary, CP-AFM is useful for locating and identifying conducting molecules and performing electronic measurements (Chapter 6).

Chapter 3

Geobacter sulfurreducens

The metal reducing bacterium, *Geobacter sulfurreducens* has in recent years received much attention for evidence of the use of pilus nanowires to deposit electrons outside the cell during respiration [1]. Respiration is the process by which all cells produce energy. *G. sulfurreducens* is a member of the family *Geobacteraceae*, the predominant family of microbes in anaerobic environments where Fe(III) oxides are reduced to Fe(II) as they receive waste electrons [66, 67]. Specifically, the species *G. sulfurreducens* has been the subject of much experimental investigation because it is genetically tractable [68]. In other words, a complete genome is available, and protocols exist for genetic modification, such as replacement of target amino acids (Section 3.3). These substitutions are common tools by which the geneticist may experimentally alter function and structure at individual sites while keeping all others constant.

In this chapter, I give an elementary overview of the *Geobacter sulfurreducens* respiratory system, concentrating on the pilus nanowires in particular. The pilus structure is explained in Sections 3.3 and 3.4. Motivated by work in the Reguera lab, I will discuss the hypothesis

that electron transfer (ET) occurs along the protein matrix, rather than via cytochromes or other proteins with embedded metal atoms (metalloproteins). Possible mechanisms of electron transfer along the protein matrix are then discussed in the remainder of 3.4.

3.1 Elementary cell respiration

Vital to a cell's activity is the process of respiration, whereby nutrients are converted into usable energy in the form of Adenosine triphosphate (ATP), the "energy currency of life." Among the most important functions for which cells use ATP are motility and division, as well as the biosynthesis of DNA, RNA, and proteins. These functions break down the ATP into its precursors, which are then recycled.

The reactions occurring while the nutrient sources break down create a potential gradient across the membrane, which in turn drives a molecular motor to produce ATP. Correspondingly, electrons must leave the cell to conserve charge. They exit via the so-called electron transport chain, which is composed of several electrically active molecules. Many of these are metalloproteins, which are proteins with bound metal atoms (metal cofactors). The conclusion of the transport chain is a foreign terminal electron acceptor, a molecule that has a reaction potential for which the molecules in the ET chain have evolved. In aerobic respiration, the preferred mode in human cells, this terminal electron acceptor is molecular oxygen. The electron allows the O_2 molecule to bind to a carbon atom from glucose to produce CO_2 waste. Anaerobic respiration, in contrast, must proceed in the absence of oxygen, often using external metal oxides as terminal electron acceptors. The anaerobe *Geobacter sulfurreducens* breaks up an electron donor, such as acetate or hydrogen, producing the potential gradient, and then may use electron acceptors such as Fe(III), U(VI), S, or other chemical species

with appropriate reduction potentials. Typical anaerobic electron transport chains invoke cytochromes and other metalloproteins.

3.2 *G. sulfurreducens* respiration

Geobacter sulfurreducens is an anaerobic organism that completes its electron transport chain in its native environment by reducing Fe(III) to Fe(II) (Fig. 3.1). Some oxides are soluble and may be reduced in the periplasmic space (the space between the inner and outer cell membranes), but others are disperse and insoluble [69, 70]. Utilization of these insoluble oxides as terminal electron acceptors requires a mechanism for transferring electrons to the outside of the cell. This extracellular electron transfer may be facilitated by proteins embedded in the outer membrane of the cell, and indeed there is evidence that common outer membrane c-type cytochromes [71] and other metalloproteins [72], contribute to this process.

However, several experiments have made it clear that the type IV pili in *G. sulfurreducens* are also necessary for an efficient pathway to extracellular terminal acceptors and hence healthy cell metabolism [1]. Pili are filament-like appendages with diameters of 2–10 nm and lengths of microns (Section 3.4.1). The most straightforward evidence is that genetically modified mutants lacking the ability to build the pilus were grown in the presence of insoluble Fe(III) oxides and were unable to reduce them, thereby severely impeding cell growth. Another study, relevant to *G. sulfurreducens* bioremediation capabilities (Chapter 1), showed that wild type cells (the type found in nature) producing pili were able to reduce significantly more U(VI) than the mutants lacking pili [12]. Suggestive that the pili additionally transfer electrons from cell to cell is that when stressed by sub-optimal growth

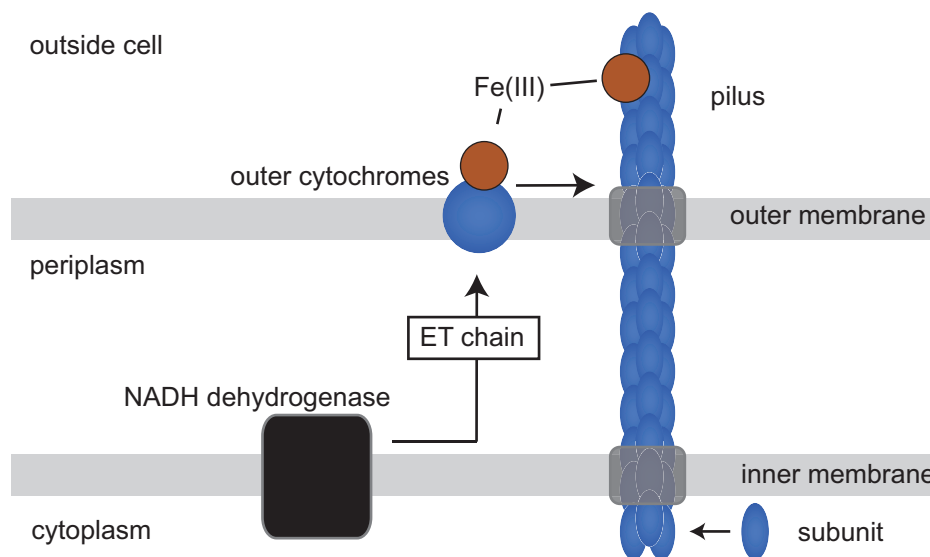


Figure 3.1: Simplified cartoon of the electron transport chain in *Geobacter sulfurreducens*. Establishment of proton gradient for ATP production results in shuttling of electrons outside the cell through a series of metalloproteins and quinones in the periplasm. The terminal electron acceptor, in this case Fe(III), accepts an electron from either an outer membrane bound cytochrome or the electronically conductive pilus.

temperatures, the cells tend to grow more pili [1]. Analysis of biofilms on fuel cell electrodes is consistent with the possibility of inter-cell transfer. As the biofilm grows, electronic efficiency of the outermost cells remains constant. For this to occur, they must be maintaining electrical access to the electrode despite the fact that they reside many layers away. Moreover, the spacing between cells suggests length scales of long pili rather than the intimate contact that metalloproteins would require [13, 14].

As demonstrated, several pieces of evidence in biological studies have suggested that the pili are an important part of the electron transport chain. As such, individually examined pili should be electrically active. Previous CP-AFM current measurements of pili verified transverse conductivity across the diameter of the pilus between the AFM tip and a conducting graphite substrate [1]. Possible mechanisms of this conductivity will be discussed in Section 3.4, and the proposal of further experiments examining the conductivity will be

discussed in Section 3.4.4.

3.3 A primer on protein structure

Proteins are molecular tools and machines that are essential for nearly all life processes. The cell synthesizes proteins such that their specific composition and folding profile define a specific function. A protein is a linearly polymerized chain of smaller molecules called amino acids. The assembled polymer, called a polypeptide, is composed of a heterogeneous sequence of amino acids from twenty distinct types that the cell produces for protein synthesis. Each amino acid has a unique side-chain, also called a residue, and the specific arrangement of these is essential to the protein's function and inter-protein interaction. The side chains are attached to the backbone, common to all amino acids, and the site at which they covalently bond to their neighbors in the peptide. (Fig. 3.2(a)). The assembly of the backbone, and the unique residue sequence, may be referred to as the primary structure of the protein.

The cell's DNA encodes for twenty distinct amino acids for use in protein synthesis. Most are composed entirely of carbon, hydrogen, nitrogen, and oxygen, while two also contain sulfur. The functional component giving each amino acid its unique properties is called the residue. These may be charged or neutral, and some are polar. Several contain aromatic residues, which are stable carbon rings with unsaturated bonds, allowing for the presence of delocalized electron states. This will be important in the discussion of electron transfer in Section 3.4.3.

A hierarchical description of protein structure is useful. The sequence of amino acids in the polypeptide is referred to as the primary structure. Secondary protein structure refers to the folding of proteins into regular geometric shapes, stabilized by hydrogen bonds across

non-neighboring residues, sometimes in a periodic manner (Fig. 3.2(b)). Common secondary protein structures are the α -helix and β -sheet. The α -helix is a right-handed coil in which residues form bonds with each other across neighboring turns of the coil. The periodicity is defined by 3.6 residues per turn, which, with the multiple hydrogen bonds, results in a very rigid structure. Another common secondary structure, the β -sheet, is a set of laterally bonded β -strands—straightened peptide series of 3–10 residues. The next order of folding, tertiary structure, describes the actual three-dimensional placement of the sub-structures (Fig. 3.2(c)). It describes, for example, the relationship of two different local α -helices to each other in space. Physically speaking, secondary and tertiary folding minimize the conformational energy of the polypeptide. Ultimately, evolutionary pressure has selected the amino acid sequence leading to higher order folding and thus a specific and optimal protein function. In quaternary structure, inter-protein interactions are invoked to assemble a structure composed of multiple protein subunits (Fig. 3.2(d)). For example, several α -helical subunits may assemble into a filamentous structure. In concert, the entire hierarchy of protein structure determines the unique functions and properties of each protein.

3.4 Possible mechanisms of electron transfer

The long-range electron transfer mediated by the pili of *Geobacter sulfurreducens* requires an understanding of electronic structure at the molecular level. In this section, I discuss common mechanisms of biological electron transfer and provide some speculation on how these may be subsets of the novel mechanism in *G. sulfurreducens* pilus electronic structure. Because protein structure—particularly the configuration of local electronic states resulting from higher order structure—is a significant determining factor in electron transfer, Section 3.4.1

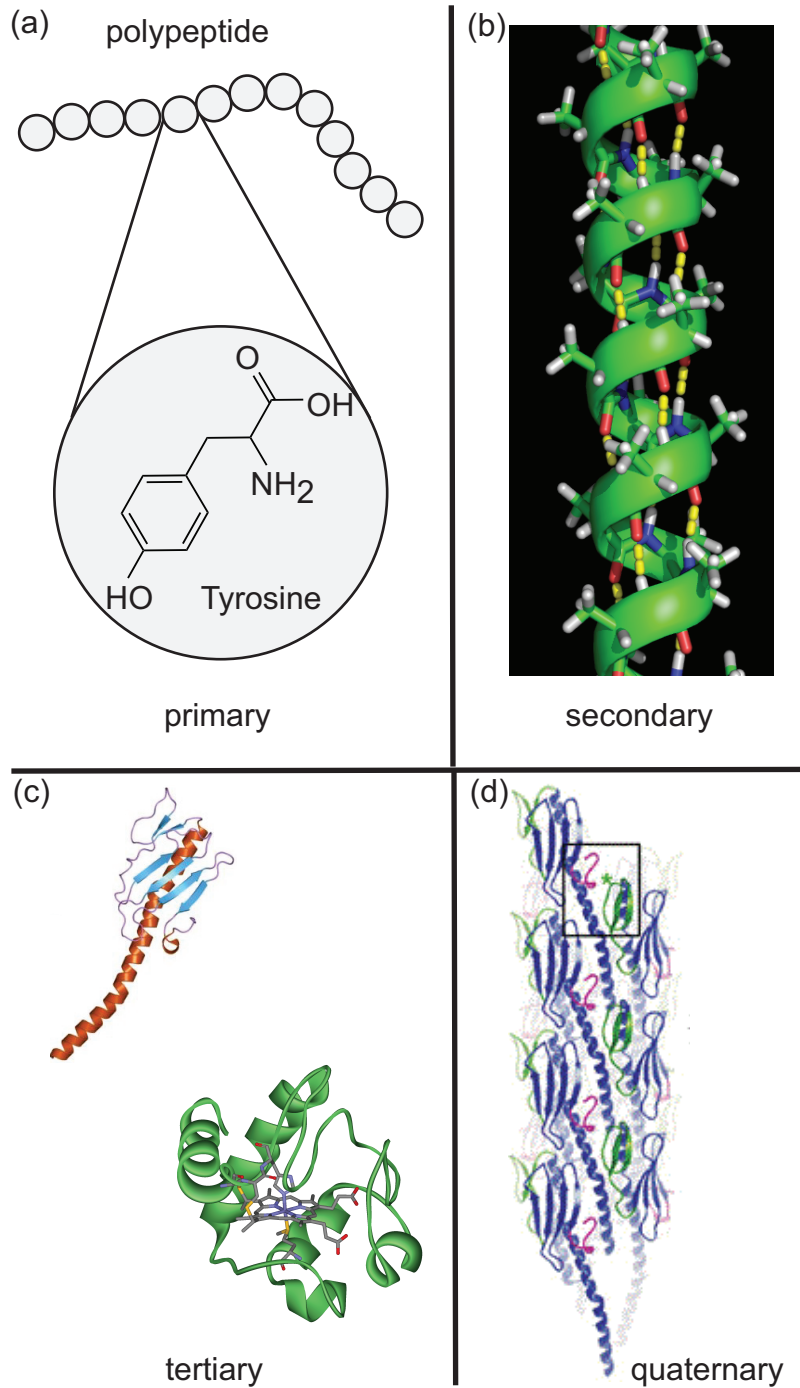


Figure 3.2: Hierarchy of protein structure. (a) Primary structure consisting of a linear polymer of amino acids. Highlighted is tyrosine, which has an aromatic side chain. (b) An example of secondary structure, in this case an α -helix. An atomic stick model is superposed with the ribbon representation. (c) Examples of tertiary structure. PAK pilin subunit (upper) and horse heart cytochrome C (lower). (d) Quaternary structure. Pictured here is the PAK pilus, assembled from multiple pilin subunits. (Part (d): Adapted by permission from Macmillan Publishers Ltd: NATURE REVIEWS MICROBIOLOGY (nature.com/nrmicro) [3], copyright 2004)

discusses the pilus macromolecular structure. Section 3.4.2 discusses common metalloprotein contributions to the electron transport chain of anaerobic microbes. Finally, Section 3.4.3 discusses the feasibility of electron transport in the absence of any metals, along the proton matrix itself.

3.4.1 The structure of *G. sulfurreducens* pili

The pili of *G. sulfurreducens* belong to the type IV class of bacterial pili, which express a quaternary assembly of pilin subunits. The pilin subunit in *Geobacter* is composed of a ~ 60 residue α -helical hydrophobic tail with a short hydrophilic head group (Fig. 3.2). Pilin polymerization is promoted by the hydrophobic attraction among the α -helix tails, and pilin assemble into a larger helical fiber that has a diameter of 2–5 nm. It is possible that the quaternary structure is such that orbitals or bonds are situated to optimize electron transfer upon assembly.

3.4.2 Electron transfer in metalloproteins

Electron transfer outside of the cell of anaerobic organisms may proceed via c-type cytochromes or other metalloproteins—proteins with bound metals. Despite observed metalloprotein participation in *G. sulfurreducens* electron transfer [1], the pili are an integral part of the electron transport chain, as discussed in Section 3.2, which is the reason they are referred to as microbial nanowires. In other reported microbial nanowires, the pilus acts as a scaffold for c-type cytochromes or other metalloproteins arranged in a filament-like morphology [73, 74]. To investigate the possibility that the pili may contain metal cofactors, work in the Reguera lab has analyzed the composition of the purified pili and concluded that

there were no metals present (discussed below).

Purification of the pili [75] removes cellular material and biological debris except the pili themselves, which are then suspended in fluid. Preparation of purified samples removes residual metals from metalloproteins elsewhere in the cell, so that metals do not contaminate analysis of the pilus composition. The presence of pili in purified samples was verified by SDS-PAGE, confocal laser scanning microscopy (CSLM), atomic force microscopy, and transmission electron microscopy (TEM). In SDS-PAGE, molecules in solution are separated according to their charge to mass ratio, which is often sufficient to distinguish proteins. CSLM is an optical microscope that detects fluorescence from molecules attached to antibodies only binding to proteins of interest, in this case binding to sites specific to the pilin subunit. AFM and TEM characterizations further confirmed the presence of pili with little contamination.

Experiments performed in the Reguera lab have eliminated the possibility that metal cofactors are responsible for the conductivity of the pili [75]. Inductively coupled plasma atomic emission spectroscopy (ICP-AES) measured the occurrence of metal atoms in parts per million, and found only trace amounts metallic elements. This suggests that pilus conductivity occurs along the protein matrix itself.

3.4.3 Electron transfer in protein matrix

Electron transfer may proceed along the pilus protein matrix itself, as evidenced by previously discussed biological studies (Section 3.2). Although protein conductivity across such long distances is unprecedented, multistep tunneling processes allow transfer of electrons over more modest distances, as large as 35 Å [16]. While metalloproteins and metal cofactors

commonly participate in the ET processes discussed here, recent studies have shown that amino acids can contribute directly to electron transfer in the absence of any metals [76, 77], perhaps a partial explanation for the finding that there are no metals in the *G. sulfurreducens* pili (previous section).

A generalized model of an electron tunneling from one site to a second may be described by a double well potential, shown in Figure 3.3(a). The electron is situated at the donor site (D), separated by a potential barrier from the acceptor site (A). Electron transfer events depend on direct or resonant tunneling between the two wells or activation over the barrier (hopping). For a symmetric well, average occupation at the two sites is equal. In organic electron transfer, the donor and acceptor sites must be in thermodynamic equilibrium. Thus a proper treatment considers positions of the ions, referred to as the nuclear coordinates. For this reason, the reduction in the Gibbs free energy for a transfer reaction describes what is referred to as the driving force, ΔG^0 . Nuclear motion, as well as reduction and oxidation potentials of the acceptor and donor define the driving force. Marcus theory [78] has been quite successful in describing this process semiclassically, where for non-adiabatic transitions, the rate of electron transfer is given by:

$$k_{ET} = \underbrace{\frac{2\pi}{\hbar} |H_{DA}|^2}_1 \underbrace{\frac{1}{\sqrt{4\pi\lambda k_B T}} \exp \left[\frac{-(\lambda + \Delta G^0)^2}{4\lambda k_B T} \right]}_2 \quad (3.1)$$

For the analyses of SPM data presented in this dissertation, however, we shall concern ourselves only with the implications of Factor 1 above, for which H_{DA} is the electronic coupling matrix element. I will briefly note here, though, that in Factor 2 above, λ is the reorganization energy, which is the energy difference of the nuclear configurations between

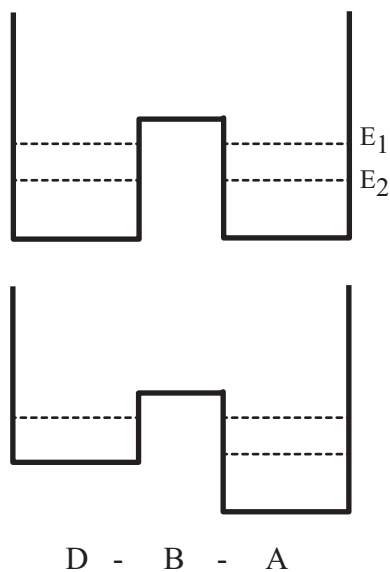


Figure 3.3: Schematic of two-site biological electron transfer reactions in the form of a double-well electronic potential. Upper: symmetric; Lower: asymmetric.

the initial and final states, due to the presence or absence of the transferred electron. The total reorganization energy is a sum of inner and outer sphere contributions, essentially the vibrational and solvent, respectively. The former is often approximated by a harmonic oscillator potential (Fig. 3.3(b)), and the latter demonstrates an influence of the solvent on transfer rates. Thus the nuclear coordinates must also be in resonance for an electron to tunnel. A conclusion from Equation 3.1 is that the transfer rate has a maximum when the driving force equals the opposite of the reorganization energy. From here on, we shall concern ourselves only with Factor 1. If we assume fixed D and A positions relative to the rest of the protein matrix, then Factor 1 incorporates the D-A distance dependence and temperature dependence of the electron transfer rate.

For fixed D and A positions the coupling $H_{DA} \propto e^{-\beta r}$ [79], where r is the distance between D and A. The decay constant, β , is determined by the character of the protein matrix between D and A, called the bridge (B), and the electron is transferred via superexchange

tunneling. In the field of biological ET, superexchange does not refer to the solid state definition of spin coupled process, but rather describes a process by which the intervening bridge molecules enhance the coupling between D and A without specific regard to spin. Here, we ignore the details of the intervening medium and focus on typical resulting transfer distances cited in the literature. Typical β -values range ~ 1.0 – 1.4 \AA^{-1} , but the dominant variable is the D-A separation. Because the rate decays exponentially with separation, as the distance increases, the rate will eventually become too slow to be biologically relevant. This means that although tunneling still occurs, albeit at a lower probability, the flux of electrons is too small to be useful in the biological process. Approximations for the fundamental distance limit for tunneling range from 14 \AA [80] to 20 \AA [76].

The maximum distances that the related process of multistep tunneling can achieve often eclipse those of superexchange tunneling. In multistep tunneling, the electron resides on intermediate states momentarily before moving on to the acceptor, contrasting superexchange where intermediate orbitals simply change the decay rate of a single coherent tunneling event. One class of these processes is electron hopping along aromatic side chains, with several experimental findings reported. In one set of experiments [81], substitution in an ET peptide of an aromatic residue decreased the transfer rate across the maximum 20 \AA distance by a factor of 20–30 versus the protein with a non-aromatic knockout substitution, suggesting that tunneling would remain biologically relevant across farther distances. Other experiments have corroborated aromatic hopping assistance, commonly via residues from the amino acids tryptophan (Trp) or tyrosine (Tyr), and sometimes associated with proton-coupled electron transfer [82, 83, 84, 85, 86, 87]. Electron transport via a multistep hopping mechanism allows transfer distances as far as 35 \AA [16].

If electron transfer were to proceed along the protein matrix in the pili of *G. sulfurreducens* then it is feasible that it would involve superexchange or hopping processes. A preliminary model of the pilin subunit shows aromatic Tyr residues situated with a spacing of 2–12 Å [88], a distance that favors electron transport via a hopping mechanism [87]. Polar amino acid residues (arginine and lysine) can also be found in the vicinities of the Tyr residues and may influence the unoccupied electronic states in the aromatic residues to optimize the chance of electron occupation [87]. The *Geobacter* pili are presumed to transfer electrons at distances exceeding 35 Å by perhaps as much as three orders of magnitude (see Chapter 6). Superexchange and hopping processes alone will not be sufficient to account for this. Speculatively, an explanation of such long-range transfer may need to consider quasiparticles such as polarons, where the polarization field would provide a feedback mechanism, or Davydov solitons [89], a type of acoustic polaron specific to α -helices. Others in our collaborative effort have recently begun modeling the pilus morphological and electronic structure using linear scaling density functional theory.

3.4.4 Experimental potential

The hypotheses of long-range electron transfer along the protein matrix in *G. sulfurreducens* use established biological ET theory and observations as foundations. However, a complete understanding of the long-range process would perhaps require a new mechanism to explain transfer farther than 35 Å. Scanning probe microscopes have high electronic sensitivity coupled with spatial resolution an order of magnitude better than the length-scales of the molecule and the hypothesized ET mechanism transfer limits. Previous CP-AFM measurements [1] were taken from mechanically sheared pili—samples in which remnant metals and

debris remained and the pili were not isolated. New scanning probe experiments may be applied to samples with purified pili to examine conductivity of the protein matrix alone.

The scanning tunneling microscope may be employed to test the conductivity of the protein matrix in isolated pili from purified samples. The configuration of donor and acceptor states should be such that charge pathways exist in the molecule, not only along its axis, but also along its diameter between the STM tip and a conducting substrate. Tunneling spectroscopy in this configuration can tell us something about the local density of states of the electronic system. Moreover, the spatial sensitivity of the STM allows a congruent spatial map of the conductivity and tunneling spectra across the entire imaged region of the molecule. Presumably, “hot spots” of conductivity, heretofore termed donor and acceptor sites, may be imaged with nanometer resolution, consistent with intraprotein tunneling distances. I will discuss experiments of this nature in Chapter 5.

While STM analysis focuses on transverse conductance, it does not directly probe the long-range electron transfer believed to take place along the pilus axis. We may use another electronically sensitive scanning probe—CP-AFM—to measure conductivity of a pilus that bridges the tip with a distant electrode. Because the bridging pilus must lie upon an insulating substrate, AFM can image both insulating substrate and conducting electrode in topographic mode to find the pili, at which time the conductive tip may measure pilus conductivity. I will discuss the development of this experiment in Chapter 6.

Chapter 4

Filament-like artifacts on graphite

Highly oriented pyrolytic graphite (HOPG) is a common substrate for STM and AFM studies of biological molecules [1, 73, 90]. It is an ideal surface for STM because it is easily cleavable by adhesive tape, resulting in large, atomically flat planes that are relatively inert and electrically conductive (see Chapter 5.1.2). Typical planes range in size from hundreds of nanometers to tens of microns with single atomic layer steps. Despite these attractive attributes, the cleavage of HOPG surfaces also generates a variety of artifacts, many of which are filamentous structures similar to DNA and other biological molecules [91]. Some even exhibit periodicities that mimic helices and other substructures expected in filamentous biological molecules [91, 92, 93, 94]. Because the primary substrate used in the STM studies presented in this thesis has been HOPG, I observed and catalogued many of these commonly known filament-like artifacts. The presence of these artifacts demands a careful interpretation of STM images, to appropriately identify filamentous biological molecules when HOPG is used as a substrate. The data presented here serve as a demonstration for how we differentiated pilus nanowires from filament-like graphite artifacts in STM experiments. STM

imaging and spectroscopy of the pilus nanowires themselves will be presented in Chapter 5.

Because the scanning tunneling microscope is a powerful probe with high spatial resolution for studying the surface topography [95] and electronic properties [19, 96] of biological samples, it has drawn considerable interest from researchers wishing to study many biological molecules. One particular molecule of interest is the filamentous molecule, DNA. Soon after the invention of the STM, researchers postulated that it may be used to sequence DNA with more accuracy than with traditional techniques [90, 96, 97, 98, 99]. This effort has led to successful development of functionalized STM tips that differentiate individual nucleosides [25, 100] However, the filament-like artifacts on the graphite surface, some of which were periodic, complicated these studies.

Likewise, the size, structure, and periodicity of pili from *Geobacter* bacteria are expected to produce topographies resembling those of common artifacts on the surface of HOPG. These pilus nanowires are protein filaments that are 2–5 nm in diameter and are formed through the periodic self-assembly of a single, small peptide subunit. Despite the limitations imposed by its artifacts, graphite remains an attractive substrate for pilus deposition and probing. For this reason, I conducted an investigation of HOPG artifacts by STM generated during biological deposition of pilus nanowires. In addition to graphite artifacts previously described in the literature [91, 92, 93, 94, 101, 102], we identified two types of artifacts on the surface of freshly cleaved HOPG that bore a resemblance to conductive biological filaments [103]. These artifacts have not been described or characterized in this detail or context before. The first is a fiber structure, and the second is a periodic, zipper-like structure.

In the following chapter, I give an overview of common graphite artifacts and then discuss the characterization of the novel fiber and zipper graphite artifacts by STM. The results

presented here demonstrate that HOPG surfaces produce artifacts that are structurally similar to microbial nanowires, but also that they can be differentiated, thereby enabling the application of STM methods to the study of conductive biological structures.

4.1 Materials & Methods

In general, sample preparation followed the protocols for STM study of pili outlined in Chapter 5.1. When indicated here, biological sample deposition was followed by chemical fixation for five minutes with a 1% solution of glutaraldehyde in phosphate buffered saline (PBS). Aspiration and drying proceeded as in 5.1. Controls with bare HOPG that lacked biological samples or solvent treatment were placed in the STM chamber within minutes after cleaving. The two microscopes used to acquire data in this chapter were described previously (2.3.1 and 2.3.2). The Nanosurf STM imaged the common artifacts shown here except Fig. 4.2(a) and (b), and the cryogenic STM imaged all other artifacts at room temperature.

The STM tips used in this study varied. An electrochemically etched tungsten tip was used to image carbon fiber artifacts in samples that underwent biological deposition. A mechanically cut Pt:Ir (80:20) tip was used to image clean graphite and common artifacts. An etched, ion-milled Pt:Ir (80:20) tip was used to characterize zipper artifacts.

Experimental Procedure

We used STM to scan dozens of graphite surfaces. The prepared surfaces fell into three categories: bare HOPG, HOPG negative control, and HOPG covered with biological samples (cells expressing pilus nanowires). The negative control samples were HOPG surfaces prepared in the same way as the samples undergoing biological deposition, but without cells

or pili present in the growth media. In general, HOPG surfaces with biological deposition were sparsely covered with intact cells, pilus nanowires, and cell debris. In order to locate and identify the pilus nanowires, we examined a high number of large scan areas. Scanning continued until a conductive filamentous structure (a pilus nanowire or an artifact) was imaged and characterized. As a surface and calibration control, we also performed similar scans on bare graphite. A result of this large number of samples across the three categories of surface preparations was a collection of common and rare HOPG artifacts. Two, in particular, that may possibly be mistaken for biological filaments, such as microbial nanowires [1, 73] were further studied. The artifacts included a fibrous carbon structure (Section 4.3) and a zipper-like structure (Section 4.4).

4.2 Common artifacts

Several STM observations of filament-like artifacts on graphite have been catalogued in the literature [91, 92, 93, 94, 101, 102]. I encountered many of these during STM studies of graphite surfaces that were bare and surfaces that had biological deposition. These include buckled graphite sheets [92, 104], (Fig. 4.2), step edges with substructure (Fig. 4.1), grain boundaries [93], (Fig. 4.1), and creases of folded-over graphite sheets. Here I discuss a few of these in particular.

First, the rather simple and abundant step edge formations found in virtually every STM scan can occasionally appear to the STM to be more than just the edges of carbon sheets. Single atomic step edges are rather easy to identify because of their small height of just a few angstroms, but edges of several graphite sheets may be as high as several nanometers. These stacked sheets will often give the illusion of structure when the break

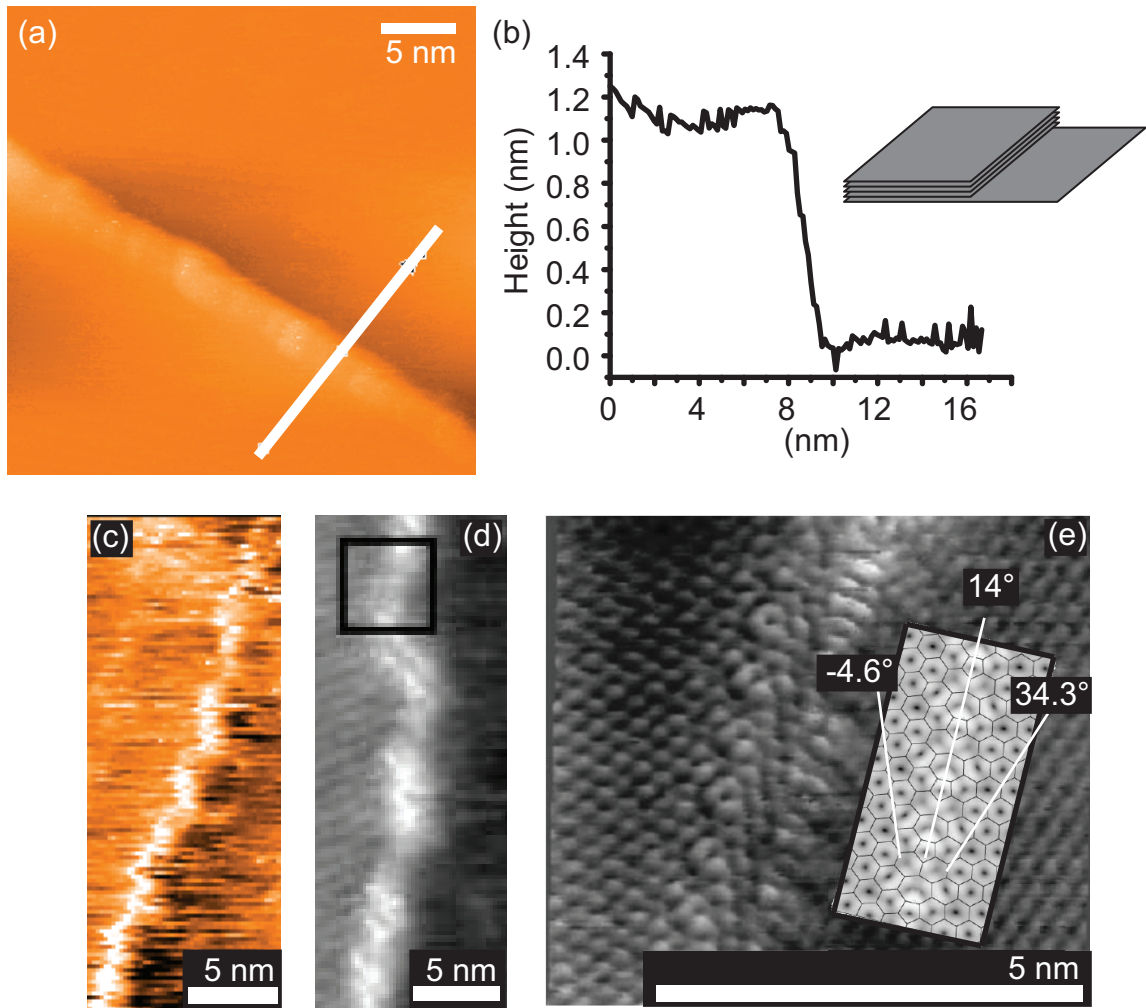


Figure 4.1: (a) STM topograph of a rough step edge. As evident in the profile in (b), the edge is several layers in height. To produce the plot, a best fit line in the direction of the cut was subtracted to correct for the background slope. This subtraction makes the step edge easier to identify. A cartoon of the step edge is also shown in (b). (c)-(e) Grain boundaries on HOPG. (c) Representative topograph of grain boundaries encountered during our studies. (d) Grain boundary resembling that in (c) [4]. (e) Atomic resolution topograph of the same grain boundary at the location of the box in (d). (inset): Lattice planes at shifted angles superimposed over a simulated STM image for a grain boundary.

is not straight. Especially with image processing artifacts such as line by line subtraction, the edge may appear to have the structure and depth of a filamentous object. Figure 4.1 shows an example of such an object. The step height in Fig. 4.1 is three times graphite's interlayer spacing of 3.3 Å, indicating that this step is a height of three stacked layers. The rounded and jagged breaks on the edge mimic the edge of a filamentous object adsorbed on the surface. Line by line subtraction, an image post-processing function that is often performed by the software during data acquisition, gives the illusion of depth. Furthermore, a reproducible and anomalous electronic structure at the step edge is imaged by the STM. With care, even these intricate step edges are easily identified. Fig. 4.1(b) shows a line cut taken across the edge, in which a background best line fit was subtracted along the direction of the profile, resulting in a height plot of the step edge with well defined flat upper layer and flat lower layer. This is a typical and rather straightforward method whereby step edges are differentiated in our analyses.

Another common artifact occurs at grain boundaries. These occur at interfaces of graphite grains, which have dimensions on the order of microns. Most grain boundaries are not imaged without atomic resolution. In Figure 4.1(c-e), I show that grain boundaries may exhibit electronic structure that has a periodicity mimicking a helical filament-like molecule. In this case, the surface is flat, but the electronic structure leads to an apparent height that is finite in the STM imaging. This phenomenon is described in Reference [93]. The feedback loop of the STM in constant current mode will pull the tip away from the surface when it detects current exceeding the set point. Because the imaging software plots this as a topographical height, the electronic structure leads to an imaging artifact that looks like an adsorbed filament. Often, these artifacts have an apparent height of just a few

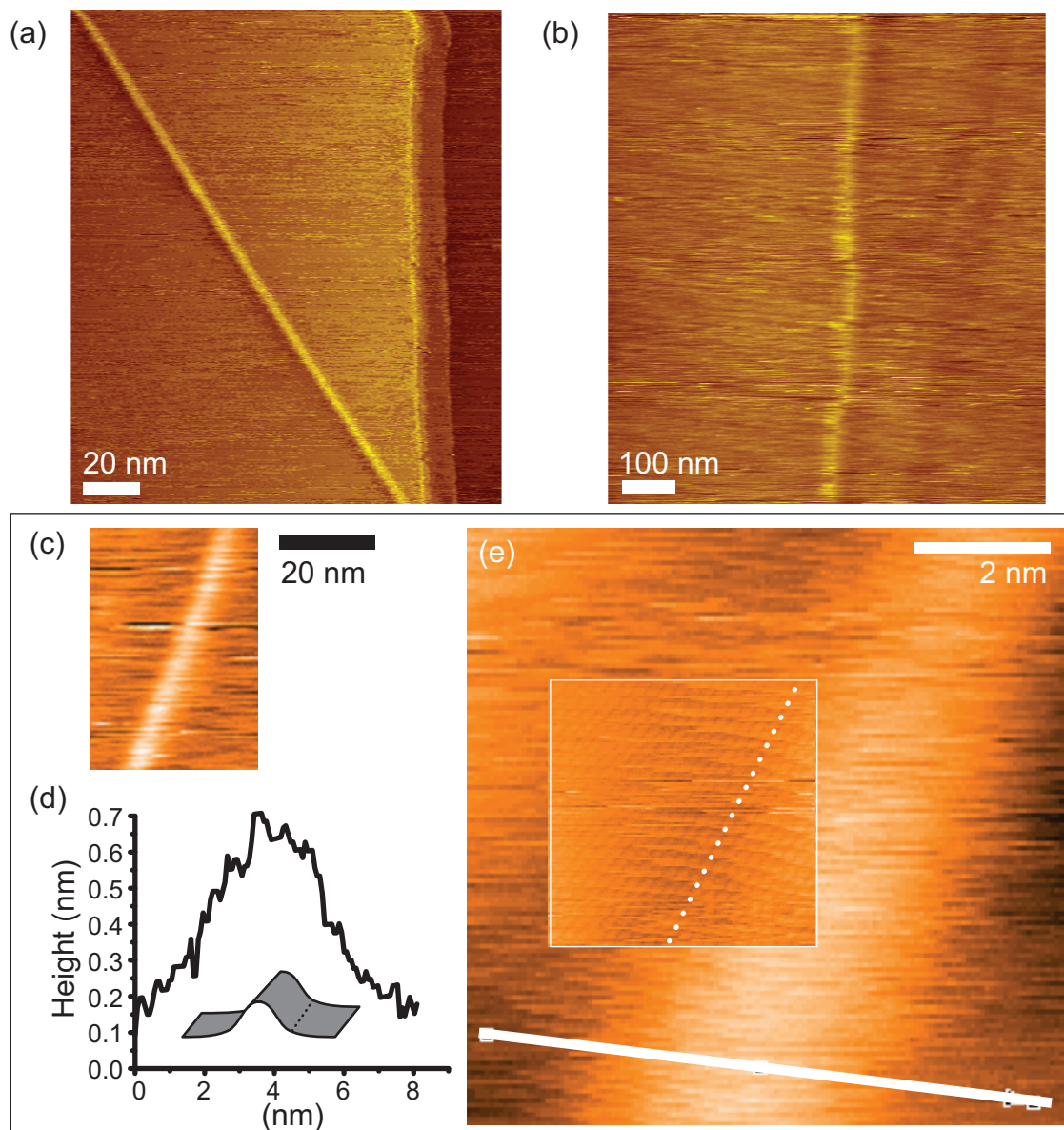


Figure 4.2: Series of STM topographs of buckled graphite sheets. (a) and (b) are examples of these oft-observed filament-like features. (c)-(e) One particular buckle examined in more detail. (d) Buckle cartoon and profile taken at the location of the line cut denoted in (e). (e) Atomic resolution topographs of the buckle. The inset is sized to scale and is placed at the approximate location at which it was taken subsequently at higher resolution.

angstroms, in contrast to microbial nanowire apparent heights of 10–15 Å (Chapter 5) and may be identified with proper care. A conclusive way to do this is to image the object with atomic resolution so that the change in lattice orientation is easily seen in the topography (Fig. 4.1(e)).

Perhaps the most prevalent of the artifacts that may be mistaken for microbial nanowires, faint filament-like objects that are microns long and on the order of 1–10 nm wide, litter the surface, appearing roughly once per five maximum STM scan areas with the Besocke instrument ($5\ \mu\text{m} \times 5\ \mu\text{m}$). These are quite common on both bare graphite surfaces and biologically-covered graphite surfaces. When these objects are examined in detail, as I show in Figure 4.2, they appear to be buckled graphite sheets, with similar appearance to those described in [92] and also to the buckled graphene sheets described recently [104]. These artifacts are often hundreds of nanometers long and range from 3–20 Å in height. In Figure 4.2(f), I show an atomic resolution topography of such an object. Other than this atomic lattice, there is no detectable substructure. Imaging the edges and on top of the buckle, one still observes the graphite lattice, indicating this is a graphitic structure.

While all of these common artifacts have become easy to discern when searching for adsorbed microbial nanowires, other artifacts, discussed in the next two sections, are less common. The discussion that follows will demonstrate that despite a familiarity with common artifacts, every object must be carefully examined for graphitic properties.

4.3 Fiber Artifact

Figure 4.3 shows a set of images of conductive filamentous artifacts taken in the same $3\ \mu\text{m} \times 3\ \mu\text{m}$ area of a HOPG surface that was fixed with the glutaraldehyde after de-

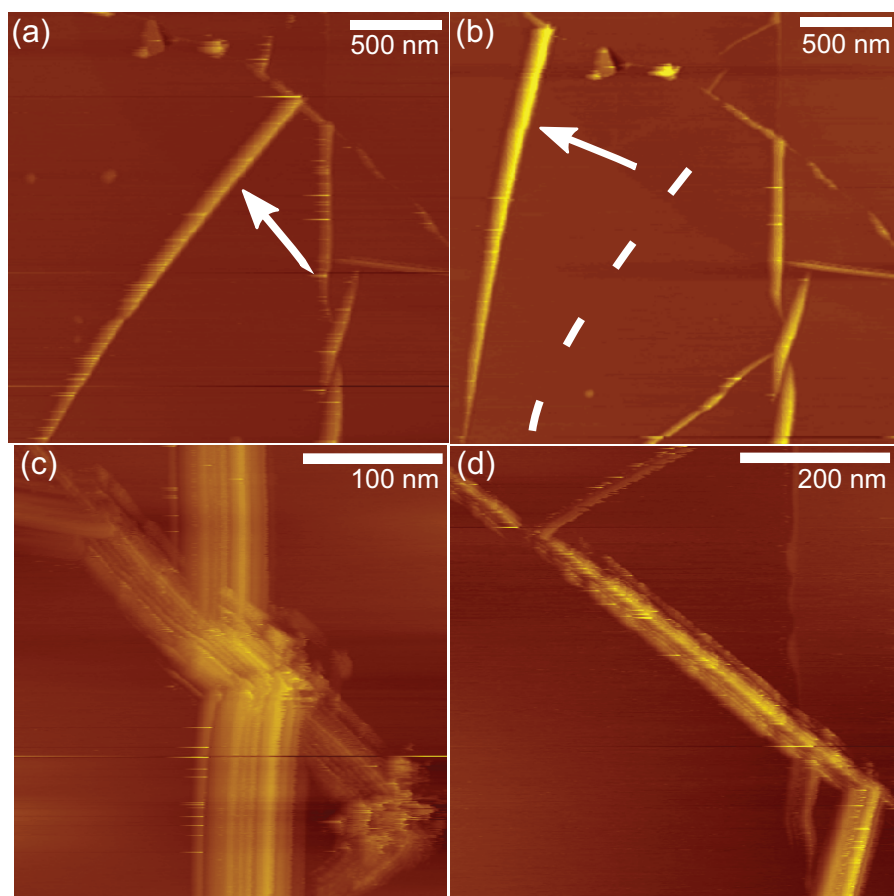


Figure 4.3: Series of scanning tunneling microscopy topographs of a region of the HOPG surface having disturbed graphite sheets ($V=-400$ mV, $I=-50$ pA). STM image taken before (a) and immediately after (b) the tip pushed one of the fibers across the surface (denoted by arrows). Both (c) and (d) were taken in the vicinity of the region in (a) and (b). (c) Higher resolution STM topograph of filament junctions. The sharp angles and rigid structure are more characteristic of HOPG artifacts than biological material. (d) Another high resolution topograph. The structure follows or originates from the step edge.

position. Fixation is a chemical treatment that preserves the basic structure but prevents decomposition. Because the protocol followed for the biological deposition does not covalently attach the biological sample to the surface, pilus nanowires can, in principle, be moved across the surface by typical tip-surface forces. We have used this property to discriminate pilus nanowires from common graphite artifacts such as grain boundaries and buckles. Like biological nanowires, the fiber artifacts were not attached to the HOPG surface, and could be displaced by the STM tip (Fig. 4.3(a-b)). Although the fiber artifacts were effectively displaced by the STM tip, they maintained their rigid structure. This contrasts with the flexible nature of biological structures such as the pilus nanowires of *G. sulfurreducens*, which show curvature changes during tip scans [105]. This is an effective way to discriminate between graphite artifacts and pilus nanowires. At higher magnification, the conductive fibers had the appearance of bundles comprised of multiple filaments, each having a width of ~ 5 nm (Fig. 4.3(c-d)). Abrupt breaks also were noticeable in some of the fiber artifacts. Figure 4.4(a) shows a higher resolution topography of one of the fiber artifacts described in Figure 4.3. A cross section of the fiber (Fig. 4.4(b)) is representative of the typical fiber dimensions—heights of 10–15 nm and widths ranging from 50 to 100 nm. Tunneling spectroscopy also suggests that this was a graphite artifact. As shown in Figure 4.4(c), I - V curves obtained from a point on top of the fiber and one on the surrounding graphite, roughly 50 nm away on the HOPG surface, were similar, both exhibiting the same characteristic graphite shape.

The bundled appearance could be misinterpreted as a bundle of bacterial pili, as previously reported [73]. However, evidence to date indicates that bundled pili do not cluster or aggregate in a way that results in collimated rows [106]. Biological helices and suprahe-

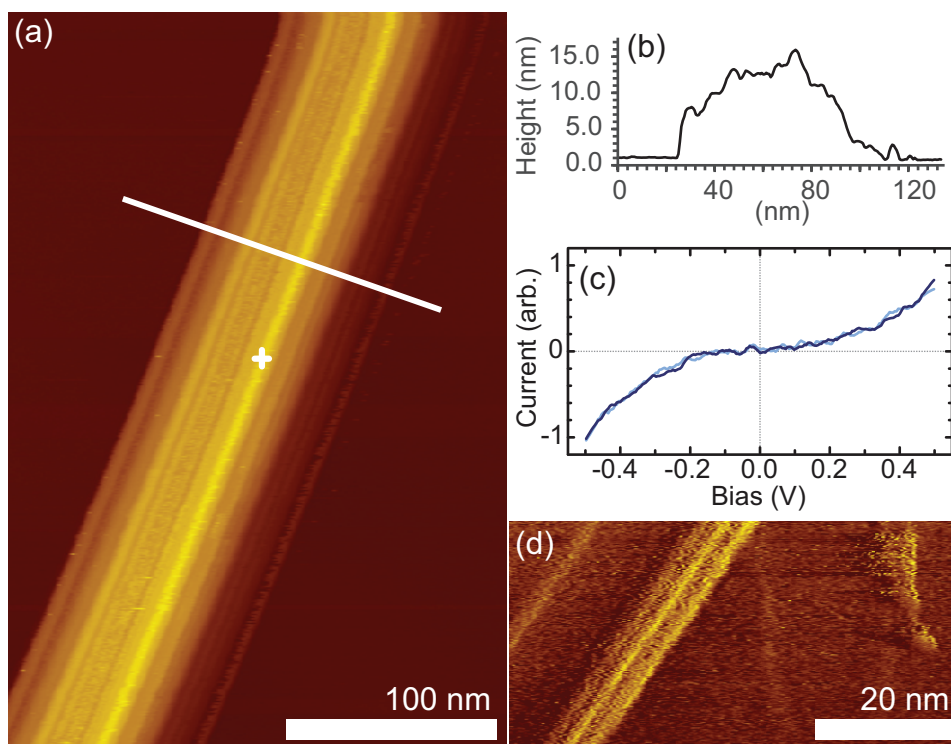


Figure 4.4: STM topographs of fibrous artifacts on the surface of HOPG. (a) High resolution image of an artifact observed on the surface of an inoculated and fixed sample in the same region shown in Figure 4.3 ($V=-400$ mV, $I=-60$ pA). The line denotes the location of the profile plotted in (b). A multi-tip effect may be contributing to the observed width of ~ 80 nm. (c) Representative normalized $I-V$ spectroscopy curves. Each is an average of ~ 40 curves with 13-point S-G smoothing. The darker line is a curve taken on the section of the fiber marked in (a). The lighter line is an $I-V$ curve of the flat HOPG next to the filament. The two curves do not have any distinguishable differences. (d) STM topograph of a similar artifact observed on the surface of a bare freshly cleaved graphite control sample ($V=50$ mV, $I=1$ nA).

lices such as pili and pili bundles, respectively, often exhibit supercoiling or twisting [107], which prevents the collimated arrangements observed in the fiber artifacts. Furthermore, the artifacts were consistently observed in areas close to torn graphite sheets and folded step edges (Fig. 4.3). This, and the fact that the filaments had sharp angles and rigid structures, suggests that the objects were graphitic. To further confirm the graphitic nature of the fiber artifacts, we scanned freshly cleaved graphite that had not been exposed to biological deposition or solvents. As shown in Fig. 4.4(d), similar structures were identified on the surface of bare HOPG controls. The bare graphite fiber was also a bundle of filaments that were each roughly 5 nm wide. When found on the surface, the substructure of these objects are resolved to varying degrees, but they occur in roughly 10% of the maximum Besocke STM scan ranges. Fibers as large as those in Fig. 4.3, however, are more rare. Cleaved graphite can form rigid rod-like structures like nanotubes and fibers [108]. However, the fiber artifacts characterized here have not previously been described. The structural and topographical features of the fiber artifacts imaged by STM were remarkably similar to the nanowires reported for *Shewanella oneidensis* and other bacteria [73]. Thus, careful analyses and characterization are required to discriminate fiber artifacts from nanowires in these organisms when using STM. Structural rigidity and the presence of sharp angles and abrupt breaks such as those shown in Figures 4.3(c-d) are good indicators of fibrous graphite artifacts rather than soft biological molecules and can help discriminate between the two.

4.4 Zipper Artifact

We also identified a long filamentous structure resembling a zipper on a surface that was not chemically fixed (Fig. 4.5). The object was microns long and had a periodicity of 6.5 nm

when measured in a cross section along the axial direction. The symmetric periodicity and dimensions were inconsistent with any known conductive biological structures. Furthermore, the width of the zipper structure (~ 15 nm) was larger than the apparent width of pilus nanowires (6–10 nm) (Chapter 5.2). This larger width is unlikely to have resulted from a tip broadening effect because the edges of the object had features that were defined with nanometer resolution. A multiple tip effect is also unlikely because the small topographic features did not repeat in the image, most notably the small, 1-nm dots repeated along the lower right side (Fig. 4.5 (b-c)). Furthermore, the object was quite straight and had a rigid appearance, which contrasted with the slightly curved and flexible pilus rod [105]. Although the pitch of the object in Figure 4.5 is roughly consistent with that of the pilus (Chapter 5.2), we see no deviations from this pitch larger than a few angstroms. This is in contrast to the larger uncertainty in the pitch of the soft pili, which is often 10–20 angstroms (Chapter 5.2). Lastly, the imaged zipper filament did not interact with the tip and could not be displaced. Although it may have been pinned to step edges at several locations, thereby preventing it from being pushed, tip-induced displacements are still expected in the middle regions of a biological nanowire because of their flexible nature. However, the tip did not displace the structure in any way at any point along the length probed.

The filamentous zipper structure presented in Figure 4.5 has a morphology resembling that reported for grain boundaries (Section 4.2, [101, 102]). However, it has more substructure than any artifact previously reported in the literature. In those reports, authors showed that torn sheets of graphite rotated at specific angles relative to one another, which resulted in the formation of an interface that was imaged by STM as a filament-like periodic grain boundary. However, at the time of our acquisition of this object, the tip could not resolve the

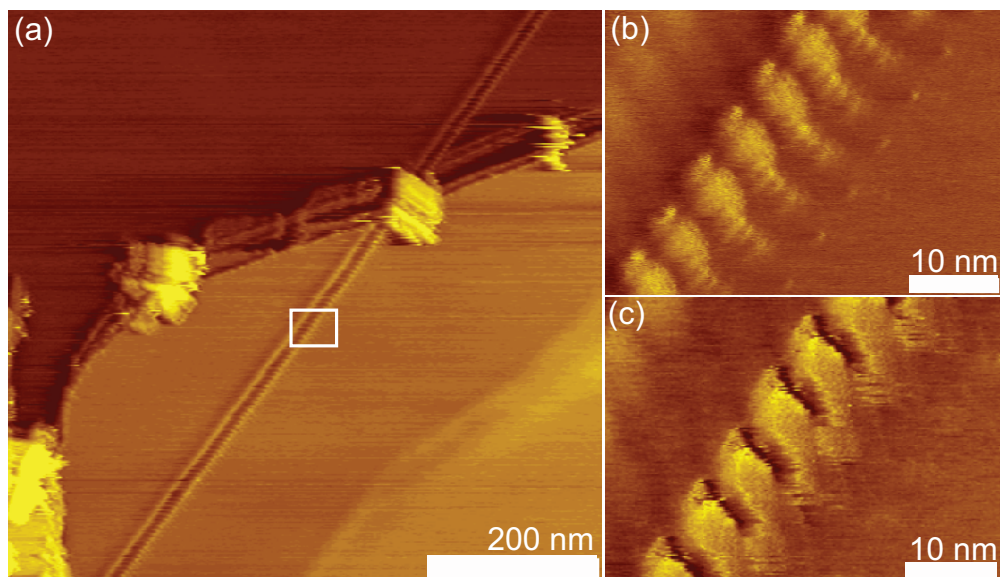


Figure 4.5: STM topograph of a zipper structure. The box in (a) denotes the region scanned in (b) and (c) ($V=1$ V, $I=100$ pA). The structure appears different in (b) and (c), presumably due to changes in the tip configuration while scanning. This structure was observed just once, and due to its rarity, it has not been observed on HOPG controls that were bare or exposed to solvents only. It also does not resemble the *G. sulfurreducens* pilus nanowires that we have observed on multiple inoculated samples (e.g. Chapter 5). The object appears to be pinned to a step edge and is straight and rigid, in contrast to the observed appearance of the pili.

atomic lattices, which could help address this possibility. Also, this was an extremely rare artifact. The structure was observed only once in the course of experiments that included the scanning of several $4\ \mu\text{m} \times 4\ \mu\text{m}$ fields for each of dozens of samples undergoing biological deposition and dozens of samples of bare graphite. The artifact was observed in one of the fields scanned among the samples that had undergone biological deposition. Thus, we could not rule out the possibility that the deposition method contributed to the formation of this artifactual structure.

4.5 Conclusions

The increased use of scanning probes to investigate the electronic properties of filamentous biological structures, such as microbial nanowires, prompted us to investigate the presence of filament-like artifacts on the surface of cleaved HOPG. In addition to the common and well-catalogued filament-like artifacts, I also described two previously undescribed graphite artifacts that could be mistaken with biological nanowires because of structural or topographic similarities or because they were observed on surfaces that had undergone biological deposition.

Step edges, grain boundaries, and graphite buckles were common on the surface of cleaved graphite. I observed several examples of each of these artifacts on samples undergoing biological deposition, as well as negative controls and bare graphite. Careful analysis and familiarity with these common artifacts facilitates their identification in STM study of biological molecules.

One of the newly described artifacts, a fibrous carbon filament, was often observed on bare, freshly cleaved HOPG surfaces as well as those undergoing deposition. This indi-

cates that HOPG cleavage, rather than biological deposition, contributed to its formation. Although the tip could push the fibers across the surface, they lacked structural characteristics of biological nanowires and had an indistinguishable spectroscopic signature with the surrounding graphite. In contrast, the rare periodic zipper structure was rigid and had distinguishable structural features that enabled its discrimination from STM images of biological molecules, especially those of the pilus nanowires produced by *G. sulfurreducens* (Chapter 5). These results demonstrate that the surface of cleaved HOPG contains artifacts that resemble biological nanowires when imaged with STM. However, a careful examination of unique structural and spectroscopic features enables their identification. This, in turn, facilitates STM approaches for the study of biological nanowires on graphite.

Chapter 5

STM study of pilus nanowire electronic properties

In an effort to elucidate the nature of the conductivity in the pilus nanowires of *Geobacter sulfurreducens*, we used STM to probe the local density of states of pili deposited onto a conducting substrate [109]. In such a configuration, we measured not length-wise transport, but rather transverse conductance in the tip-molecule-substrate direction, perpendicular to the pilus axis. The high spatial resolution of STM combined with the ability to probe the energy spectrum of electronic states allowed for imaging of molecular substructure and an analysis of the spatial dependence of the local electronic density of states (LDOS) of the pilus (Chapter 2.1.2).

5.1 Materials & Methods

5.1.1 STM and AFM Measurements

Within minutes after deposition of the sample onto a substrate (Section 5.1.2), or after removal from storage in a nitrogen box, samples were placed in the cryogenic STM chamber, which was under dry nitrogen or high vacuum (Chapter 2.3.2). Though the nature of the solvent for molecules *in situ* can influence conduction properties (Chapter 3.4.3), dry proteins (solid-state) have been shown to conduct as well or better than those in moist environments [110]. A thin layer of water may also remain around a “dry” molecule. Therefore, in our depositions of pili that subsequently dry out, the STM tip can still probe the electronic states contributing to conduction, but analysis should acknowledge potential differences in properties when dry and when in moist environments.

Experiments discussed in this chapter were performed at room temperature. Most proceeded in dry nitrogen gas, using commercial electrochemically etched Pt:Ir (80:20). Samples with cells expressing pili were scanned in high vacuum ($\sim 10^{-6}$ torr) with cut Pt:Ir (80:15) tips. Tips were tested on HOPG for sharp profile and the expected electronic structure. For imaging and spectra of pili, we used a small tunneling current set point (typically 50–100 pA) to keep the tip relatively far from the sample and minimize its influence on the electronic states in the pilus and its mechanical deformation. When not in use, samples were stored in dry nitrogen atmosphere.

5.1.2 Sample Preparation

The appropriate sample preparation protocols required some important considerations. Deposition needed to result in sub-monolayer coverage for clear and individually resolved molecules, and the STM required a conductive substrate to allow the pili to be biased via the surface. Sub-monolayer coverage was desirable so that individual pili could be clearly distinguished from the surrounding surface. Sparsely populated samples, however, with fewer than one pilus in an area of $5\ \mu\text{m} \times 5\ \mu\text{m}$, required a time consuming search algorithm in which scanning would have to be stopped, the sample shifted, and then brought back into range. We therefore sought protocols resulting in a reasonable balance (Section 5.1.2). The sample growth and deposition protocols used in our studies were derived from those developed previously for transverse CP-AFM experiments [1]. The purification protocol has been developed more recently [75] by collaborators in the Reguera lab to remove all biological material except pili. Moreover, we found that the purified pili preparation greatly reduced or eliminated the amount of contamination impeding STM study. We shall discuss this below, followed by a discussion of substrate requirements.

AFM topographic imaging was performed in ambient environment with a Dimension Instruments 3100 scanning probe microscope in tapping mode. Samples of cells expressing pili and purified pili were imaged with silicon probes (Veeco) having nominal spring constants of 42 N/m and 0.2 N/m, respectively.

Growth and Deposition

A schematic of growth and deposition steps is shown in Figure 5.1. First, an anaerobic tube of fresh water with fumarate and acetate media (FWFA) was inoculated by transferring

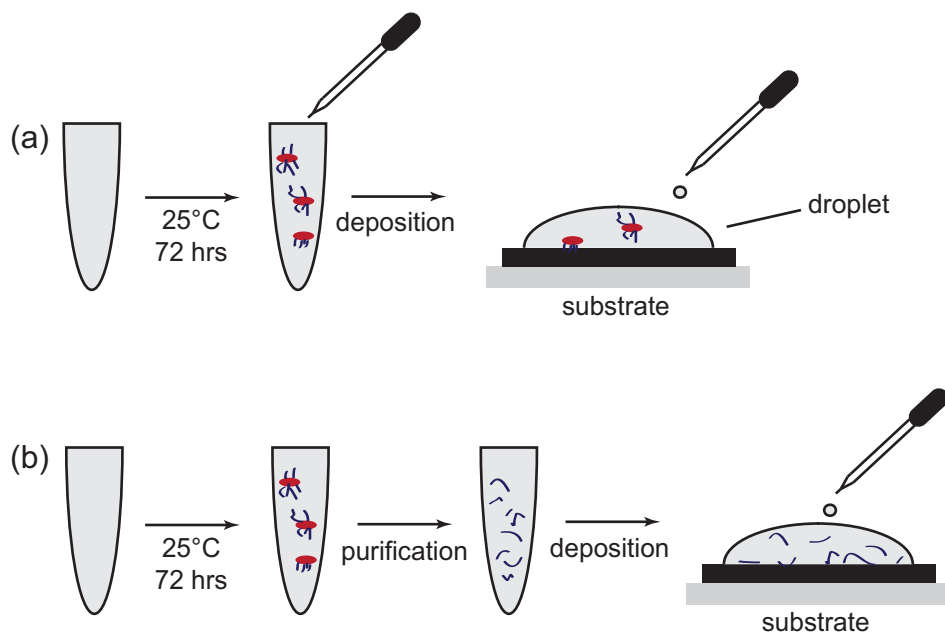


Figure 5.1: Schematic for deposition of samples in STM study of (a) cells and pili and (b) purified pili.

from an existing *Geobacter sulfurreducens* culture. Then, the tube was incubated at 25° C for 72 hours—growth conditions that optimized pilus growth [1]. Samples were then either deposited directly onto the substrate at this point (as below) or taken for pili purification. We took no steps to chemically adsorb the pili to the substrate, so the physical adsorption is likely due to the van der Waals force.

A Pasteur pipette deposited a droplet onto a small (~5 mm x 5 mm) graphite chip and left 15–60 minutes for pili to diffuse towards the surface and adsorb. Droplets consisted of either cells and pili (suspended in growth media, FWFA) or pure pili (in phosphate buffered saline (PBS)). The surface was then rinsed twice with anaerobic wash buffer or PBS to remove excess salts while maintaining the same pH. Excess moisture was then aspirated and gently wicked dry with absorbent paper. For cells expressing pili, this procedure was carried out in a nitrogen glove bag; for purified pili, this was carried out in ambient atmosphere.

As a control (Section 5.5), non-conducting pili from the bacterium *Pseudomonas aeruginosa* K strain (PAK) were purified following the method of [111]. Deposition of PAK pili suspended in PBS buffer proceeded in the same manner described for deposition of purified *G. sulfurreducens* pili.

STM experiments—which require a conductive sample—were complicated if insulating material was present. For samples composed of cells expressing pili, insulating debris from the culture and remnants from the growth media and buffer remained, even after rinsing (Fig. 5.2). The tip could also crash into the insulating cell bodies themselves. A significant tip crash almost always resulted in the need to change the tip. Because of the infinitesimal probability of landing a new tip in the same micron sized location, a permanent loss of a potentially interesting area of the sample would result. In practice, even when the tip interacted only minimally with insulating debris, the tip quality degraded over time until the development of unstable tunneling currents or double tips (Chapter 2.2.3). This degradation was likely a combination of tip damage and biological contamination of the tip itself.

In our samples with cells expressing pili, the optimal balance between minimal cell concentration and sufficient pili concentration was an experimental disadvantage when compared with the purified samples. This was quantified during surface characterization by AFM (Figure 5.2). Adjustment of pilus concentration to improve statistics for STM location and identification came with a corresponding increase in the concentration of large insulating cells and other biological debris. Moreover, the rate of pilus occurrence was comparable to the rate of filament-like artifact occurrence (Chapter 4). In addition, the AFM characterization likely underestimated the number of pilus candidates for STM study. This is because the STM tip often pushed filaments across the surface, likely due to the larger forces between

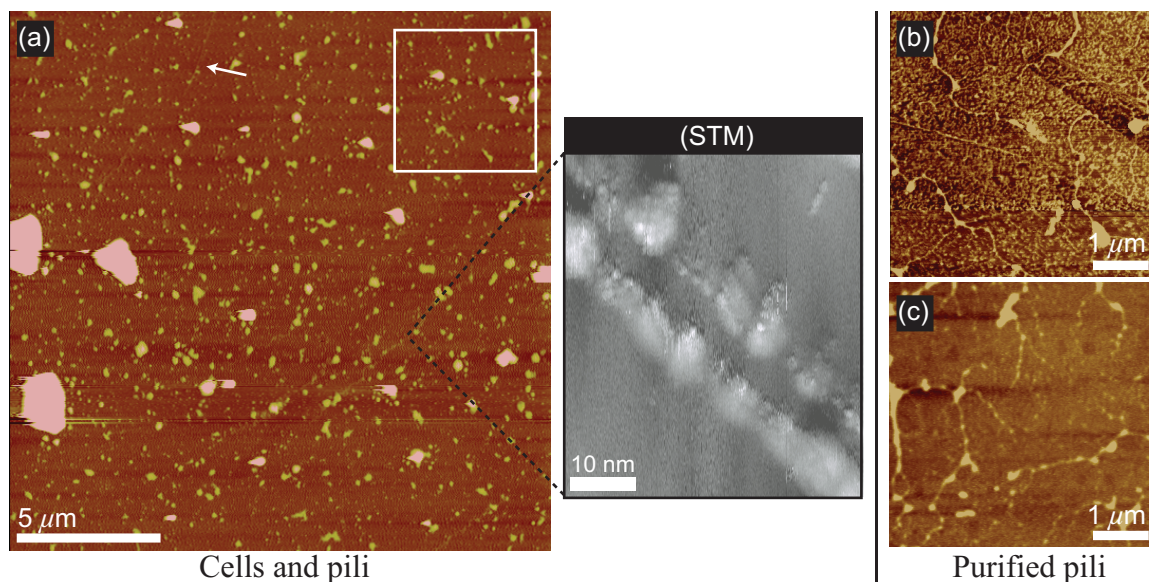


Figure 5.2: (a) Atomic force microscopy image of cells expressing pili deposited onto the surface of HOPG. The white box indicates the nominal maximum scan range of the STM. An increase in density of pili comes with increase in debris and cells. For reference, an STM topograph of a sample prepared in a similar way is also shown. A double tip, which often developed while scanning these dirty samples, complicates the interpretation ($V=900$ mV; $I=70$ pA). (b) AFM image of purified pili deposited at high concentration onto the surface of HOPG. With purified pili, we may exert much more control over the concentration and achieve sub-monolayer coverage for use in STM, as shown in (c). Both (b) and (c) are the same scan size as the maximum scan range of the STM.

the tip and surface in the presence of an electric field.

The use of samples of purified pili alleviated this problem. The purification process not only selected the conductive pili, but it removed insulating cells and debris present in the growth stage. For these samples, an increase in the pili concentration did not come with the consequence of a corresponding increase in the density of insulating cells hazardous to the tip. Figure 5.2 compares the two biological preparations after deposition onto HOPG. An STM topograph of a pilus, with a ghost image from tip degradation in this type of sample preparation is shown (Fig. 5.2(a)). Though tips were tested on cleaved HOPG before beginning the experiment, interactions with insulating debris frequently caused this

immediate tip degradation. The pili themselves in these preparations were quite disperse, as seen in the large AFM topograph. An increase in concentration resulted in a parallel increase in insulating cells and debris. In contrast, samples with purified pili preparations could be deposited at much higher concentrations (Fig. 5.2(b) and (c)). Because of the quality of purification, little or no other insulating debris was present in typical samples. The overall cleaner surface improved efficiency of STM study.

Substrate

The choice of substrate is a critical consideration when imaging biological molecules with STM. The surface should be electrically conductive because, after all, the source of signal in STM is the tunneling current. In addition, for optimal adsorbate definition during imaging, it should be flat. The surface should also be biocompatible so that the cells or other molecules may adsorb readily and not degrade quickly. Finally, the substrate material should be relatively inert to the surrounding atmosphere.

It is desirable, though not a strict requirement, that the conductivity in the substrate be metallic in nature. The current-voltage spectroscopy comes about from a convolution of the densities of states of the tip, adsorbate, and sample (Chapter 2). Such convolution of states is the reason metallic tips are preferred in most STM experiments to begin with. Substrates with metallic density of states over the energy range probed in the experiment simplify the interpretation of electronic information to extract the properties of the adsorbed molecules themselves.

In order to image with good contrast between the surface and pilus, and to obtain spectra for which the electron pathway was most clearly defined, we needed to deposit pili onto a substrate that was very flat over the region scanned. Quantitatively, I defined this as a

need for plane sizes at least an order of magnitude larger laterally than the adsorbed pilus. Vertically, the need was for corrugations an order of magnitude smaller than the 2–10 nm pilus size, which meant atomic or near atomic flatness. Thus, atomic planes that were hundreds of nanometers on a side were ideal. Because of limits in the dynamic z-range of the scanning piezo tube, it was desirable for step edges or other features on the surface to be no more than a few nanometers in height for good image definition. This allowed enough contrast in the image to resolve the pili, and for STM experiments, the local electronic density of states of the nanowire was presumed to be undisturbed as long as spectroscopy was performed sufficiently far away from defects.

Considering all of these substrate requirements, I studied in detail three surfaces for use as an STM substrate: Au(111), Si(100), and highly oriented pyrolytic graphite (HOPG). Of these, HOPG provided the most desirable combination of substrate conductivity, flatness, and biocompatibility. While working with the Au(111) surface, I observed evidence that pili were often not attached to the surface firmly enough to enable repeated STM imaging and spectroscopy after depositing samples of cells expressing pili. In limited data runs with purified pili deposited onto Au(111), I again failed to locate pili, which is consistent with the conclusion of poor attachment. During trials for another surface, Si(100), I consistently found that the tunneling current was not stable enough to image adsorbed pili. This is likely due to the 1 nm thick native oxide that forms in the ambient environment and covers the entire surface.

Though the surface of HOPG expresses filament-like artifacts that mimic biological molecules, an extensive study of these artifacts aided pilus identification (Chapter 4). Moreover, the implementation of samples of purified pili allowed greater control over concentra-

tion, thus providing a statistical pathway to discerning pili from artifacts. We obtained numerous pili on the surface for nearly every sample and were able to express enough control over the concentration and deposition to obtain sub-monolayer coverage.

5.2 Pilus Imaging

The high resolution real space imaging of STM provides an effective means to determine structure of conductive adsorbates at nanometer length scales. The high resolution aids not only in identification of pili, but also in the association of spectroscopic properties with spatial variation within the molecule. Tip shape and states may cause minor variations in the resulting image (Chapter 2.2), but molecular dimensions may be estimated from the topographs.

Figure 5.3 shows an STM topograph of a 200 nm segment of a long pilus from a purified sample preparation. A representative line cut across the diameter of this pilus is shown in Fig. 5.3(b) and indicates an apparent diameter of ~ 8 nm and an apparent height of ~ 1 nm. Typical measured diameters varied between 8–10 nm. The apparent heights varied depending on the tip position and sample voltage. The latter of these is a result of the voltage dependence of the density of states and will be discussed in greater detail in Section 5.3. Another line cut in Fig. 5.3(b) was taken along the pilus axis, indicating two periodic structures. First is a large pitch of ~ 14 nm, consistent with measured pitches of 12–14 nm on samples with purified pili. Helical quaternary structure has been observed for other type IV pili [3, 112, 113], attributed to the way in which the subunits assemble. The smaller periodic structure observed here, though convolved with the larger pitch, is also measured using a line profile along the pilus axis. The periodicity for this substructure is roughly 2–3 nm,

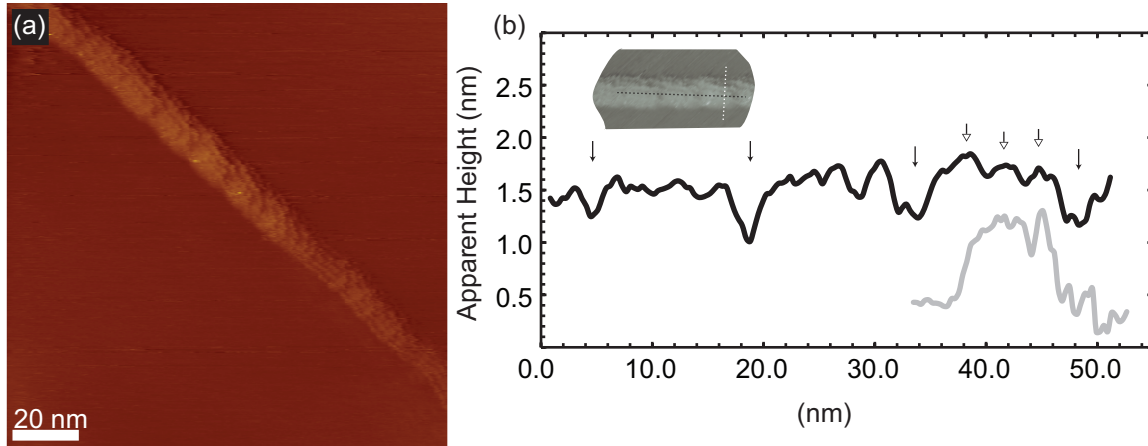


Figure 5.3: (a) STM topograph of a pilus from purified pili sample. (b) Axial (black) and transverse (grey) line profiles obtained for the same image at the locations marked in the inset. Offset on y-axis is arbitrary. Large pitch of ~ 14 nm measured over three periods denoted by filled arrows. Small pitch of ~ 3 nm measured over two periods (open arrows), consistent when measured at other locations (0.5 V, 110 pA).

consistent with the average measured periodicity of 2.5 ± 0.1 nm. Similar analysis gives an average peak width of 1.2 ± 0.1 nm.

5.2.1 Analysis of observed structure

To analyze the pilus dimensions observed by STM, we may also consider samples of cells expressing pili as in the STM topograph in Figure 5.2. Line profiles of diameter, height, large pitch, and small pitch gave approximate values of 6 nm, 1 nm, 7 nm, and 2.5 nm, respectively (profiles not shown). The finite tip radius in experiments studying both samples of cells expressing pili and purified pili led to geometric convolution of the tip and pilus in producing the images (Chapter 2.2.2). The most significant contributions were in lateral broadening, affecting the diameter, and vertical flattening, affecting the apparent height. By contrast, the line cuts that measured the pitch values were taken along the pilus axis and thus not subject to lateral broadening or vertical flattening.

As discussed in 2.2.2, analyses of STM images of carbon nanotubes deposited onto graphite indicated that broadening could occur by 50% to 300%, depending on actual carbon nanotube diameter. Diameters for the pili measured by STM range between 6–10 nm, and if we assume, at least to first approximation, similar broadening factors, then the pili would have a diameter of 3–7 nm, which is consistent with expected values of 2–5 nm. In contrast to broadening of the diameter, which was a result of geometric effects and variable tunneling gap width, the apparent pilus height would likely be flattened due to changes in tunneling gap width alone. This was measured for carbon nanotubes to be as much as 10–20% [44, 114]. Depending on the position of the tip and the applied voltage, typical apparent nanowire heights ranged from 0.8–1.2 nm. Applying the CNT estimate again suggests actual heights of 1.0–1.5 nm. One could speculate that additional flattening may have occurred from a reduction in moisture *ex situ*, explaining the still smaller diameter estimated by height versus estimation by width. A further comparison with measured AFM heights is useful because the imaging mechanism in tapping mode does not suffer from the flattening effect of the STM tunneling gap. Typical heights measured in AFM characterizations were 1–2 nm, consistent with this assumption (Appendix B). Moreover, samples that do not conduct as well as carbon nanotubes may suffer from this flattening effect in STM to a greater degree [44]. These reasons may explain why the diameter is smaller when measured via height compared with width.

In general, STM measurements were consistent with expectations for pilus dimensions, and while an exact molecular model of the *G. sulfurreducens* pilus does not exist, the observed structure has features in common with models of other type IV pili [3, 112] and cryogenic SEM images of *N. gonorrhoeae* type IV pili [113]. The smaller pitch of ~ 2.5 nm is perhaps

consistent with the expectation of “hot spots” of conductivity discussed in Chapter 3. This will be explored more in Section 5.6.

5.3 Voltage-dependent Imaging

Given that the tunneling current magnitude depends on the integrated sample DOS between the applied voltage and zero (Eqn. 2.9), the STM topograph contains spatially-resolved information about the density of states. The resulting image is a convolution of the morphological structure and the electronic states probed (2.1.2). We used this fact to perform a type of electronic spectroscopy by imaging the sample at different bias voltages. At low voltages ($\lesssim 1$ V), the states probed are those in the energy range corresponding to the voltages between the set bias voltage and zero volts. An image at 0.5 V, for example, resulted from an integral of the states between 0 and 0.5 eV.

When operating in constant current mode, the image is actually a topograph of the value of the feedback voltage that is applied to the scanning piezo tube in order to keep the tunneling current constant, thereby producing an image with information about both the morphological structure and the density of states. If a local electronic state has a threshold turn on voltage, then as the applied voltage is increased past this threshold, the tip detects an increase in tunneling current. The feedback voltage responds accordingly, pulling the tip out, which consequently increases the apparent height. If the characteristic threshold of this local state is not uniform with the surrounding structure, the difference in contrast makes it appear brighter in relation to its surroundings. This is an illustrative example of how changes in electronic states can alter the topographic image even though the morphological structure of the object has remained the same.

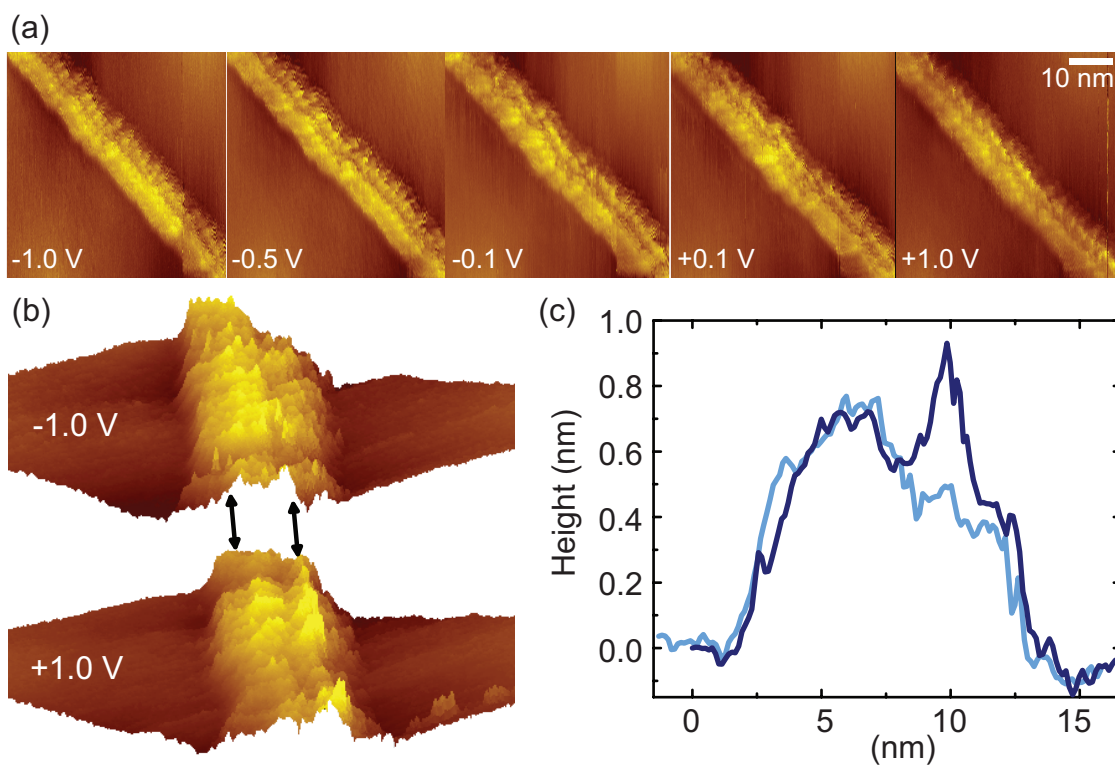


Figure 5.4: Voltage-dependent imaging of the pilus nanowire shown in Fig. 5.3. The apparent height is proportional to the integral of density of states (Chapter 2.1.2). (a) Topographs of the same pilus section obtained at different sample voltages. (b) Three-dimensional rendering of the topographs at +1.0 V and -1.0 V to highlight differences in apparent height on the left edge versus the right edge. (c). Representative line profiles taken at the same location for +1.0 V (dark blue) and -1.0 V (light blue).

Acquisition of multiple topographs at different voltages allowed visual inspection of the spatial dependence of electronic states at different energies. Figure 5.4(a) shows a series of images of the same pilus section at different voltages. The character of the ~ 2.5 nm pitch “hot spots” appeared to change slightly, but the most dramatic differences occurred upon comparison of the apparent heights of the left and right edges for +1.0 V versus -1.0 V. Three dimensional renderings of the images from these voltages are shown in Figure 5.4(b). At -1.0 V sample voltage, the pilus is brighter on its left edge than right edge, indicating greater apparent height. By contrast, at +1.0 V sample voltage, the pilus is brighter on its right side. This apparent difference is not due to a change in the physical height above the surface, but rather indicates an asymmetry in the spatial dependence of the electronic structure at opposing polarities. The asymmetry essentially suggests easier current flow out of the pilus on its left edge and into the pilus on its right edge.

Figure 5.5 shows the development of the transition between these two regimes in 100 mV increments using STM data obtained on a sample of cells expressing pili first shown in Fig. 5.2. The apparent heights do not portray the asymmetry for voltages near zero, but the crossover into asymmetric behavior—for both positive and negative polarity—happens at 0.4–0.6 V. We will return to this in the discussion of Section 5.6.

5.4 Point Spectroscopy

We further investigated the variation in energy states at different voltages using point spectroscopy, which displays information on the density of states in a two-dimensional curve. In this case, the tip was stopped at several different locations above the pilus, the voltage swept, and either the current, I , was recorded directly or the differential conductance, dI/dV , was

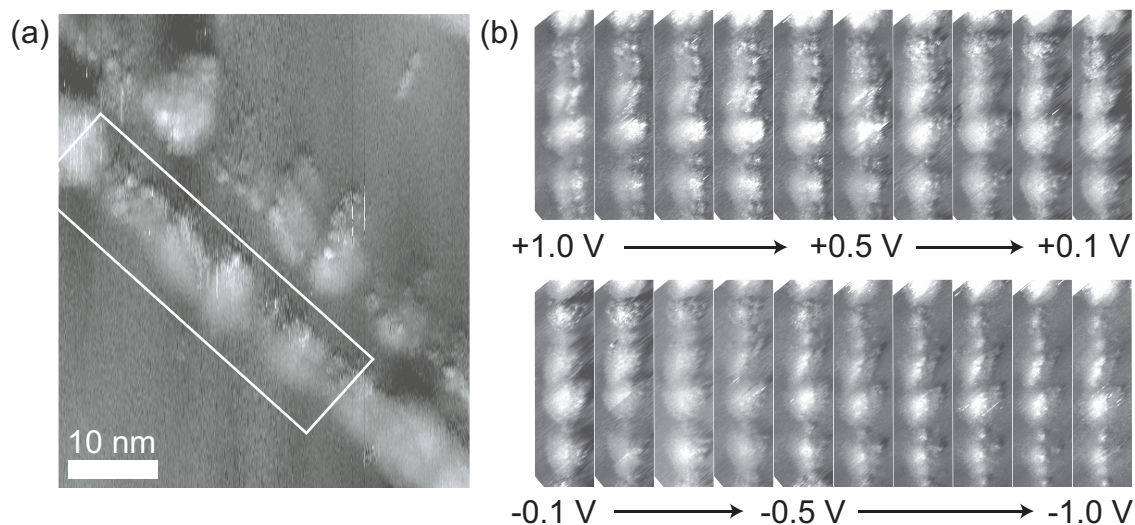


Figure 5.5: Voltage dependent imaging in 100 mV increments for the pilus from Fig. 5.2. (a) The white box denotes the location at which all images in (b) were cropped ($V=900$ mV; $I=70$ pA). (b) Topography development with voltage changing in 100 mV increments between +1.0 V and -1.0 V. Images near +1.0 V have a larger apparent height on the right edge while images near -1.0 V have a larger apparent height on the left edge, qualitatively consistent with the observation for purified pili in Fig. 5.4. Here, a large pitch of 6–8 nm is constant with voltage and a small pitch of 2–2.5 nm shifts from right to left with voltage. ($|I|=70$ pA)

obtained with a lock-in amplifier (See Chapter 2.1.3). dI/dV is proportional to the local density of states, albeit limited by thermal smearing (Chapter 2.1.3). As $I-V$ is the integral of the differential conductance, it too is a valuable way to display spectroscopic information about the density of states.

Curves taken at positions spanning the diameter show varying asymmetry. Figure 5.6 shows the basic spatial dependence of both $I-V$ and dI/dV spectroscopy curves. The $I-V$ curves demonstrate that the current signal was higher for negative voltage on the left edge, while higher for positive voltage on the right edge. In the center of the pilus, the $I-V$ curve was symmetric. The dI/dV curves display the same information in a slightly different form. The right edge has a greater measure of density of states for large positive sample voltages, while the left edge has greater measure for negative voltages. For smaller voltages, such as ± 0.3 V, this asymmetry in dI/dV was reversed. Above the center of the pilus were symmetric dI/dV curves with characteristics of the substructure seen in the curves on the left and right edges. All three curves show a gap-like behavior near the Fermi level with widths of $\lesssim 1$ V and sub-gap states. Any spatial dependence of the width of the gap-like feature could not be determined, as the variations of the width in different curves were on the order of the margin of error from thermal smearing at room temperature, ~ 100 meV. Finally, interesting peaks or plateau-like structures occur near the edges of the gap, between 250–750 mV, denoted by arrows.

The overall evolution of the asymmetry as the tip moved along the diameter of the pilus is plotted in Figure 5.7. Fig. 5.7(a) shows a series of fourteen dI/dV curves obtained for different points spanning the diameter of the pilus. Points off the pilus express spectra that are characteristic of the graphite substrate. Points on the right edge of the pilus are

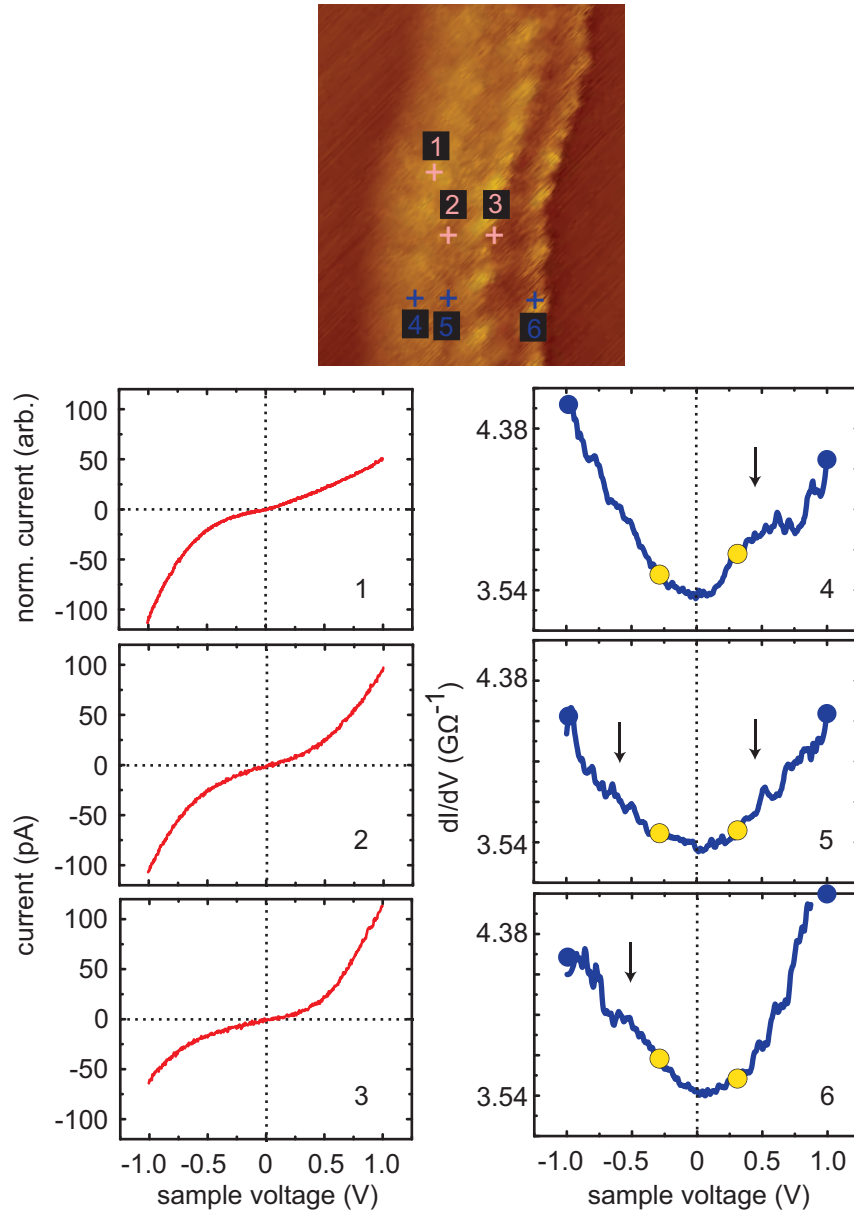


Figure 5.6: Position dependent tunneling spectra for a purified pilus. Red: I - V spectroscopy curves at left edge, center, and right edge locations denoted in the topograph. Each is an average of 100 I - V curves obtained in sequence. Blue: dI/dV spectroscopy curves at the left edge, center, and right edge locations denoted in the topograph. Each is an average of 20 curves obtained with a lock-in amplifier, followed by 19-point Savitzky-Golay smoothing. The blue and yellow circles are added to the dI/dV curves at ± 1.0 V and ± 0.3 V, respectively, as visual aids for observing the asymmetries at those voltages. (Topograph: $V=1.0$ V; $I=150$ pA)

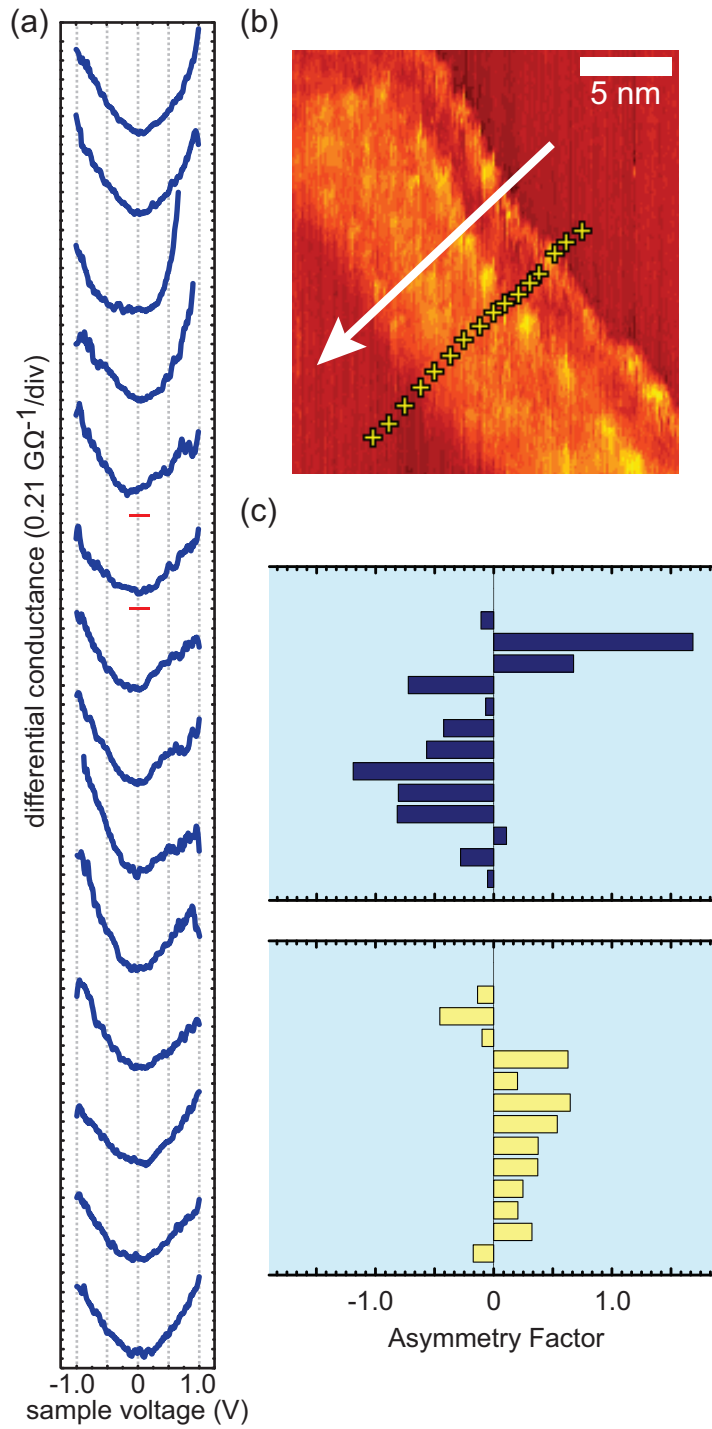


Figure 5.7: (a) dI/dV tunneling spectroscopy for fourteen curves spanning the diameter of the same pilus under the same conditions as in Fig. 5.6; locations marked in (b). Right edge to left edge is top to bottom. A short red line denotes an omitted curve due to anomalous noise, inconsistent among the 20 averaged curves. Major tick marks in (a) are each $0.21 \text{ G}\Omega^{-1}$. (c) Asymmetry factors for each of the fourteen dI/dV curves in (a). (Topograph: $V=1.0 \text{ V}$; $I=150 \text{ pA}$)

asymmetric but become more symmetric as the tip moves toward the center. Moving on from the center to the left edge of the pilus, the curves become asymmetric again but have the opposite asymmetry to the right edge. To quantify this, we defined the asymmetry factor, which is the natural logarithm of the ratio of dI/dV value at positive polarity to the value at negative polarity:

$$AsymmetryFactor(|V_0|) = \ln \left(\frac{\left. \frac{dI}{dV} \right|_{V=-V_0}}{\left. \frac{dI}{dV} \right|_{V=+V_0}} \right) \quad (5.1)$$

Curves with opposite asymmetry have asymmetry factors with opposite signs, and the magnitude is a measure of the magnitude of the asymmetry. Plotted in Figure 5.7(c) are fourteen asymmetry factors, calculated from the curves in (a), moving in order along the diameter of the pilus from right edge to left edge. I have calculated asymmetry factors for both ± 1.0 V and ± 0.3 V. Examples of spectrum locations at which they were calculated are denoted by the blue and yellow circles in Fig. 5.6. When the two bar graphs are compared side by side, it is clear that the asymmetry at higher voltage is opposite the asymmetry at lower voltage, closer to the Fermi level. This is true for all positions on the pilus. At both high and low voltage, the asymmetry flips sign as the tip moves from the right side to the left side. For high voltage, this means the asymmetry flips from negative to positive, and for low voltage, this means the asymmetry flips from positive to negative.

5.5 PAK Pilus Negative Control

As discussed previously in chapter 3, the pili of *Geobacter* species are protein filaments classified as type IV pili and are assembled from pilin subunits. The pili of *Pseudomonas*

aeruginosa, like *Geobacter*, are also type IV. The polymerization of the PAK pilin subunit, composed of an α -helix tail and large globular head group, also assembles helically [3, 115]. However, unlike *Geobacter sulfurreducens* pili, they are not electrically conductive. The *P. aeruginosa* bacteria use these pili for twitching motility [116] and attachment to cells of hosts for infection [117, 118]. Although the structure of *P. aeruginosa* pili protein filaments is similar to that of *Geobacter*, they do not have electronic states participating in electron transfer [1]. Thus, they provide a negative control for *Geobacter* pilus electronic properties.

Purification of *Pseudomonas aeruginosa* K strain (PAK) pili, performed in the Reguera lab, produced filaments that had lengths of hundreds of nanometers and diameters comparable to those of *Geobacter* when examined with AFM (Fig. 5.2(a)). Often, this apparent diameter for both species' pili was 30–40 nm in AFM, likely due to broadening from tip curvature (Chapter 2.2.2). Height measurements in AFM were more accurate, and we measured heights of 2–3 nm, somewhat smaller than the 5 nm diameter measured from X-ray diffraction and EM data of single PAK pili [3, 119]

In contrast, PAK pilus imaging was much more difficult with STM, where the imaging mechanism required a tunneling current. The behavior was that of a surface covered with insulating debris. Because of the unstable tunneling current, images were noisy, and identification of pili was not possible without increasing the applied voltage much higher than required when imaging purified *G. sulfurreducens* pili. Figure 5.8(b) is one such image. The voltage was increased to 3 V, much higher than is biologically relevant for electron transfer processes, and much higher than used for *G. sulfurreducens* pili, which ranged between ± 1 V and gave images stable enough to resolve LDOS variations (Section 5.3). While a PAK pilus is discernable in Figure 5.8, its poor definition is the result of an unstable tunneling signal

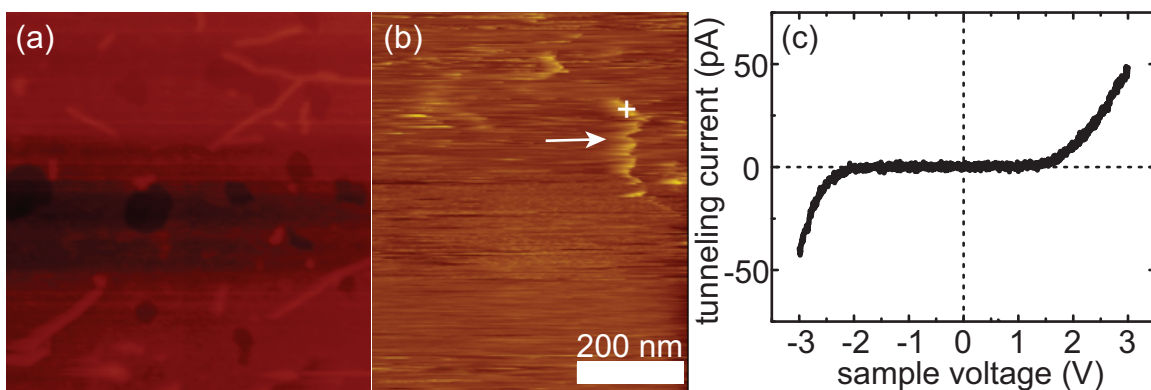


Figure 5.8: Purified PAK pilus control sample. (a) AFM characterization of purified PAK pili. (b) STM topograph of purified PAK pili, indicative of unstable tunneling current and insulating behavior ($V=3.0$ V; $I=50$ pA). (c) I - V tunneling spectrum taken at the point denoted in (b). Voltages had to be high to obtain appreciable signal. The curve has a flat (insulating) region that extends well outside the bounds where significant tunneling current was obtained for *G. sulfurreducens* pili (Fig. 5.6), and well outside the bounds of biologically relevant electron transfer energies.

between the tip and surface, described as follows.

As the tip scans along the conducting HOPG substrate, it enjoys a stable tunneling current. As it comes upon an insulating object, the feedback loop detects this as a decrease in the tunneling current. In order to compensate, the feedback pushes the tip closer to the surface until it detects a current spike greater than or equal to the set point current (Chapter 2.3.3). For an insulating molecule, the error signal will not be monotonic across the diameter. Thus, the pilus is imaged unstably, although a human observer of the topography can distinguish it from the surrounding graphite. In addition to imaging the pilus unstably, the hard contact of the STM tip with the pilus molecule can damage the delicate, sharp active region of the tip. The tip can be left with loose atoms or pieces of debris from the pilus that are not as rigid as the solid metal usually is. This is why much of the image (Fig 5.8(b)) after this tip contact continued to look unstable.

Using tunneling spectroscopy to take a more careful look at the electronic structure of the PAK pilus corroborated this inference. Point spectroscopy is less sensitive to a damaged tip cone, although a flaky tip may cause anomalous I - V curves if mobile atoms or contamination cause the effective tip-sample separation to fluctuate. Figure 5.8(c) shows a PAK I - V spectrum obtained between +3 V and -3 V. These high bias sweep limits were necessary to get appreciable signal. We may use tunneling I - V to infer information about the density of states, much like its derivative, dI/dV . When we compare this PAK I - V curve with a *G. sulfurreducens* I - V curve (Fig. 5.6) near the Fermi level, in the region of the spectrum where we studied *G. sulfurreducens* electronic structure, the PAK pilus I - V curve is quite flat, suggesting a virtually infinite resistance. The signal to noise ratio for PAK pilus I - V curves was quite low, as there was little tunneling current detected.

Recall from Chapter 2.1.3 that because of the arbitrary tip-sample distance when performing tunneling spectroscopy, spectroscopic curves often must be normalized in order to directly compare them. Because of the evidently poor conductance of the PAK pilus, the gap voltage while scanning PAK samples was necessarily much higher than that for *Geobacter* samples. In the voltage range studied for *Geobacter*, PAK was quite insulating, so a comparison of normalized curves would not be easy to interpret, if meaningful at all. Thus, the I - V comparison of PAK with *Geobacter* should not be quantitative but rather qualitative, based on the information contained therein.

The I - V spectroscopy and the difficulty in stably imaging the PAK pili were consistent with our expectation that PAK pili, having no known evidence of or need for participation in electron transfer processes, should be nominally insulating and should not image easily or give the interesting electronic signature seen for *G. sulfurreducens* pili. Thus, there is

something significant about the structure of the *Geobacter* pili that leads to the biologically relevant conductivity. The PAK pilus, a protein filament of similar size and structure, did not display the same electronic behavior when observed with STM. We can rule out artifacts of the technique that perhaps could have contributed to stable imaging for *G. sulfurreducens* pili, such as stable tunneling through the pilus protein. The STM technique has given us information unique to the electronic structure of the *Geobacter sulfurreducens* pilus.

5.6 Discussion

A very important result from this STM work is the affirmation that electron transfer occurs along the pilus protein matrix itself, rather than metalloproteins (See Chapter 3), as evidenced by the stable imaging and high spectroscopy signal. Though coherent signal had been observed previously with a CP-AFM study of mechanically sheared pili [1], metalloproteins, and other cell debris were not systematically eliminated. These are present in cells further up the ET chain before the electron reaches the pili. However, in the STM examination of samples of purified pili, the matrix of the protein was isolated from any contamination of this kind. Moreover, spectral features in $I-V$ and dI/dV of these isolated pili were indicative of good conduction rather than insulation or tunneling across the pilus as the tunneling barrier [24, 120]. Asymmetric spectroscopy curves with the basic peaks and gap-like features shown in the preceding sections were obtained with varying degrees of quality on roughly five pili from purified preparations. The spatial dependence of this structure, however, was observed twice on pili from purified samples and once on a pilus from a preparation with cells expressing pili. Further examination of the electronic structure of this protein conduction is discussed below.

Topographic structures

Recall from Chapter 3 that a hypothetical explanation of the charge transport in the pilus nanowires constructed a series of donor and acceptor sites along which an electron may continuously travel. For an electronic probe of the density of states, these donor and acceptor sites may be manifest as imaged “hot spots” of conductivity. The periodic structure discussed in Section 5.2 had a pitch that ranged 2–3 nm and an average pitch of ~ 2.5 nm (Figs. 5.4 and 5.5), consistent with the known distant limit of single superexchange tunneling events and approaching that of hopping (Chapter 3.4.3). This may invite the assumption of a varying inter-hot-spot distance range of 2–3 nm, but it is unclear from the data whether this was a real fluctuation or the result of the tip interaction or convolution with the larger pitch. Future STM studies may examine this possibility, but it should be noted that this distance range is consistent with the distance limits for superexchange tunneling and multistep hopping.

Comparison of the larger pitch with the helical quaternary structure of other type IV pili with known protein structure is complicated by the inconsistency of its STM measurement. The measured pitch was either 7–8 nm or 12–14 nm depending on which pilus was measured. Because the latter value is double the former, one could speculate that for structural or electronic reasons the STM was unable to resolve every period every time. The PAK structural model, however, gives a pitch of 4.1 nm, defined by the size of the subunit’s $\alpha\beta$ -head group [113]. Of course, because the PAK pilus has a much different electronic structure than the *G. sulfurreducens* pilus (that is, it is insulating), an STM image of its pitch does not exist for comparison. Structural and electronic models of the *G. sulfurreducens* pilus nanowire would be useful for comparison with these data.

Electronic structures

The tunneling spectra shown in Section 5.4 express an asymmetric character, and are gap-like near the Fermi level with sub-gap states. The peaks in the spectra occur at 0.4–0.6 V (Fig. 5.6), which is also the voltage onset of the increased brightness in the 2.5 nm periodic structure in the voltage-dependent imaging of the pili (Fig. 5.5). Biologically relevant reduction potentials for cytochromes in anaerobic microbes, which are also tuned to Fe(III) reduction, are in the range of ± 0.4 V [20, 121]. While the features at these potentials were not closely scrutinized in data acquisition, future STM work may focus on precise measurement and character of these peaks for comparison with reduction potentials and modeling of *G. sulfurreducens* pili.

The broader spatial dependence of the electronic structure presents a clearer picture. We observed a spatial dependence of the nature of the asymmetry in the dI/dV spectra (Section 5.4) that was also visualized by voltage-dependent imaging (Section 5.3). That is, the location on the pilus where dI/dV exhibited enhanced states at +1 V compared with -1 V (the right edge) was also brighter in topographs obtained at +1 V. Similarly, dI/dV spectra on the left edge were enhanced at -1 V and images at that voltage were correspondingly brighter on the left edge. Assuming no significant difference in the tunneling matrix element, brighter contrast represents larger apparent height and thus higher integrated density of states.

The spatial dependence of this asymmetry is key. Rectifying behavior has been observed previously in tunneling spectra of atomic adsorbates [122] and several biological adsorbates, including those in References [24, 123], which were artifactual. Depending on the situation, the effect may arise due to band bending at the substrate-adsorbate interface or an asymmet-

ric voltage drop at the tip-adsorbate versus adsorbate-substrate tunneling gap. In our STM data, the fact that the sign and nature of the asymmetry develop spatially depending on tip position suggests it is intrinsic to the nanowire electronic structure itself. Real rectifying behavior in organic molecules is not unprecedented [124, 125, 126, 127, 128], and in the case of *G. sulfurreducens* pilus nanowires, it may be biologically relevant.

Asymmetry of current flow between the sample and the tip may be inferred from the dI/dV spectra and visualized by the I - V spectra (Fig. 5.6). When the STM tip is above the left edge, it probes electrons from the current coming out of the sample, and when it is above the right edge, it acts as a source for electrons going back into the pilus (see Eqn. 2.7). To speculate on how this may be extrapolated to the nature of the long-range transport in the pilus nanowires, we may again consider the type IV structural model [113]. We know that type IV pili have helical symmetry, so the reversal in the sign of the rectifying behavior may indicate current flow in one direction circumferentially and thus axially as well. While this is speculative, the biological relevance of this is the fact that the cell may like to keep electrons moving away, toward the external electron acceptor (Chapter 3).

The stability and quality of the STM data, along with existing biological data, suggest that electron transfer occurs along the protein matrix. While these STM data give evidence that the pilus nanowires may be rectifying, we would need a direct observation of such behavior via a transport measurement to clarify this. Moreover, electron transfer in proteins across distances farther than 10 nm would itself be novel behavior. This so-called long distance electron transfer is the object of study in the transport experiment described in the following chapter.

Chapter 6

CP-AFM study of pilus long distance electron transfer

Recall from Chapters 1 and 3 that biological studies of the *Geobacter sulfurreducens* respiratory system have indicated that the organism's pilus nanowires transport electrons across longer distances than previously observed in biological systems. The fact that cell viability is uniform across 40–50 μm thick *G. sulfurreducens* biofilms grown on fuel cell electrodes suggests that the transport for single nanowires could be on the order of a micron or more [14]. The authors of that study also state that individual pili as long as 20 μm have been observed. Recent experiments in marine sediments observed redox reactions across distances of 12 mm, between oxidized and reduced materials, at rates much faster than achievable by diffusion. This suggests that direct electrical contact exists, perhaps via a network of conductive nanowires [129].

Fundamental limits for single electron transfer tunneling and hopping events are 20 Å and 35 Å, respectively (Chapter 3). Recent experiments have even observed electron trans-

port across distances in excess of 120 Å in self-assembled monolayers of synthetic α -helical peptides [17]. The ability for charge to move this distance was attributed to multistep hopping. While the study of *Geobacter* pili thus far has suggested that transport may occur over much longer distances than these, the evidence is indirect. Additionally, STM (Chapter 5) and other experiments have suggested that the conduction takes place along the protein matrix; an observation of such long distance protein transport would further push the need to consider a novel transport mechanism for *G. sulfurreducens* pilus nanowires.

To this end, we developed a method to measure long distance conductivity of a pilus nanowire bridging a surface electrode with a conductive AFM tip (Figure 6.1). We used photolithography to deposit a single microelectrode with 5–10 μm gaps opening to an insulating substrate. While operating the CP-AFM in topographic mode, we searched the insulating surface for pilus nanowires lying across the edge of a gap, resting opposite ends on the gold electrode and the substrate. We then placed the tip into an end of the nanowire opposite the electrode to measure current with the conductive probe.

The samples we dealt with were heterogeneous mixtures having aggregates of multiple pili interspersed with individual pili (see for example, Fig. 5.2(b) and (c)). However, the method we developed gave us a statistical advantage over more straightforward transport measurement methods like fixed two-point and four-point fabricated probes. The dynamic AFM probe was able to search for individual isolated nanowires, in contrast to the more traditional methods, which would have relied on single unaggregated nanowires to land across each of the stationary probes. El-Naggar and co-workers developed a similar experiment in parallel to our own development, but they studied nanowires expressed by *Shewanella oneidensis* [130], where the conductivity takes place among cytochromes [73], rather than

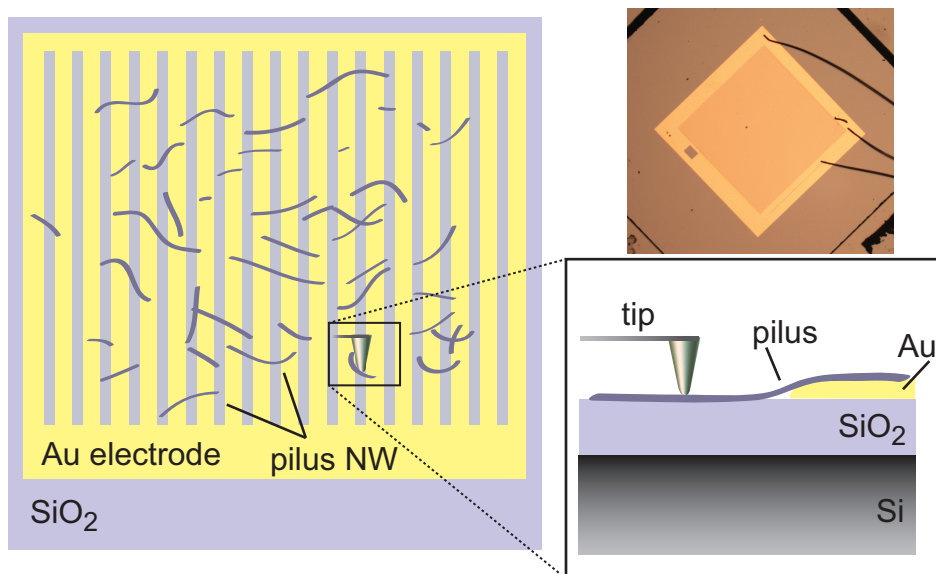


Figure 6.1: Schematic of the experiment. Purified pili suspended in water are deposited onto a surface electrode. For electronic measurement, the pilus bridges the electrode to a conductive AFM tip. *Upper right:* Photograph of one of the electrode geometries we use.

the protein matrix as with *G. sulfurreducens* pili. While we shall see in this chapter that at this time, we have obtained preliminary data using our system, and that long distance conductivity has been observed in *Geobacter* nanowires, the experiments discussed here are ongoing.

6.1 Materials & Methods

We used standard photolithography techniques to deposit metallic electrodes onto insulating substrates. Photoresist (Shipley S1813) was spin-coated onto silicon $\langle 100 \rangle$ wafers having either native (~ 1 nm) or thermally grown (300 nm) oxide surface. After the photoresist development, we evaporated 5 nm of titanium followed by 25 nm of gold onto the exposed wafer surface. Purified pili suspended in doubly distilled water (ddH₂O) were then deposited onto the electrodes, left to adsorb for 10–25 minutes, and wicked dry with absorbent paper.

Wafers having only the native oxide were B-doped (p type) and had bulk resistivity of 1–5 Ω -cm. Electrical contact to the metal electrode was obtained by attaching a gold wire with conductive paint.

Topographic imaging to evaluate deposition quality was performed with a DI-3100 AFM, as described in Chapter 5.1. CP-AFM was performed on another device (Asylum) with Pt:Ir-coated silicon cantilevers having nominal spring constants of 42 N/m. While in imaging mode (tapping), we identified pilus nanowires lying across the electrode edge, and then obtained I - V curves after placing the tip on a point of the pilus lying on the SiO_2 opposite the electrode. For control, we obtained I - V curves on the surrounding substrate and the gold electrode to check for insulating and metallic behavior, respectively. We also used STM to measure the surface band gap of the silicon with the native oxide.

6.2 Preliminary Results

6.2.1 Native oxide substrate

We first investigated deposition of and transport in pili on the native oxide of silicon. In ambient atmospheric conditions, the presence of water and oxygen promote the growth of a ~ 1 nm thick layer of SiO_2 on the surface of Si [131], termed the native oxide. Although we operated at low voltages within the band gap, the insulating barrier helped impede electronic conductivity through the substrate at the low voltages applied. The standard value of the indirect band gap of Si is 1.1 eV, and the surface band gap measured with STM across the native oxide was ~ 3 eV (Fig. 6.2).

Figure 6.3 shows I - V curves obtained from one of these samples. The curve acquired

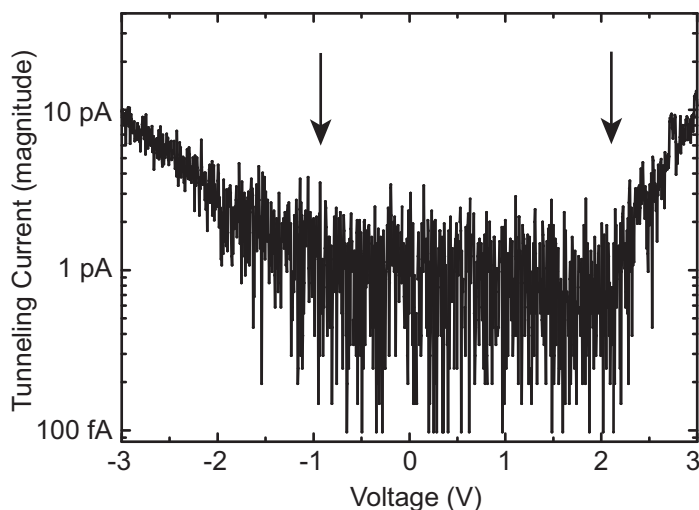


Figure 6.2: Representative STM I - V spectroscopy taken at a point above a clean silicon wafer like that used in the electrode of Fig. 6.3, plotted on a log scale. Arrows mark the edges of the band gap, well outside the region probed in Fig. 6.3.

with the tip placed above the end of a nanowire, roughly 200 nm away, shows significant conductivity compared to that for the surrounding silicon substrate. Voltages were ramped cyclically, so the two curves for each point were acquired: one while the voltage increased and one while the voltage decreased. An average low-voltage resistance of $40\text{ M}\Omega$ was calculated from the slopes of the I - V curves in the linear region near the Fermi level. Outside this region, the resistance at negative voltage was roughly $15\text{ M}\Omega$. Control I - V curves taken on the Si substrate show insulating behavior in this voltage range, which is inside the band gap. Finite current near $+500\text{ mV}$ may indicate Schottky behavior where the electrode contacts the surface. STM electronic spectroscopy obtained on clean electrodes fabricated in the same manner indicated a band gap at the surface of $\sim 3\text{ eV}$ (Fig. 6.2), which is consistent with silicon's I - V behavior in Figure 6.3. Finally, I - V curves obtained with the tip placed above the gold electrode show resistance several orders of magnitude less, as the amplifier saturates almost immediately at finite voltage.

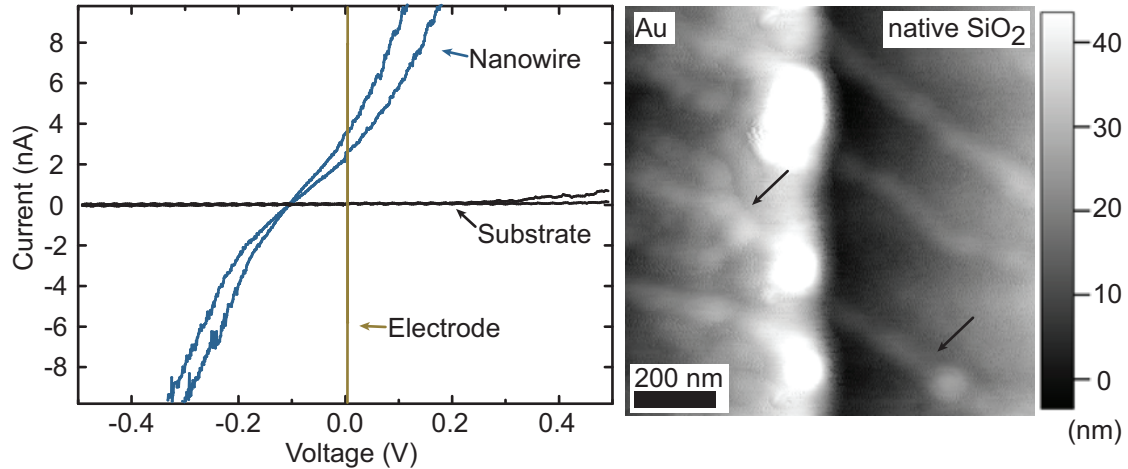


Figure 6.3: I - V curves obtained with CP-AFM at points from the AFM topograph at right. The nanowire and substrate curves were taken with the tip placed roughly 200 nm away from the electrode. We have not speculated here on the origin of the finite current at zero voltage. While the electrode curve appears vertical and overlaps the current-axis, it has finite slope consistent with gold conductivity.

The results here offer convincing preliminary evidence of long range conductivity, but we should be careful about generalizing to electronic behavior of the pilus. Unfortunately, this short data run was limited by time constraints, as it was obtained on others' equipment. We obtained just one conductance curve for the nanowire and studied just one sample deposited onto this substrate. Though the STM and CP-AFM control measurements of the band gap on the surface demonstrate no significant tunneling across the 1 nm native oxide, we may choose a different surface that has less access to surface states. In the next section, I will discuss work with a substrate having a thicker oxide.

6.2.2 Thermal oxide substrate

Because the effects of surface electronic states on substrates having only the 1 nm thick native oxide are unknown, we sought to repeat the measurement of Section 6.2.1 on a silicon

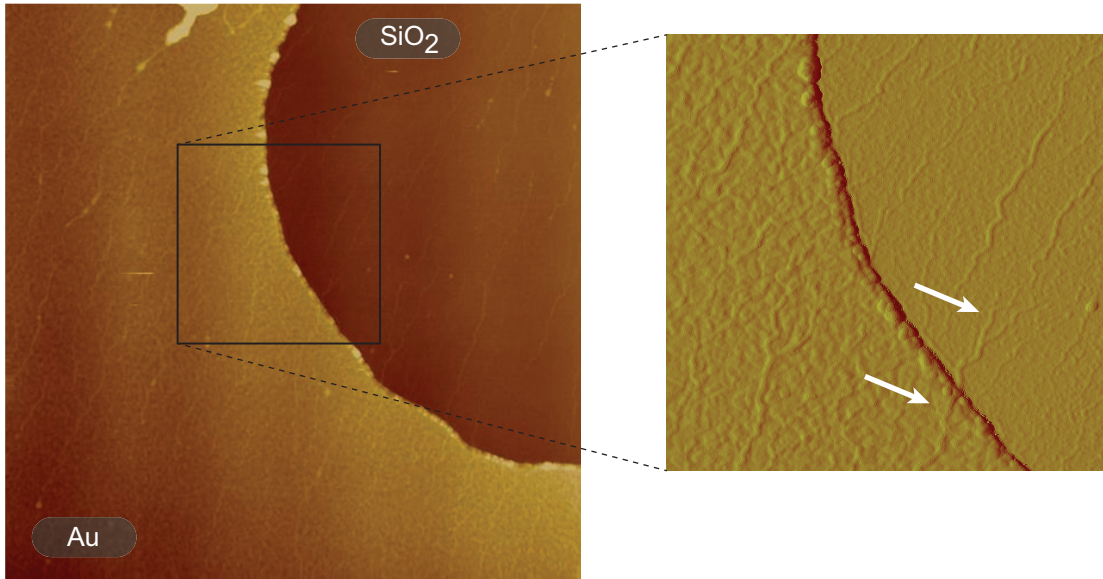


Figure 6.4: AFM characterization of a deposition onto 300 nm SiO₂. The larger, 7 μm x 7 μm topograph shows widespread coverage of pili, and the inset shows pili lying across the electrode edge. The inset is an amplitude signal topograph taken following the larger image.

wafer with a thicker, thermally grown oxide from a dry growth process [132]. The oxide thickness of 300 nm is much greater than the distance across which significant tunneling current may flow, so the electronic states at the Si surface are inaccessible to the CP-AFM probe. In addition, we are not limited to voltages within the Si band gap.

Though successful electronic measurements have yet to be performed on samples prepared in this way, we have begun work to test the deposition onto this surface. Figure 6.4 shows a successful deposition of a sample of purified pili. The surface had a heterogeneous arrangement of aggregates and individual pili. Current work in our lab is focusing on optimizing the protocol so that we may have reproducible control over the deposition quality. Electronic measurements like those obtained on the native oxide will follow thereafter.

6.3 Discussion and Future Directions

The observation of long-range (~ 200 nm) electron transport discussed in Section 6.2.1 is quite promising but needs to be reproduced. An upper limit of resistance was calculated from the data of Section 6.2.1. As our scheme is essentially a two-probe measurement, contact resistances between the nanowire and the tip or surface electrode will increase the measured resistance. Control over the pressure exerted by the tip on the nanowire may reduce the former source of contact resistance. During experiments of conductivity of pili deposited onto the thick thermal oxide, we intend to quantify the contribution of these contact resistances by measuring the resistances of the same nanowire at different distances from the electrode. In this experiment, a plot of resistance versus distance should have a y-intercept equal to the total contact resistance. This will in effect be a scanning probe version of a transmission line measurement. The existing data quantified the average low-voltage upper limit of resistance at just one distance (~ 200 nm) to be ~ 40 M Ω . In other words, the data imply an upper bound on the resistance per unit length of 200 M $\Omega/\mu\text{m}$. We estimate the resistivity from this to be 0.1 – 0.4 $\Omega\text{-cm}$ depending on whether we use the area implied by a ~ 5 nm cylindrical nanowire diameter or the area estimated from flattened nanowires (Appendix B). This is roughly the same resistivity as the basal plane of graphite. For comparison, measurements by El-Naggar *et al.* for *Shewanella oneidensis* nanowires also subtracted the contact resistance in the manner described above, resulting in a resistivity of 1 $\Omega\text{-cm}$, comparable to that of moderately doped silicon nanowires [130].

In the future, we would like to further explore the possibility for nanowire rectifying behavior, for which we discussed evidence in Chapter 5. Though the curve in Figure 6.3 does show some asymmetry, an experiment designed to test this specific question would be

preferable. In future transport experiments of the kind discussed in this chapter, we may replace the single surface electrode with two interdigitated electrodes—Electrodes A and B. I - V curves may then be obtained with Electrode A biased and Electrode B grounded. Rectifying character should be reversed if we then conversely ground Electrode A and bias Electrode B. This eliminates the possibility that differences in contact resistance between the tip and electrode cause rectifying behavior not intrinsic to the nanowire itself [24, 133].

It is important to keep in mind that the long-range electron transport in *Geobacter sulfurreducens* takes place along the protein matrix itself (Chapters 3 and 5), while transport in *Shewanella oneidensis* nanowires takes place along cytochromes that align themselves along the pili [73]. Electron transport along the protein matrix at such long distances would require a novel biological electron transport mechanism. Future work with this experimental setup will investigate expectations that this novel transport happens at distances even longer than 200 nm.

Chapter 7

Conclusions

The electron transport chain in *Geobacter sulfurreducens* employs pilus nanowires to attach to external electron acceptors. Using scanning probes, we have made progress in understanding the mechanism of electron transport in these pili. In concert with previous biological experiments, we have shown that electrons do not travel along metalloproteins, as they do in many other biological ET processes, including long distance electron transport in other microbial nanowires [74, 130]. Rather, electrons move along the protein matrix itself. Evidence for this included the stable and significant tunneling current signal and energy spectra from our scanning tunneling microscopy experiments performed on purified pili lacking metal atoms. Additionally, the results of the STM experiments gave information about the local electronic density of states at different positions on the pilus. Although we were primarily interested in electronic states contributing to long distance electron transport, for these measurements, the charge traveled transversely across the diameter of the nanowire, a distance on the order of just a few nanometers. In contrast, our transport experiment measuring pilus conduction to a surface electrode, with CP-AFM as a dynamic second electrode, detected

electron transport length-wise, over a distance on the order of hundreds of nanometers. As our lab further develops this technique, we postulate that it will have the ability to detect transport over distances perhaps as long as a micron, a distance scale suggested by biological reports [14, 129].

Because fundamental distances for well understood electron transfer processes purely in the protein matrix are limited to ~ 4 nm (Chapter 3), and recently reported observations of protein matrix transport in synthesized α -helices still only reach 12 nm [17], it appears as though the pili use a novel mechanism of long distance electron transport. Development and optimization of the potential applications discussed in Chapter 1 would require an understanding of the biological electron transport process.

In scanning tunneling microscopy experiments (Chapter 5), we observed asymmetries in the topography and spectroscopy. The apparent heights in the topographs, proportional to an integral over the local density of states between the sample voltage and zero, indicated that opposite sides of the nanowire have enhanced states at opposite polarities at high (~ 1 V) tip-sample voltage. Direct acquisition of dI/dV , which was directly proportional to the local density of states at the position of the tip, showed curves at opposite edges of the nanowire that were consistent with this observation. The calculated asymmetry factors at the sample voltages at which the asymmetric images were obtained (± 1.0 V), which quantified the direction and magnitude of the dI/dV asymmetry (Eqn. 5.1), ranged from -1.3 on one edge of the nanowire to +1.7 on the opposite edge. The helical symmetry of the assembled pilus suggests that the tip-molecule-substrate pathway may be repeated lengthwise down the axis. (For a representation of this symmetry, refer to the structural model for the Type IV PAK pilus, in Fig. 3.2(d)). A model developed by Kuznetsov [128] began

with the STM configuration having redox energy levels in the probed molecule sandwiched between the tip and sample and predicted an asymmetric dI/dV . We could speculate that perhaps the assembly of dipolar subunits in the pilus (Chapter 3) is such that it provides the same potential drop simulated by the tip-substrate potential difference. Rectifying pilus nanowires may be biologically relevant as the cell wants to move electrons unidirectionally toward external acceptors (Chapter 3).

While investigation of this apparent rectifying behavior was one motivation for measuring the transport properties of the pilus nanowires, micron distance transport of any character would require a novel biological electron transport mechanism. This was the primary reason we employed CP-AFM to perform such an investigation (Chapter 6). At the time of this writing, we have achieved convincing preliminary evidence for at least 200 nm charge transport, with resistances at this distance of tens of megaohms, inferring an upper bound on the longitudinal resistivity of 0.4 Ω -cm. However, the present size of the data set (one nanowire curve) is insufficient to make firm conclusions about either the distance across which the pilus nanowires may transfer electrons or the electronic structure involved in that long-range transport. This is an active experiment in our lab at this time.

We have demonstrated protein conductivity in the absence of metals, and preliminary evidence suggests that this electron transport is indeed long-range. Yet questions remain. Though preliminary pilus structure models [88] indicate aromatic residues that may help facilitate tunneling or hopping reactions, this alone does not explain sustained transport across micron distances. In other systems, feedback mechanisms propel electrons via quasiparticle states like polarons (electrostatic interaction) and Davydov solitons (vibrational interaction in alpha helices). The polar pilin subunits in the nanowire may be suggestive of the former,

while their alpha helical nature may be suggestive of the latter. The fact that nuclear motion is a degree of freedom in biological ET would accommodate a feedback mechanism as well. The question of how long-range transport proceeds is a very difficult one. On the following pages, I conclude this dissertation by suggesting ways in which scanning probe techniques in particular may continue to further elucidate the pilus electronic structure.

Future Directions

Future study of this system with scanning probes should continue to exploit their powerful topographic and electronic acquisition capabilities. Postulating that known electron transfer mechanisms are elements of the more complicated pilus electron transport system, we may direct future scanning probe experiments to study their contributions piece by piece. While pure electron tunneling has no temperature dependence, it does vary exponentially with distance between initial and final states. Thermally activated hopping events, meanwhile do depend on temperature but their distance dependence is not necessarily exponential. Because of the sensitive distance dependence of tunneling, biological ET processes generally transition to hopping mechanisms beyond ~ 2 nm. Since even hopping conductivity should die out by the time distances reach tens of nanometers, we should consider both tunneling and hopping as possible players in the overall system. The introduction of modified pili from genetic modification or selective pressure would provide a source of varied structure, such as variable distance between donor and acceptor states for electrons. Modification may involve insertion or deletion of amino acids to change distances without altering the higher order structure. Access to cryogenic SPM will allow our lab to observe changes in electronic structure with decreasing temperature. Modeling of the electronic and molecular structure of the pilus nanowires will greatly enhance our ability to interpret data and develop new

experiments.

Our most widely used probe so far, the STM, is indispensable for the examination of the local electronic states of the pili. We could extend our proven ability to spatially distinguish variation in the density of states to detect changes in the electronic signature when we introduce modified pili and/or vary the temperature. We might observe these subtle variations either in imaging or dI/dV versus voltage curves. Though topographic imaging is sensitive to integrated density of states, scanning tunneling spectroscopy imaging (STS) may be able to image the relative magnitude of a localized state with more sensitivity. STS, as described in Chapter 2.1.3, gives a topographic image of the magnitude of the local density of states at a particular tip-sample voltage. If it is indeed possible to image localized “hot spots” of conductivity in this way, then we could observe how the position or magnitude change when we alter the D-A distances or temperature. This is of course somewhat speculative and depends on the hope that STS would be possible and robust for this soft organic material.

Alternatively, in two-dimensional curves of dI/dV vs voltage, we may observe how the energy spectrum at a particular point itself changes as we adjust these variables. If the energy levels of the local states change, this may alter the asymmetry in some detectable way. If peaks in the dI/dV curve do correspond to redox potentials of terminal electron acceptors, as suggested in Chapter 5, we could observe how these energies and thus redox potentials may vary as well. This type of analysis has been achieved by others for c-type cytochromes, with comparison to theoretical redox levels and complementary electrochemical experiments [20]. The existence of an electronic model for the *Geobacter* pilus, complemented by a simulation of what electronic signature the tip would detect in the STM configuration, would greatly complement the interpretation of experimental data.

Another logical experimental direction for the future is the continued use of the dynamic CP-AFM transport technique. If indeed we isolate interesting modified pili, the transport technique could directly study the long-range transport dependence. Utilization of a cryogenic CP-AFM would allow similar measurements to take place while lowering the temperature. In this way, we could study the temperature dependence of the long distance transport to infer properties of the transport process.

These experiments may also play a role in informing the enhancement of the potential applications for *Geobacter* species and their pilus nanowires, discussed in Chapter 1. If STM can indeed identify reduction potentials, perhaps it may assist in engineering modified pili with reduction potentials optimized for specific toxic substances. For enhancement of *Geobacter* fuel cells, continued study of electronic properties of pili and modified pili could help identify optimal strains to use in fuel cell studies seeking optimal current output. Finally, if it is indeed possible to incorporate pilus nanowires into top-down or self-assembled—and possibly biocompatible—devices, then biodegradation may impede the lifetimes of these. Chemical fixation could preserve the pili long term, but common methods such as glutaraldehyde fixation can alter electronic properties. For this reason, it may be necessary in the long term to perform similar studies of the electronic properties of preserved pilus nanowires.

Most immediately, however, we should fall back toward the earth. Perhaps the most intriguing possible outcome from physical studies of the pilus nanowires over the next several years is the elucidation of a novel biological mechanism for electron transfer. The potential physics involved in sustaining transport over such long distances in a seemingly amorphous structure, some of which were broached in this chapter, promise to be interesting as well. Future study of the electronic properties by scanned probes and other means should continue

to drive toward the nature of this novel conduction mechanism.

APPENDICES

Appendix A

Tip-adsorbate distortions

The effects of geometric convolution and tunneling gap variability for adsorbates were first discussed in Chapter 2.2.2. These effects have been studied in detail by Biro, *et al.* [44, 54, 114, 134] while interpreting STM images of carbon nanotubes (CNT). Because of the large radius of curvature of the tip, the leading tip edge begins to image the filamentous adsorbate much earlier than an infinitesimally small tip would (Fig. A.1(a)). As a result, the tip follows a contour defined by its effective finite radius. This effective radius includes the tunneling gap, in addition to the physical radius of curvature. In practice, we would like to be able to quantitatively determine the amount of broadening of a filamentous feature, such as a nanowire. The effective tip radius must be determined experimentally for the same tip used to image the nanowire. Characterizations of tip radii *ex situ* via scanning electron microscopy (SEM) or transmission electron microscopy (TEM) may estimate the tip radius, with some predictability. An *in situ* method of estimating the tip radius is more desirable. This may be done by analyzing images of step edges on the same surface that contains adsorbates (Fig. A.1(b)) [54]. Most step edges are in effect atomically sharp. Rather than

the tip imaging the step edge, the smaller effective radius of the step edge images the tip. From geometric arguments alone, one can show that the effective tip radius is given by:

$$R_{eff} = \frac{L^2 + h^2}{2h} \quad (\text{A.1})$$

where L is the *apparent* step width in the image, and h is the height of the step edge (presumed to be much more accurate), as illustrated in Fig. A.1(b). Once the tip radius is determined by analyzing the line profile of a step edge, the apparent diameter of an imaged nanowire may be expressed, also via geometric arguments, as:

$$\frac{D_{app}}{2} = \sqrt{(2R_{eff} - \delta)(D + \delta)} \quad (\text{A.2})$$

Where D_{app} is the apparent diameter and δ is the separation between an adsorbate and the substrate. The expression may be solved for the actual width, D , of the nanotube. Typical values of δ for a carbon nanotube on a substrate are $\sim 3 \text{ \AA}$ [44].

For adsorbates with very large heights, $\gtrsim 10 \text{ nm}$, the active tip must indeed be approximated by a cone rather than a sphere (see Fig. A.1(c)). The tip begins to contact the adsorbate much sooner, and the radius of the cone at the point of contact will be added to the smearing effect. The tip pulls out following a path along the cone until the active tip region reaches the spherical regime. This again broadens the measured diameter [54]:

$$D_{app} = D + 2R_c \quad (\text{A.3})$$

$$2R_c = 2H \tan\left(\frac{\beta}{2}\right) \quad (\text{A.4})$$

where H is the height of the point of contact of the adsorbate with the tip, R_C is the cone radius, and β is the apex angle of the cone.

Even when tip preparation methods are followed identically, the exact tip radius is not reproducible with a sufficient level of accuracy. As a general rule for imaging large adsorbates or surface structures, one would like the smallest nominal tip radius possible, with the smallest cone apex angle. The actual tip radius may then be determined *in situ*. Experimental determination of the sizes of adsorbates must consider geometric convolution of the tip and sample. Broadening by as much as 50% for 10 nm CNT and as much as 300% for 1 nm CNT has been observed [54].

In addition to lateral broadening, STM topography of CNT often shows anomalously small apparent heights as well [55, 56]. Typically, this reduction in apparent height is roughly 10% for CNT [44]. This issue has been attributed to several possible factors [54, 44] that should not be unique to CNT studies. Differences in work function between the substrate and adsorbate is one effect that could dominate. If the tunneling decay length is significantly decreased as the tip reaches the adsorbate, the tip-sample gap is much smaller, and this results in the feedback circuit reporting a reduced height. In addition, the interface of the adsorbate and the substrate results in a second tunneling gap, in addition to the tip-adsorbate gap (Fig. A.1(d)). Intuitively, this would lead to a reduced tunneling probability, and in fact simulations have shown that a significant fraction of tunneling electrons originating from the tip is reflected back into the tip at the adsorbate-substrate tunneling junction [54]. Another possible explanation for vertical flattening is again a consideration of geometric effects on the tunnel gap. Larger radii of curvature for the tube-like adsorbates [44] and the tip itself [44, 135] lead to a smaller tunneling gap and thus a flattened apparent height.

Finally, mechanical deformations in the adsorbate from the tip and the substrate, which are difficult to quantify, may also affect the measured height. Thus, it is clear that apparent heights when measured with STM must be analyzed with care.

In summary, when imaging molecular adsorbates, the finite tip radius and conic geometry can lead to a lateral broadening of the imaged molecule. A varying tunneling gap is thought to be the largest contributor to the flattening of the apparent height of these adsorbates. These issues must be considered along with those addressed in Section 2.1.2 when interpreting images of adsorbates.

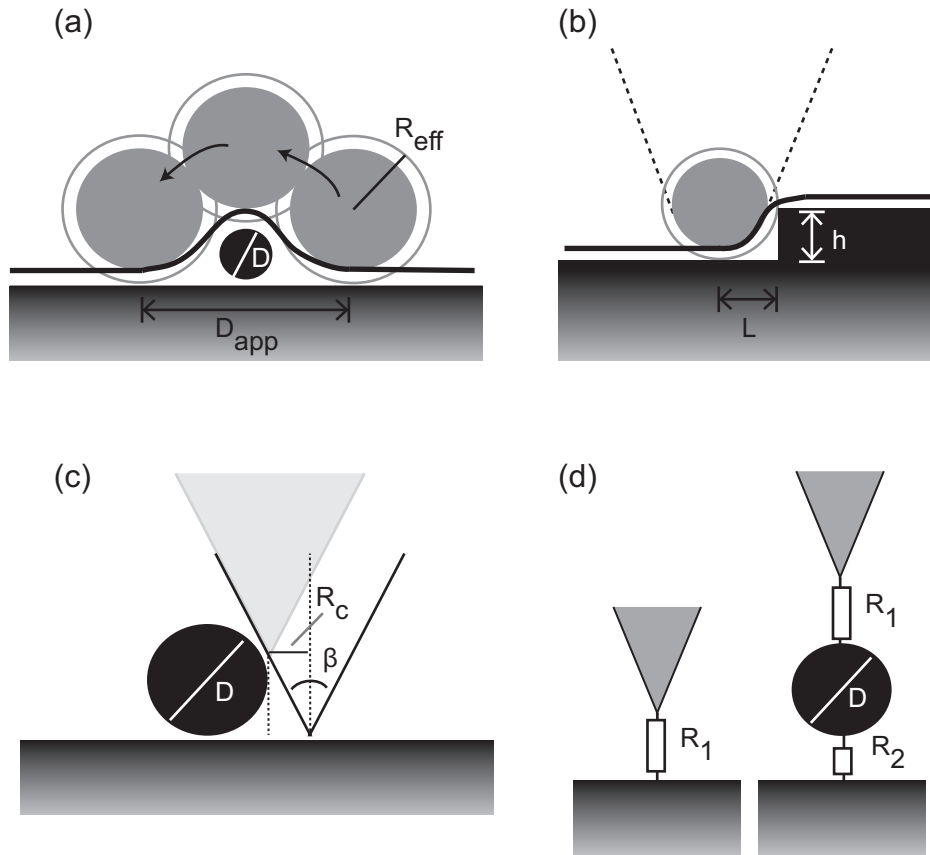


Figure A.1: Examples of geometric distortions due to finite tip geometry. (a) Filament (black) of diameter D is broadened when scanning with a tip of finite radius R_{eff} . (b) Broadening of a step edge due to finite tip radius. L is the apparent length over which the step edge rises. This may be used to quantify the effective tip radius. (c) Geometric distortion for large filament where tip is approximated as a cone. The apparent radius is broadened due to imaging before apex reaches the filament. (d) Schematic of tunneling junctions for tip-surface and tip-molecule-surface configurations. The interface between the molecule and the surface acts as a second tunneling junction.

Appendix B

AFM characterization of pilus height

An approximation of the heights of adsorbates in scanning probe experiments requires careful consideration of the imaging mechanism. In Chapter 5, we discussed that when imaging with STM, due to the difference in work function between substrate and adsorbate, the tunneling gap may change and thus give an apparent height that is misleading. The AFM, however, does not suffer from this problem because the imaging does not depend on a tunneling current. We therefore used AFM in tapping mode as another means to measure the height and compared it with STM. Figure B.1 shows a representative line profile of several pili from a purified sample prepared in the same way as described in Chapter 5.1. Because this and other similarly prepared samples contained aggregates of multiple pili, the line cut was taken across the smallest filaments on the surface, presumably individual wires. The apparent heights measured this way were 1–2 nm, compared with STM, which measured 0.8–1.2 nm. As discussed in Chapter 5, it is possible that some physical flattening has taken place during deposition. In the AFM setup we used for this measurement, the lateral broadening—analogueous to that for STM—is quite large, and the apparent pilus width here

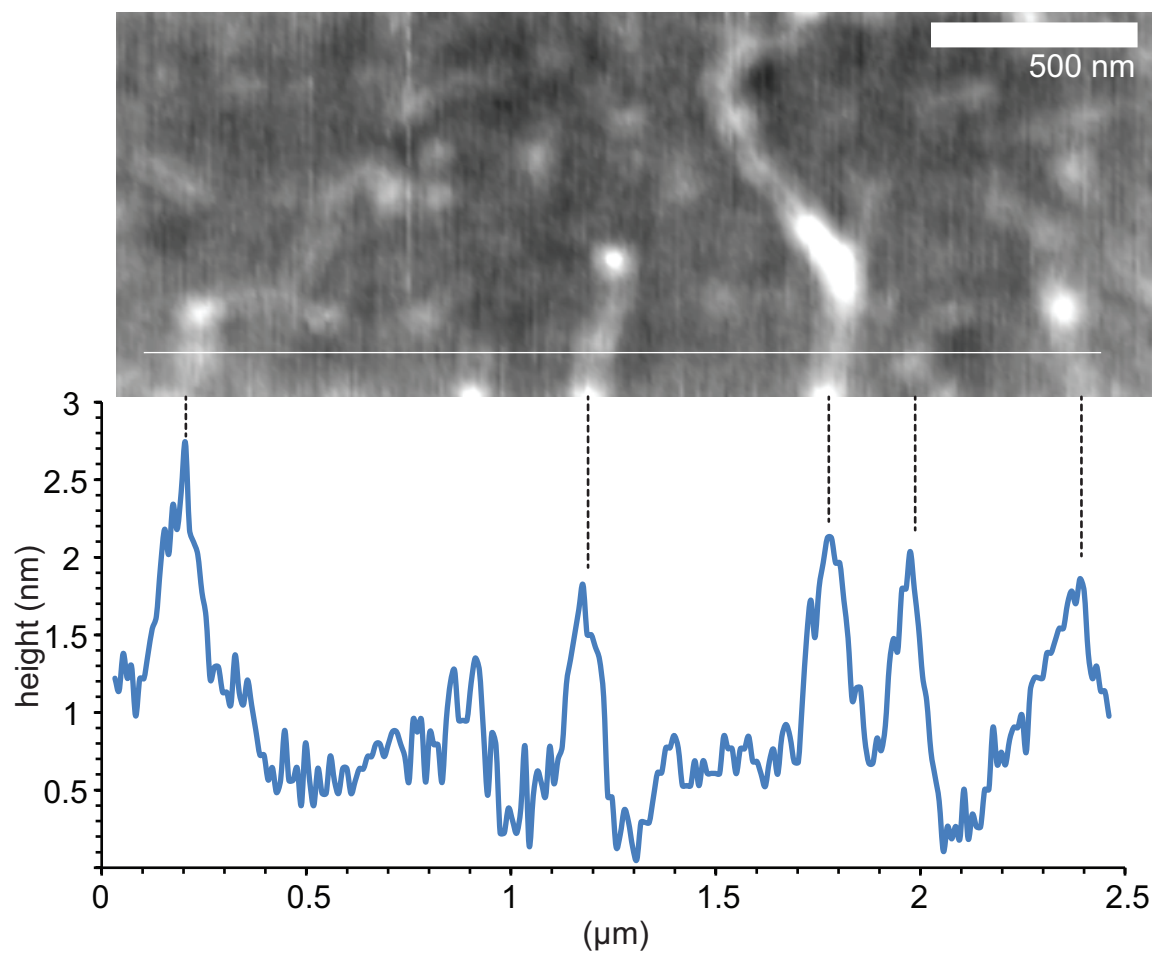


Figure B.1: Representative AFM line profile of several pili. The white line marks the location of the cut.

is neither accurate nor of any consequence to the height measurement.

Appendix C

Subsurface atom contribution to tunneling current in CeTe_3

Rare earth tellurides (RTe_3) are a family of layered materials that have received much attention as model systems to study incommensurate charge density waves (CDWs) [136, 137, 138]. The characteristic square net of the cleaved surface in these materials forms a one-dimensional CDW driven by Fermi-surface nesting [139]. CeTe_3 in particular forms a CDW energy gap of ~ 400 mV [140, 141, 142] at even room temperature, and the CDW remains at temperatures as high as 500 K [143]. Below 10 K, CeTe_3 becomes a weak Kondo lattice and then transitions to an antiferromagnetic ground state ($T_{Nee\ell}=2.8$ K) [141]. The f electrons in the cerium atoms are the sources of the magnetic moments leading to these properties.

The undistorted crystal structure of CeTe_3 is shown in Figure C.1. It is a weakly orthorhombic, NdTe_3 type, described within the space group $Cmcm$ [144, 145]. Corrugated and covalently bonded CeTe slabs are sandwiched between double Te net layers between

which a weak van der Waals attraction allows an easy cleavage plane for surface studies like those involving STM. In analyses of Fourier transform (FT) images from STM topographs, a CDW peak consistent with $q_{CDW} = 3.9 \text{ nm}^{-1}$ is observed, along with interesting satellite peaks (Fig. C.2, C.3, [146]). These are explained by a wave vector mixing analysis given in Ref. [146]. The nature of the other peaks, marked q_{atom} is the focus of the investigation described here. These peaks form an additional square lattice that may be interpreted as either subsurface atoms or dimerizations (Section C.2.1). We present room temperature and low temperature STM data, along with simulations of STM images to elucidate the nature of the q_{atom} peaks. Detailed analysis of the data with regard to the CDW is not the focus of this discussion, so I refer the reader to [146, 147] for more information.

C.1 Materials and Methods

We performed STM topography on freshly cleaved surfaces of CeTe_3 at both room temperature ($\sim 300 \text{ K}$) and 77 K . CeTe_3 crystals were grown by halide flux method [148]. For room temperature STM measurements described here, we used adhesive tape to cleave the crystal in a nitrogen glove bag and then placed the sample directly into the table-top Nanosurf STM operating inside the same glove bag. For low temperature experiments described here, we cleaved the CeTe_3 crystal in air and then immediately placed it into the high vacuum chamber coupled with the Besocke-style STM and Dewar, and began pumping before cooling down. The steps taken during cleaving minimize contamination that may form within minutes on the CeTe_3 surface.

Two-dimensional Fourier transform (FT) image production and reverse FT filtering were performed with SPIP software (Image Metrology). Simulations of STM data were performed

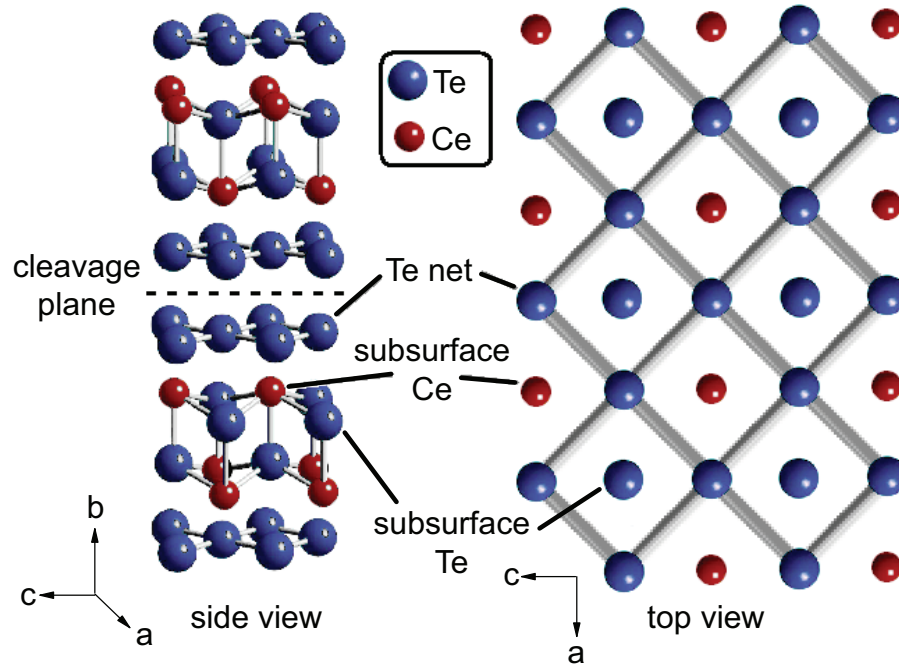


Figure C.1: The average (undistorted) crystal structure of CeTe_3 consisting of CeTe slabs corrugated as shown, separated by a double layer of a 3.1 \AA square Te net. The side view shows two complete unit cells repeated along the \vec{b} axis (vertical, perpendicular to the cleavage plane). The top view shows the exposed surface upon cleaving, displaying the square Te net and positions of the subsurface Te and Ce atoms. The subsurface Ce atoms are 2.53 \AA below the Te net, while the Te atoms are 3.44 \AA below.

by collaborators in the Mahanti group at MSU using electronic structure calculations within density-functional theory, described in more detail in Ref. [146].

C.1.1 Cryogenic operation of Besocke STM

I briefly mentioned in Chapter 2.3.2 the capability of our Besocke microscope to operate with the sample and scan head at cryogenic temperatures. The scan head attaches to the end of a long stick that extends down to the center of a Dewar housing a helium-3 refrigerator. In this refrigerator, a sample space is kept at high vacuum and the microscope is in good thermal contact with the cryostat pot via copper contacts. Our refrigerator operates at several base temperatures. Liquid nitrogen cools the Dewar to the nitrogen boiling point of 77 K for either operation at this base temperature or as a precooling step for lower temperatures. To reduce the temperature further, the nitrogen is removed and backfilled with liquid helium-4, the boiling point of which is 4 K. Precooling with nitrogen is desirable because it is significantly less expensive than helium-4. Pumping on the helium-4 lowers the vapor pressure, allowing the temperature to drop to 1.2 K. After this, the introduction and pumping of helium-3 in a separate pot cools the Dewar more. The helium-4 in the 1 K pot cools and condenses the helium-3 into a liquid. Pumping on the helium-3 reduces its temperature to 0.2 K, which is the lowest temperature this type of refrigerator may reach. Because helium-3 is rare and quite expensive, we would like to recycle it. For this reason, a sorb pump is selected to pump on the helium-3 so that the refrigerator may reach 0.2 K. The sorb is a porous charcoal collar wrapped around the helium-3 pot that captures the helium-3 vapor. When all the helium-3 evaporates, it may be recovered by re-condensing, either back into the helium-3 pot or into a helium-3 storage Dewar. The experiments described in this appendix, however, were only

performed at the liquid nitrogen base temperature (77 K).

In order to prevent thermal shock to the piezo tubes or other sensitive components, the scan head must be lowered slowly into the Dewar, a process which takes several hours. A flange on the stick meets with the opening to the sample space, and the stick slides through the flange via a sliding seal. To maintain vacuum, a mechanical pump pumps on the sliding seal while the stick is moved. Under ideal Dewar conditions, the sample space itself can reach vacuum levels of 10^{-7} torr with the use of a turbo pump. The properties of the piezoelectric materials change with temperature, so when operating at low temperature, it is necessary to use a different calibration to determine scan sizes. For example, at nitrogen temperature, piezo motion is reduced by roughly a factor of three for the same voltage at room temperature. Coaxial cables attached to the tip, sample, and piezo tubes run from the scan head, through the center of the stick, outside to the control box.

C.2 Results and Discussion

To investigate the nature of this surprisingly large additional square lattice contribution (the q_{atom} peaks), we directed a series of STM experiments and simulations specifically to this task. We complemented existing and new room temperature STM with low temperature (77 K) STM [146, 147]. Because of the reduced thermal and vibrational noise, low temperature STM is generally much cleaner and is able to more clearly resolve structure and thus FT peaks.

Figures C.2 and C.3 show STM topographs and FT obtained at room temperature and 77 K, respectively. In the room temperature data, it is clear from the topograph and its reverse FT that the STM resolves the surface lattice and CDW modulation. The reverse FT

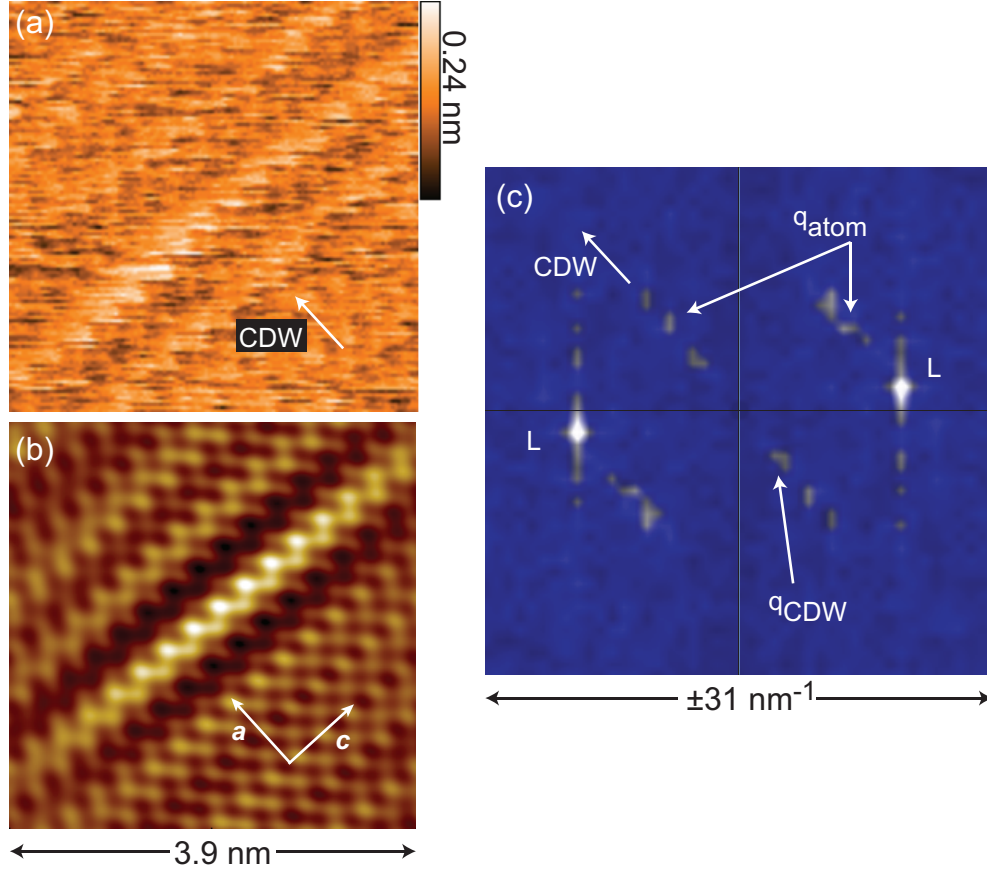


Figure C.2: Room temperature STM topography. Raw topography (a) and reverse FT (b) clearly showing both the square surface Te net and the CDW oriented 45° relative to the net. (b) was obtained by filtering noise below a certain threshold magnitude in the Fourier transform. This image also shows the location of the \vec{a} and \vec{c} lattice vectors. (c) FT image obtained by adding the square root sum of six topographs taken consecutively. The color scale is the relative Fourier magnitude, where blue to white corresponds to low to high magnitude. Two of the peaks corresponding to the surface Te net are labeled L , and the other two were lost when filtering out noise lying along the vertical axis that was an artifact of the scan direction. One of the peaks corresponding to the CDW wave vector is marked, along with two of the four peaks corresponding to the larger square lattice rotated 45° relative to the surface Te net. (sample voltage=800 mV; $I=50$ pA)

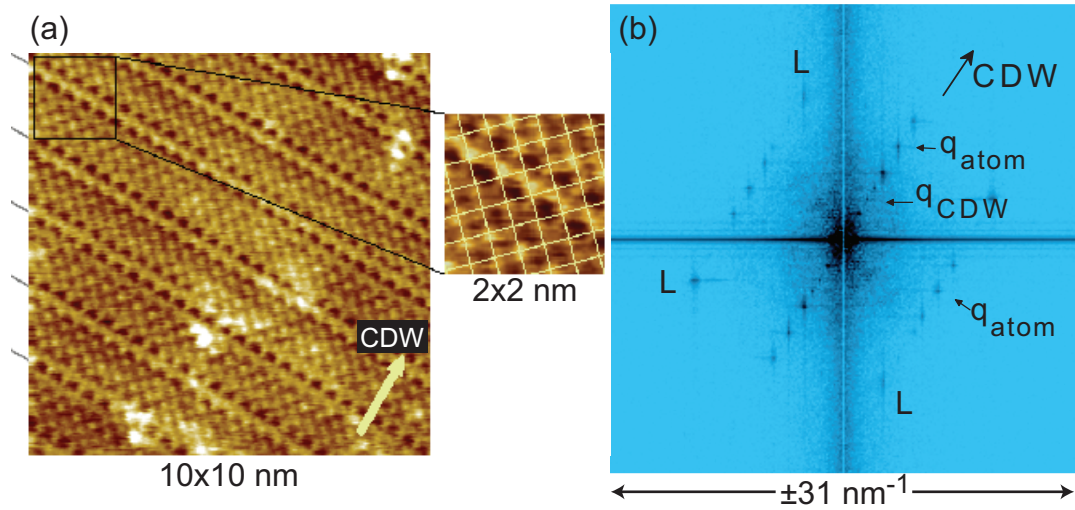


Figure C.3: Low temperature STM topography (77 K). (a) Topograph again showing the surface Te and several periods of the CDW. The image is the average of four images that were obtained consecutively. The bright irregular features indicate surface contamination. A lattice grid, where line intersections indicate surface Te locations, is superimposed on the 2 nm x 2 nm inset. The grey lines on the left side of the topograph indicate CDW maxima. (b) Fourier transform of the low temperature data in (a). The color scale is the relative Fourier magnitude, where blue to black corresponds with low to high magnitude. The same peaks are labeled as in (a), but are much more clearly distinguished in the low temperature data, where STM is more thermally stable. (sample voltage=100 mV; $I=0.6$ nA)

allows filtering of background noise to enhance the contrast from the lattice and CDW. In the FT image (Fig. C.2(c)), we observe some of the satellite peaks also observed in Ref. [149]. The low temperature data of Fig. C.3 are much clearer. We observe clear peaks from the Te net, the CDW and satellite peaks, and the additional square lattice peaks that are the subject of this study. We will discuss this in more detail now.

C.2.1 Secondary square lattice

In addition to Fourier transform (FT) peaks corresponding to the square net and the CDW, we also observed an additional square lattice oriented at 45° relative to the Te net, with $k = 2\pi/c = 14.3 \text{ nm}^{-1}$ [146, 149]. Here, \vec{c} is the lattice vector that points in the direction of the CDW (Fig. C.1). This location and spacing were consistent with both the subsurface Ce and Te atoms. It may show that STM has access to the f electrons near the Fermi level of the cerium atoms. This signature was also consistent, however, with dimerizations observed in the related material TbTe_3 at sample voltage outside the CDW gap [5]. This is because the FT retains no information about the phase, so equal \vec{k} vectors with different phases appear identical in the FT image. Figure C.4(a) shows an illustration of how these dimerizations have equivalent spacing and thus identical FT signatures. In the report of Fang, *et al.* [5], the dimerizations are not due to displacement of the atoms themselves, but rather enhanced tunneling signal between pairs of atoms. This is why the signature from the surface Te net is not destroyed.

To elucidate the source of the contribution to this additional lattice, we first addressed the question of whether the peaks arise from dimerizations, as were observed for TbTe_3 . In Figure C.4(b) and (c), I show STM topographs taken on CeTe_3 under the same tunneling

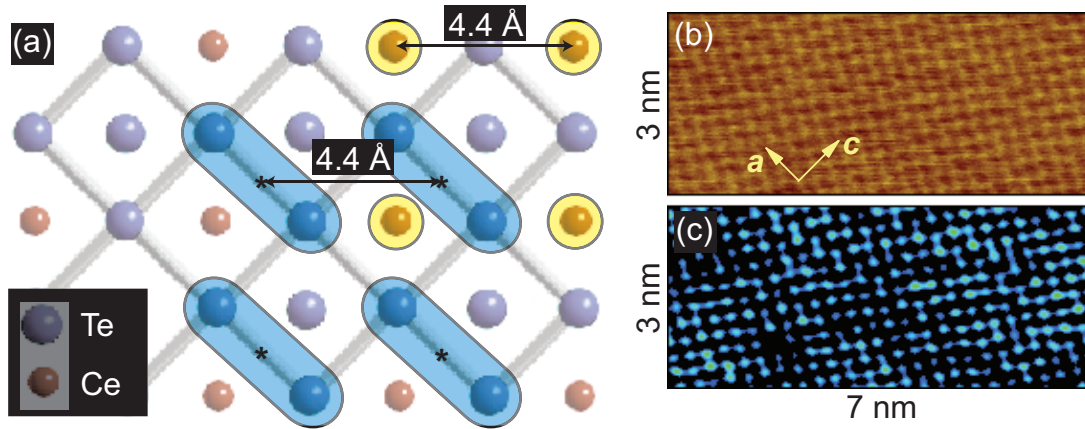


Figure C.4: (a) Cartoon showing the locations of dimers observed with STM for the related material TbTe_3 in Reference [5], as well as the locations of the subsurface Ce and Te atoms. Because the Fourier transform lacks phase information, the square net rotated at 45° relative to the Te net observed in our Fourier transforms of CeTe_3 (Figs. C.2 and C.3) could be due to either these dimers or to the subsurface Ce or Te net. (b) STM topography of CeTe_3 at room temperature and sample voltage -800 mV, the same used when dimerizations were observed in Ref. [5]. The current set point here was 140 pA, which was necessary to achieve quality comparable to that of [5]. We did not observe evidence of dimerizations in CeTe_3 under these conditions. Lower quality images at 50 pA also lacked evidence of dimerizations. The image is raw data, aside from line by line subtraction. (c) Low-pass ($|k| < 26 \text{ nm}^{-1}$) Fourier filtered image of the same data as in (a), given in high contrast for comparison with [5].

conditions as Ref. [5] on TbTe_3 . We observed no evidence of dimerizations in either the raw data or the reverse FT enhanced topographs. Moreover, we did not see evidence for dimerization in the hundreds of images taken of CeTe_3 over a broad set of voltages in the range ± 800 mV. This suggests that the secondary square lattice peaks are due to either subsurface Ce or subsurface Te.

To the naked eye, the subsurface structure is less apparent in the real space data of Fig. C.4, but the representative FT in Fig. C.2 demonstrates that the contribution of this secondary square lattice is present here, even in the absence of dimers. So why then should we expect that, if present, we would have been able to observe dimers here in the real space data alone? The relative magnitude of the tunneling signal in the dimerizations of Ref. [5] suggests that if they existed, they should be quite strong and thus visible in our own real space imaging. However, by contrast, the subsurface peaks observed in Figs. C.2, C.3, and Refs. [146, 149] in the absence of easy real space STM observation of the subsurface lattice suggests that the magnitude of the subsurface contribution is small enough that it is typically difficult to see with the naked eye in real space images.

Next, we address the question of whether the subsurface contribution comes from the subsurface Ce or subsurface Te atoms. The subsurface Ce is closer (2.53 \AA) to the surface than the subsurface Te (3.44 \AA), but this does not directly imply a larger contribution to the tunneling current. Figure C.5 shows a simulation of an STM image at sample voltage 100 meV and temperature 77 K taken at the approximate position of the tip above the surface (3 \AA). These were the same conditions as Fig. C.3. The subsurface Ce contributes more to the charge density than the subsurface Te, suggesting that the Ce sites are more likely to contribute tunneling current to the image.

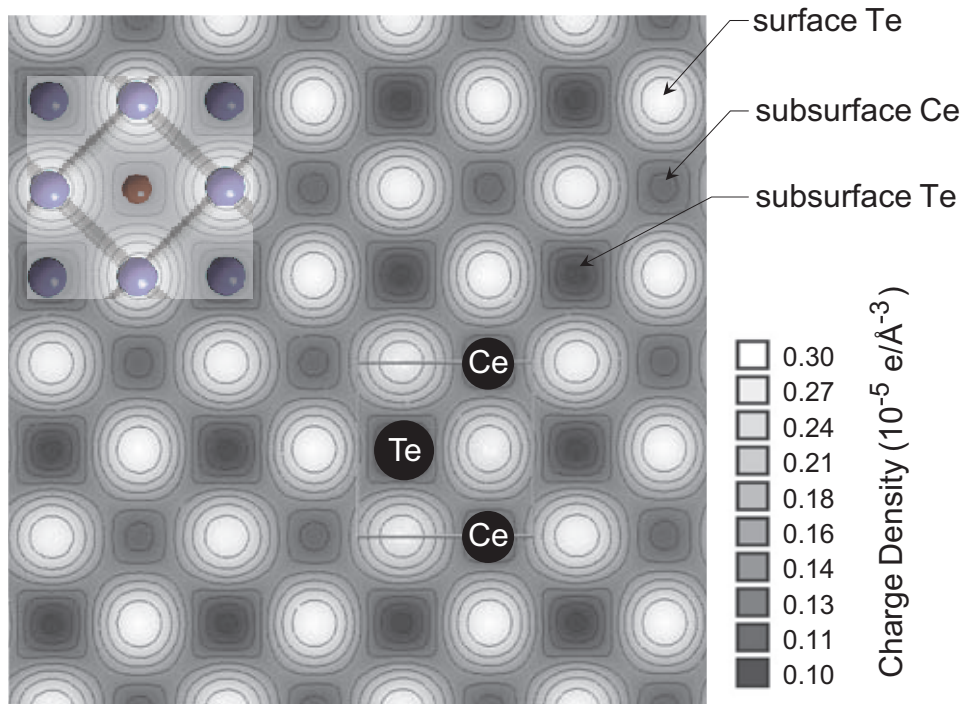


Figure C.5: Simulation of STM image to investigate the relative contributions of the subsurface Ce and Te to the topography that results in the square lattice rotated 45° to the surface Te net. The image here is a contour plot of the charge density projected onto a plane at 3.0 \AA above the surface (roughly the distance to the tip), in the energy range of $0.0\text{-}0.1 \text{ eV}$. The subsurface Ce atoms contribute more to the charge density than the subsurface Te atoms. The Fermi level corresponds to 0.0 eV . Moreover, the subsurface modulation is of comparable magnitude to the signal from the surface Te net.

Barring any other unknown electronic contributions, we conclude that the surprisingly large secondary square lattice contribution to the tunneling current comes about from the subsurface Ce atoms. For most materials, STM only has access to electrons at the surface. That STM may be able to probe the f electrons in the subsurface Ce presents the possibility of examining the electronic structure of the Kondo lattice with STM below 10 K. Thus far, STM has only studied Kondo properties for surface magnetic impurities on metals. Despite the certain experimental challenges, it is an exciting prospect.

REFERENCES

REFERENCES

- [1] G. Reguera, K. D. McCarthy, T. Mehta, J. S. Nicoll, M. T. Tuominen, and D. R. Lovley, “Extracellular electron transfer via microbial nanowires,” *Nature*, vol. 435, pp. 1098–1101, June 2005.
- [2] Reprinted from *Surface Science*, vol. 181, R. Hamers, R. Tromp, and J. Demuth, “Electronic and geometric structure of Si(111)-(7x7) and Si(001) surfaces,” pp. 346–355, Copyright 1987, with permission from Elsevier [49].
- [3] L. Craig, M. E. Pique, and J. A. Tainer, “Type IV pilus structure and bacterial pathogenicity,” *Nature Reviews Microbiology*, vol. 2, pp. 363–378, May 2004.
- [4] Reprinted from *Surface Science*, vol. 511, P. Simonis, C. Goffaux, P.A. Thiry, L.P. Biro, P. Lambin, and V. Meunier, “STM study of a grain boundary in graphite,” pp. 319–322, Copyright 2002, with permission from Elsevier [93].
- [5] A. Fang, N. Ru, I. R. Fisher, and A. Kapitulnik, “STM studies of TbTe₃: evidence for a fully incommensurate charge density wave,” *Physical Review Letters*, vol. 99, p. 046401, July 2007.
- [6] D. R. Lovley, E. J. P. Phillips, Y. A. Gorby, and E. R. Landa, “Microbial reduction of uranium,” *Nature*, vol. 350, pp. 413–416, Apr. 1991.
- [7] D. R. Lovley, M. J. Baedeker, D. J. Lonergan, I. M. Cozzarelli, E. J. P. Phillips, and D. I. Siegel, “Oxidation of aromatic contaminants coupled to microbial iron reduction,” *Nature*, vol. 339, pp. 297–300, May 1989.
- [8] D. R. Lovley and D. J. Lonergan, “Anaerobic oxidation of toluene, phenol, and p-cresol by the dissimilatory iron-reducing organism, GS-15,” *Applied and Environmental Microbiology*, vol. 56, no. 6, pp. 1858–1864, 1990.

- [9] R. T. Anderson, H. A. Vrionis, I. Ortiz-Bernad, C. T. Resch, P. E. Long, R. Dayvault, K. Karp, S. Marutzky, D. R. Metzler, A. Peacock, D. C. White, M. Lowe, and D. R. Lovley, "Stimulating the *in situ* activity of *Geobacter* species to remove uranium from the groundwater of a uranium-contaminated aquifer," *Applied and Environmental Microbiology*, vol. 69, pp. 5884–5891, Oct. 2003.
- [10] D. R. Lovley, J. C. Woodward, and F. H. Chapelle, "Rapid anaerobic benzene oxidation with a variety of chelated Fe(III) forms," *Applied and Environmental Microbiology*, vol. 62, pp. 288–91, Jan. 1996.
- [11] T. Zhang, S. M. Gannon, K. P. Nevin, A. E. Franks, and D. R. Lovley, "Stimulating the anaerobic degradation of aromatic hydrocarbons in contaminated sediments by providing an electrode as the electron acceptor," *Environmental Microbiology*, vol. 12, pp. 1011–20, Apr. 2010.
- [12] D. Cologgi, A. Speers, S. Lampa-Pastirk, S. Kelly, and G. Reguera, "Extracellular reduction of uranium via *Geobacter*'s conductive pili as a protective cellular mechanism." in preparation, 2011.
- [13] G. Reguera, R. B. Pollina, J. S. Nicoll, and D. R. Lovley, "Possible nonconductive role of *Geobacter sulfurreducens* pilus nanowires in biofilm formation," *Journal of Bacteriology*, vol. 189, pp. 2125–2127, Mar. 2007.
- [14] G. Reguera, K. P. Nevin, J. S. Nicoll, S. F. Covalla, T. L. Woodard, and D. R. Lovley, "Biofilm and nanowire production leads to increased current in *Geobacter sulfurreducens* fuel cells," *Applied and Environmental Microbiology*, vol. 72, pp. 7345–7348, Nov. 2006.
- [15] H. Yi, K. P. Nevin, B.-C. Kim, A. E. Franks, A. Klimes, L. M. Tender, and D. R. Lovley, "Selection of a variant of *Geobacter sulfurreducens* with enhanced capacity for current production in microbial fuel cells," *Biosensors & Bioelectronics*, vol. 24, pp. 3498–503, Aug. 2009.
- [16] H. B. Gray and J. R. Winkler, "Electron flow through proteins," *Chemical Physics Letters*, vol. 483, pp. 1–9, Nov. 2009.
- [17] Y. Arikuma, H. Nakayama, T. Morita, and S. Kimura, "Ultra-long-range electron transfer through a self-assembled monolayer on gold composed of 120 Å long α -helices," *Langmuir*, vol. 27, pp. 1530–1535, Nov. 2010.
- [18] G. B. Khomutov, L. V. Belovolova, S. P. Gubin, V. V. Khanin, A. Y. Obydenov, A. N. Sergeev-Cherenkov, E. S. Soldatov, and A. S. Trifonov, "STM study of morphology

- and electron transport features in cytochrome c and nanocluster molecule monolayers,” *Bioelectrochemistry*, vol. 55, pp. 177–181, Jan. 2002.
- [19] N. S. Wigginton, K. M. Rosso, B. H. Lower, L. Shi, and M. F. Hochella, “Electron tunneling properties of outer-membrane decaheme cytochromes from *Shewanella oneidensis*,” *Geochimica et Cosmochimica Acta*, vol. 71, pp. 543–555, Feb. 2007.
- [20] N. S. Wigginton, K. M. Rosso, and M. F. Hochella, “Mechanisms of electron transfer in two decaheme cytochromes from a metal-reducing bacterium,” *Journal of Physical Chemistry B*, vol. 111, pp. 12857–12864, Nov. 2007.
- [21] A. Alessandrini, S. Corni, and P. Facci, “Unravelling single metalloprotein electron transfer by scanning probe techniques,” *Physical Chemistry: Chemical Physics*, vol. 8, no. 38, pp. 4383–4397, 2006.
- [22] V. Frascerra, F. Calabi, G. Maruccio, P. P. Pompa, R. Cingolani, and R. Rinaldi, “Resonant electron tunneling through azurin in air and liquid by scanning tunneling microscopy,” *IEEE Transactions on Nanotechnology*, vol. 4, no. 5, pp. 637–640, 2005.
- [23] E. P. Friis, J. E. T. Andersen, Y. I. Kharkats, A. M. Kuznetsov, R. J. Nichols, J.-D. Zhang, and J. Ulstrup, “An approach to long-range electron transfer mechanisms in metalloproteins: *in situ* scanning tunneling microscopy with submolecular resolution,” *Proceedings of the National Academy of Sciences of the USA*, vol. 96, pp. 1379–1384, Feb. 1999.
- [24] J. Zhao, J. J. Davis, M. S. P. Sansom, and A. Hung, “Exploring the electronic and mechanical properties of protein using conducting atomic force microscopy,” *Journal of the American Chemical Society*, vol. 126, pp. 5601–5609, May 2004.
- [25] S. Huang, J. He, S. Chang, P. Zhang, F. Liang, S. Li, M. Tuchband, A. Fuhrmann, R. Ros, and S. Lindsay, “Identifying single bases in a DNA oligomer with electron tunnelling,” *Nature Nanotechnology*, vol. 5, pp. 868–873, Nov. 2010.
- [26] G. Binnig and H. Rohrer, “Scanning Tunneling Microscopy,” *Helvetica Physica Acta*, vol. 55, no. 6, pp. 726–735, 1982.
- [27] G. Binnig, C. Quate, and C. Gerber, “Atomic Force Microscope,” *Physical Review Letters*, vol. 56, pp. 930–933, Mar. 1986.

- [28] H. J. Butt, “Measuring electrostatic, van der Waals, and hydration forces in electrolyte solutions with an atomic force microscope,” *Biophysical Journal*, vol. 60, no. 6, pp. 1438–1444, 1991.
- [29] H. W. Hao, “Electrostatic and contact forces in force microscopy,” *Journal of Vacuum Science & Technology B: Microelectronics and Nanometer Structures*, vol. 9, p. 1323, Mar. 1991.
- [30] J. J. Saenz, N. Garcia, P. Grutter, E. Meyer, H. Heinzelmann, R. Wiesendanger, L. Rosenthaler, H. R. Hidber, and H.-J. Guntherodt, “Observation of magnetic forces by the atomic force microscope,” *Journal of Applied Physics*, vol. 62, no. 10, p. 4293, 1987.
- [31] G. Meyer and N. M. Amer, “Simultaneous measurement of lateral and normal forces with an optical-beam-deflection atomic force microscope,” *Applied Physics Letters*, vol. 57, no. 20, p. 2089, 1990.
- [32] D. Tománek, W. Zhong, and H. Thomas, “Calculation of an atomically modulated friction force in atomic force microscopy,” *Europhysics Letters*, vol. 15, pp. 887–892, Aug. 1991.
- [33] H. P. Kleinknecht, J. R. Sandercock, and H. Meier, “An experimental scanning capacitance microscope,” *Scanning Microscopy*, vol. 2, no. 4, pp. 1839–1844, 1988.
- [34] S. H. Tessmer, P. I. Glicofridis, R. C. Ashoori, L. S. Levitov, and M. R. Melloch, “Subsurface charge accumulation imaging of a quantum Hall liquid,” *Nature*, vol. 392, pp. 51–54, Mar. 1998.
- [35] I. Giaever, “Energy gap in superconductors measured by electron tunneling,” *Physical Review Letters*, vol. 5, pp. 147–148, Aug. 1960.
- [36] I. Giaever, “Electron tunneling between two superconductors,” *Physical Review Letters*, vol. 5, pp. 464–466, Nov. 1960.
- [37] I. Maggio-Aprile, C. Renner, A. Erb, E. Walker, and O. Fischer, “Direct vortex lattice imaging and tunneling spectroscopy of flux lines on $\text{YBa}_2\text{Cu}_3\text{O}_{7-\delta}$,” *Physical Review Letters*, vol. 75, pp. 2754–2757, Oct. 1995.
- [38] S. Pan, E. Hudson, A. Gupta, K.-W. Ng, H. Eisaki, S. Uchida, and J. Davis, “STM studies of the electronic structure of vortex cores in $\text{Bi}_2\text{Sr}_2\text{CaCu}_2\text{O}_{8+\delta}$,” *Physical Review Letters*, vol. 85, pp. 1536–1539, Aug. 2000.

- [39] J. J. Davis and H. A. O. Hill, "The scanning probe microscopy of metalloproteins and metalloenzymes," *Chemical Communications*, no. 5, pp. 393–401, 2002.
- [40] H. Ohtani, R. Wilson, S. Chiang, and C. Mate, "Scanning tunneling microscopy observations of benzene molecules on the Rh(111)-(3x3)(C₆H₆ + 2CO) surface," *Physical Review Letters*, vol. 60, pp. 2398–2401, June 1988.
- [41] S. Chiang, "Scanning tunneling microscopy imaging of small adsorbed molecules on metal surfaces in an ultrahigh vacuum environment," *Chemical Reviews*, vol. 97, pp. 1083–1096, June 1997.
- [42] K. Müllen and J. P. Rabe, "Nanographenes as active components of single-molecule electronics and how a scanning tunneling microscope puts them to work," *Accounts of Chemical Research*, vol. 41, pp. 511–20, Apr. 2008.
- [43] J. Bardeen, "Tunnelling from a many-particle point of view," *Physical Review Letters*, vol. 6, pp. 57–59, Jan. 1961.
- [44] L. Tapasztó, G. I. Márk, A. A. Koós, P. Lambin, and L. P. Biró, "Apparent diameter of carbon nanotubes in scanning tunnelling microscopy measurements," *Journal of Physics: Condensed Matter*, vol. 18, pp. 5793–5805, July 2006.
- [45] J. Tersoff and D. R. Hamann, "Theory and application for the scanning tunneling microscope," *Physical Review Letters*, vol. 50, p. 1998, June 1983.
- [46] J. Tersoff and D. R. Hamann, "Theory of the scanning tunneling microscope," *Physical Review B*, vol. 31, p. 805, Jan. 1985.
- [47] R. Hamers and D. Padowitz, "Methods of tunneling spectroscopy with the STM," in *Scanning Probe Microscopy and Spectroscopy* (D. Bonnell, ed.), New York: Wiley-VCH, 2nd ed., 2001.
- [48] R. Feenstra, J. A. Stroscio, J. Tersoff, and A. P. Fein, "Atom-selective imaging of the GaAs(110) surface," *Physical Review Letters*, vol. 58, no. 12, pp. 1192 – 1195, 1987.
- [49] R. Hamers, R. Tromp, and J. Demuth, "Electronic and geometric structure of Si(111)-(7x7) and Si(001) surfaces," *Surface Science*, vol. 181, pp. 346–355, Mar. 1987.
- [50] R. Feenstra, W. Thompson, and A. Fein, "Real-space observation of π -bonded chains and surface disorder on Si(111)2x1," *Physical Review Letters*, vol. 56, pp. 608–611, Feb. 1986.

- [51] E. L. Wolf, A. Chang, Z. Y. Rong, Y. M. Ivanchenko, and F. Lu, “Direct STM mapping of the superconducting energy gap in single crystal $\text{Bi}_2\text{Sr}_2\text{CaCu}_2\text{O}_{8+x}$,” *Journal of Superconductivity*, vol. 7, pp. 355–360, Apr. 1994.
- [52] S. H. Pan, J. P. O’Neal, R. L. Badzey, C. Chamon, H. Ding, J. R. Engelbrecht, Z. Wang, H. Eisaki, S. Uchida, A. K. Gupta, K. W. Ng, E. W. Hudson, K. M. Lang, and J. C. Davis, “Microscopic electronic inhomogeneity in the high- T_c superconductor $\text{Bi}_2\text{Sr}_2\text{CaCu}_2\text{O}_{8+x}$,” *Nature*, vol. 413, pp. 282–5, Sept. 2001.
- [53] R. M. Feenstra, J. A. Stroscio, and A. P. Fein, “Tunneling spectroscopy of the $\text{Si}(111)2\times 1$ surface,” *Surface Science*, vol. 181, pp. 295–306, Mar. 1987.
- [54] L. P. Biró, J. Gyulai, P. Lambin, J. B. Nagy, S. Lazarescu, G. I. Mark, A. Fonseca, P. R. Surján, Z. Szekeres, P. A. Thiry, and A. A. Lucas, “Scanning tunnelling microscopy (STM) imaging of carbon nanotubes,” *Carbon*, vol. 36, no. 5-6, pp. 689–696, 1998.
- [55] P. Kim, T. W. Odom, J. Huang, and C. M. Lieber, “STM study of single-walled carbon nanotubes,” *Carbon*, vol. 38, no. 11-12, pp. 1741–1744, 2000.
- [56] Z. Klusek, S. Datta, P. Byszewski, P. Kowalczyk, and W. Kozłowski, “Scanning tunneling microscopy and spectroscopy of Y-junction in carbon nanotubes,” *Surface Science*, vol. 507-510, pp. 577–581, June 2002.
- [57] D. Bonnell and B. Huey, “Basic principles of scanning probe microscopy,” in *Scanning Probe Microscopy and Spectroscopy* (D. Bonnell, ed.), New York: Wiley-VCH, 2nd ed., 2001.
- [58] C. Chen, *Introduction to Scanning Tunneling Microscopy*. New York: Oxford University Press, 1st ed., 1993.
- [59] M. Okano, “Vibration isolation for scanning tunneling microscopy,” *Journal of Vacuum Science & Technology A: Vacuum, Surfaces, and Films*, vol. 5, p. 3313, Nov. 1987.
- [60] K. Besocke, “An easily operable scanning tunneling microscope,” *Surface Science*, vol. 181, pp. 145–153, Mar. 1987.
- [61] J. Frohn, J. F. Wolf, K. Besocke, and M. Teske, “Coarse tip distance adjustment and positioner for a scanning tunneling microscope,” *Review of Scientific Instruments*, vol. 60, no. 6, p. 1200, 1989.

- [62] S. Urazhdin, S. H. Tessmer, and R. C. Ashoori, “A simple low-dissipation amplifier for cryogenic STM,” *Review of Scientific Instruments*, vol. 73, no. 2, p. 310, 2002.
- [63] T. R. Albrecht, P. Grutter, D. Horne, and D. Rugar, “Frequency modulation detection using high-Q cantilevers for enhanced force microscope sensitivity,” *Journal of Applied Physics*, vol. 69, no. 2, p. 668, 1991.
- [64] Q. Zhong, D. Inness, K. Kjoller, and V. Elings, “Fractured polymer/silica fiber surface studied by tapping mode atomic force microscopy,” *Surface Science Letters*, vol. 290, pp. L688–L692, June 1993.
- [65] J. J. Davis, D. A. Morgan, C. L. Wrathmell, D. N. Axford, J. Zhao, and N. Wang, “Molecular bioelectronics,” *Journal of Materials Chemistry*, vol. 15, no. 22, p. 2160, 2005.
- [66] J. N. Rooney-Varga, R. T. Anderson, J. L. Fraga, D. Ringelberg, and D. R. Lovley, “Microbial communities associated with anaerobic benzene degradation in a petroleum-contaminated aquifer,” *Applied and Environmental Microbiology*, vol. 65, pp. 3056–3063, July 1999.
- [67] O. L. Snoeyenbos-West, K. P. Nevin, R. T. Anderson, and D. R. Lovley, “Enrichment of *Geobacter* species in response to stimulation of Fe(III) reduction in sandy aquifer sediments,” *Microbial Ecology*, vol. 39, no. 2, pp. 153–167, 2000.
- [68] M. V. Coppi, C. Leang, S. J. Sandler, and D. R. Lovley, “Development of a genetic system for *Geobacter sulfurreducens*,” *Applied and Environmental Microbiology*, vol. 67, pp. 3180–3187, July 2001.
- [69] D. R. Lovley, “Dissimilatory Fe(III) and Mn(IV) reduction,” *Microbiology and Molecular Biology Reviews*, vol. 55, no. 2, pp. 259–287, 1991.
- [70] K. P. Nevin and D. R. Lovley, “Mechanisms for Fe(III) oxide reduction in sedimentary environments,” *Geomicrobiology Journal*, vol. 19, no. 2, p. 19, 2002.
- [71] L. Shi, T. C. Squier, J. M. Zachara, and J. K. Fredrickson, “Respiration of metal (hydr)oxides by *Shewanella* and *Geobacter*: a key role for multihaem c-type cytochromes,” *Molecular microbiology*, vol. 65, pp. 12–20, July 2007.
- [72] T. Mehta, S. E. Childers, R. Glaven, D. R. Lovley, and T. Mester, “A putative multi-copper protein secreted by an atypical type II secretion system involved in the reduc-

- tion of insoluble electron acceptors in *Geobacter sulfurreducens*,” *Microbiology*, vol. 152, pp. 2257–2264, Aug. 2006.
- [73] Y. Gorby, S. Yanina, J. S. McLean, K. M. Rosso, D. Moyles, A. Dohnalkova, T. J. Beveridge, *et al.*, “Electrically conductive bacterial nanowires produced by *Shewanella oneidensis* strain MR-1 and other microorganisms,” *Proceedings of the National Academy of Sciences of the USA*, vol. 103, no. 30, pp. 11358–11363, 2006.
- [74] M. Y. El-Naggar, Y. A. Gorby, W. Xia, and K. H. Nealson, “The molecular density of states in bacterial nanowires,” *Biophysical Journal*, vol. 95, pp. L10–L12, July 2008.
- [75] S. Lampa-Pastirk, J. P. Veazey, J. Sun, P. Zhang, S. H. Tessmer, and G. Reguera, “Long-range electron transfer via the protein matrix in *Geobacter*’s pilus nanowires.” in preparation, 2011.
- [76] H. B. Gray and J. R. Winkler, “Electron tunneling through proteins,” *Quarterly Reviews of Biophysics*, vol. 36, no. 03, pp. 341–372, 2003.
- [77] T. Brittain, “Intra-molecular electron transfer in proteins,” *Protein and Peptide Letters*, vol. 15, pp. 556–561, July 2008.
- [78] R. Marcus, “Electron transfers in chemistry and biology,” *Biochimica et Biophysica Acta - Reviews on Bioenergetics*, vol. 811, pp. 265–322, Aug. 1985.
- [79] J. J. Hopfield, “Electron transfer between biological molecules by thermally activated tunneling,” *Proceedings of the National Academy of Sciences*, vol. 71, pp. 3640–3644, Sept. 1974.
- [80] C. C. Moser, C. C. Page, and P. L. Dutton, “Darwin at the molecular scale: selection and variance in electron tunnelling proteins including cytochrome c oxidase,” *Philosophical Transactions of the Royal Society of London. Series B, Biological Sciences*, vol. 361, pp. 1295–305, Aug. 2006.
- [81] M. Cordes, A. Köttgen, C. Jasper, O. Jacques, H. Boudebous, and B. Giese, “Influence of amino acid side chains on long-distance electron transfer in peptides: Electron hopping via ‘stepping stones’,” *Angewandte Chemie International Edition*, vol. 47, no. 18, pp. 3461–3463, 2008.
- [82] C. Shih, A. K. Museth, M. Abrahamsson, A. M. Blanco-Rodriguez, A. J. Di Bilio, J. Sudhamsu, B. R. Crane, K. L. Ronayne, M. Towrie, A. Vlcek, J. H. Richards, J. R.

- Winkler, and H. B. Gray, "Tryptophan-accelerated electron flow through proteins," *Science*, vol. 320, pp. 1760–2, June 2008.
- [83] J. Stubbe, D. G. Nocera, C. S. Yee, and M. C. Y. Chang, "Radical initiation in the class I ribonucleotide reductase: Long-range proton-coupled electron transfer?," *Chemical Reviews*, vol. 103, pp. 2167–2202, June 2003.
- [84] S. Y. Reece, M. R. Seyedsayamdost, J. Stubbe, and D. G. Nocera, "Direct observation of a transient tyrosine radical competent for initiating turnover in a photochemical ribonucleotide reductase," *Journal of the American Chemical Society*, vol. 129, pp. 13828–30, Nov. 2007.
- [85] M. R. Seyedsayamdost, J. Xie, C. T. Y. Chan, P. G. Schultz, and J. Stubbe, "Site-specific insertion of 3-aminotyrosine into subunit $\alpha 2$ of *E. coli* ribonucleotide reductase: direct evidence for involvement of Y₇₃₀ and Y₇₃₁ in radical propagation.," *Journal of the American Chemical Society*, vol. 129, pp. 15060–71, Dec. 2007.
- [86] A. Lukacs, A. P. M. Eker, M. Byrdin, K. Brettel, and M. H. Vos, "Electron hopping through the 15 Å triple tryptophan molecular wire in DNA photolyase occurs within 30 ps," *Journal of the American Chemical Society*, vol. 130, pp. 14394–5, Nov. 2008.
- [87] C. Wittekindt, M. Schwarz, T. Friedrich, and T. Koslowski, "Aromatic amino acids as stepping stones in charge transfer in respiratory complex I: An unusual mechanism deduced from atomistic theory and bioinformatics," *Journal of the American Chemical Society*, vol. 131, pp. 8134–8140, June 2009.
- [88] R. Steidl, G. Reguera, *et al.* unpublished.
- [89] A. Davydov, "Solitons and energy transfer along protein molecules," *Journal of Theoretical Biology*, vol. 66, pp. 379–387, May 1977.
- [90] D. D. Dunlap and C. Bustamante, "Images of single-stranded nucleic acids by scanning tunnelling microscopy," *Nature*, vol. 342, pp. 204–206, Nov. 1989.
- [91] C. R. Clemmer and T. P. Beebe, "Graphite: a mimic for DNA and other biomolecules in scanning tunneling microscope studies," *Science*, vol. 251, pp. 640–642, Feb. 1991.
- [92] H. Chang and A. J. Bard, "Observation and characterization by scanning tunneling microscopy of structures generated by cleaving highly oriented pyrolytic graphite," *Langmuir*, vol. 7, pp. 1143–1153, June 1991.

- [93] P. Simonis, C. Goffaux, P. A. Thiry, L. P. Biro, P. Lambin, and V. Meunier, “STM study of a grain boundary in graphite,” *Surface Science*, vol. 511, pp. 319–322, June 2002.
- [94] M. Salmeron, T. Beebe, J. Odriozola, T. Wilson, D. F. Ogletree, and W. Siekhaus, “Imaging of biomolecules with the scanning tunneling microscope: Problems and prospects,” *Journal of Vacuum Science & Technology A: Vacuum, Surfaces, and Films*, vol. 8, pp. 635–641, Jan. 1990.
- [95] A. M. Baro, R. Miranda, J. Alaman, N. Garcia, G. Binnig, H. Rohrer, C. Gerber, and J. L. Carrascosa, “Determination of surface topography of biological specimens at high resolution by scanning tunnelling microscopy,” *Nature*, vol. 315, pp. 253–254, May 1985.
- [96] E. Shapir, H. Cohen, A. Calzolari, C. Cavazzoni, D. A. Ryndyk, G. Cuniberti, A. Kotlyar, R. D. Felice, and D. Porath, “Electronic structure of single DNA molecules resolved by transverse scanning tunnelling spectroscopy,” *Nature Materials*, vol. 7, pp. 68–74, Jan. 2008.
- [97] E. Shapir, L. Sagiv, N. Borovok, T. Molotski, A. B. Kotlyar, and D. Porath, “High-resolution STM imaging of novel single G4-DNA molecules,” *The Journal of Physical Chemistry B*, vol. 112, no. 31, pp. 9267–9269, 2008.
- [98] S. M. Lindsay and M. Philipp, “Can the scanning tunneling microscope sequence DNA?,” *Genetic Analysis: Biomolecular Engineering*, vol. 8, pp. 8–13, Feb. 1991.
- [99] D. D. Dunlap, R. García, E. Schabtach, and C. Bustamante, “Masking generates contiguous segments of metal-coated and bare DNA for scanning tunneling microscope imaging,” *Proceedings of the National Academy of Sciences of the USA*, vol. 90, no. 16, pp. 7652–7655, 1993.
- [100] S. Chang, J. He, A. Kibel, M. Lee, O. Sankey, P. Zhang, and S. Lindsay, “Tunnelling readout of hydrogen-bonding-based recognition,” *Nature Nanotechnology*, vol. 4, pp. 297–301, May 2009.
- [101] W. M. Heckl and G. Binnig, “Domain walls on graphite mimic DNA,” *Ultramicroscopy*, vol. 42-44, pp. 1073–1078, July 1992.
- [102] Y. Gan, W. Chu, and L. Qiao, “STM investigation on interaction between superstructure and grain boundary in graphite,” *Surface Science*, vol. 539, pp. 120–128, Aug. 2003.

- [103] J. P. Veazey, G. Reguera, and S. H. Tessmer, “Filament-like artifacts on graphite.” under review, 2011.
- [104] K. Xu, P. Cao, and J. R. Heath, “Scanning tunneling microscopy characterization of the electrical properties of wrinkles in exfoliated graphene monolayers,” *Nano Letters*, vol. 9, pp. 4446–4451, Dec. 2009.
- [105] N. Biais, D. L. Higashi, J. Brujić, M. So, and M. P. Sheetz, “Force-dependent polymorphism in type IV pili reveals hidden epitopes,” *Proceedings of the National Academy of Sciences of the USA*, vol. 107, pp. 11358–11363, June 2010.
- [106] S. Knutton, R. K. Shaw, R. P. Anantha, M. S. Donnenberg, and A. A. Zorgani, “The type IV bundle-forming pilus of enteropathogenic *Escherichia coli* undergoes dramatic alterations in structure associated with bacterial adherence, aggregation and dispersal,” *Molecular Microbiology*, vol. 33, no. 3, pp. 499–509, 1999.
- [107] A. A. Kornyshev, D. J. Lee, S. Leikin, and A. Wynveen, “Structure and interactions of biological helices,” *Reviews of Modern Physics*, vol. 79, no. 3, p. 943, 2007.
- [108] S. Choudhary and A. K. Gupta, “Spatially varying super-lattice structures and linear fringes on graphite surface,” *Journal of Physics: Condensed Matter*, vol. 20, no. 22, p. 225008, 2008.
- [109] J. P. Veazey, S. Lampa-Pastirk, G. Reguera, and S. H. Tessmer, “Microbial nanowire electronic structure probed by Scanning Tunneling Microscopy.” in preparation, 2011.
- [110] I. Ron, I. Pecht, M. Sheves, and D. Cahen, “Proteins as solid-state electronic conductors,” *Accounts of Chemical Research*, vol. 43, pp. 945–53, July 2010.
- [111] W. Paranchych, P. Sastry, L. Frost, M. Carpenter, G. Armstrong, and T. H. Watts, “Biochemical studies on pili isolated from *Pseudomonas aeruginosa* strain PAO,” *Canadian Journal of Microbiology*, vol. 25, no. 10, pp. 1175–1181, 1979.
- [112] D. W. Keizer, C. M. Slupsky, M. Kalisiak, A. P. Campbell, M. P. Crump, P. A. Sastry, B. Hazes, R. T. Irvin, and B. D. Sykes, “Structure of a pilin monomer from *Pseudomonas aeruginosa*. Implications for the assembly of pili,” *J. Biol. Chem.*, vol. 276, pp. 24186–24193, June 2001.
- [113] L. Craig, N. Volkmann, A. S. Arval, Michael E. Pique, M. Yeager, E. H. Engelman, and J. A. Tainer, “Type IV pilus structure by cryo-electron microscopy and crystallography:

- Implications for pilus assembly and functions,” *Molecular Cell*, vol. 23, no. 1, pp. 651–662, 2006.
- [114] L. P. Biró, S. Lazarescu, P. Lambin, P. A. Thiry, A. Fonseca, J. B. Nagy, and A. A. Lucas, “Scanning tunneling microscope investigation of carbon nanotubes produced by catalytic decomposition of acetylene,” *Physical Review B*, vol. 56, p. 12490, Nov. 1997.
- [115] B. Hazes, P. A. Sastry, K. Hayakawa, R. J. Read, and R. T. Irvin, “Crystal structure of *Pseudomonas aeruginosa* PAK pilin suggests a main-chain-dominated mode of receptor binding,” *Journal of Molecular Biology*, vol. 299, pp. 1005–1017, June 2000.
- [116] J. Henrichsen, “Twitching motility,” *Annual Review of Microbiology*, vol. 37, pp. 81–93, Jan. 1983.
- [117] W. Paranchych, P. A. Sastry, K. Volpel, B. A. Loh, and D. P. Speert, “Fimbriae (pili): molecular basis of *Pseudomonas aeruginosa* adherence,” *Clinical and Investigative Medicine*, vol. 9, pp. 113–8, Jan. 1986.
- [118] P. Doig, T. Todd, P. A. Sastry, K. K. Lee, R. S. Hodges, W. Paranchych, and R. T. Irvin, “Role of pili in adhesion of *Pseudomonas aeruginosa* to human respiratory epithelial cells.,” *Infect. Immun.*, vol. 56, no. 6, pp. 1641–1646, 1988.
- [119] W. Folkhard, D. A. Marvin, T. H. Watts, and W. Paranchych, “Structure of polar pili from *Pseudomonas aeruginosa* strains K and O,” *Journal of Molecular Biology*, vol. 149, pp. 79–93, June 1981.
- [120] J. G. Simmons, “Generalized formula for the electric tunnel effect between similar electrodes separated by a thin insulating film,” *Journal of Applied Physics*, vol. 34, pp. 1793–1803, June 1963.
- [121] H. B. Gray and J. R. Winkler, “Heme protein dynamics: Electron tunneling and redox triggered folding,” in *The Porphyrin Handbook* (K. M. Kadish, K. M. Smith, and R. Guilard, eds.), pp. 51, Vol. 11, New York: Academic Press, 2003.
- [122] R. Feenstra, “Electronic states of metal atoms on the GaAs(110) surface studied by scanning tunneling microscopy,” *Physical Review Letters*, vol. 63, pp. 1412–1415, Sept. 1989.

- [123] M. Pomerantz, A. Aviram, R. A. McCorkle, L. Li, and A. G. Schrott, “Rectification of STM current to graphite covered with phthalocyanine molecules,” *Science*, vol. 255, pp. 1115–1118, Feb. 1992.
- [124] J. J. Langer and M. Martynyński, “Nano-scale protonic rectifier,” *Synthetic Metals*, vol. 107, pp. 1–6, Nov. 1999.
- [125] J. J. Langer and M. Martyski, “Protonic nanorectifier: STM imaging,” *Advanced Materials for Optics and Electronics*, vol. 9, pp. 15–18, Jan. 1999.
- [126] S. Sek, K. Swiatek, and A. Misicka, “Electrical behavior of molecular junctions incorporating α -helical peptide,” *The Journal of Physical Chemistry B*, vol. 109, pp. 23121–4, Dec. 2005.
- [127] A. Stamouli, J. W. M. Frenken, T. H. Oosterkamp, R. J. Cogdell, and T. J. Aartsma, “The electron conduction of photosynthetic protein complexes embedded in a membrane.,” *FEBS letters*, vol. 560, pp. 109–14, Feb. 2004.
- [128] A. M. Kuznetsov and J. Ulstrup, “Mechanisms of molecular electronic rectification through electronic levels with strong vibrational coupling,” *The Journal of Chemical Physics*, vol. 116, no. 5, p. 2149, 2002.
- [129] L. P. Nielsen, N. Risgaard-Petersen, H. Fossing, P. B. Christensen, and M. Sayama, “Electric currents couple spatially separated biogeochemical processes in marine sediment,” *Nature*, vol. 463, pp. 1071–1074, Feb. 2010.
- [130] M. Y. El-Naggar, G. Wanger, K. M. Leung, T. D. Yuzvinsky, G. Southam, J. Yang, W. M. Lau, K. H. Nealson, and Y. A. Gorby, “Electrical transport along bacterial nanowires from *Shewanella oneidensis* MR-1,” *Proceedings of the National Academy of Sciences of the USA*, vol. 107, pp. 18127–18131, Oct. 2010.
- [131] M. Morita, T. Ohmi, E. Hasegawa, M. Kawakami, and M. Ohwada, “Growth of native oxide on a silicon surface,” *Journal of Applied Physics*, vol. 68, no. 3, p. 1272, 1990.
- [132] MTI Corporation (www.mtixtl.com).
- [133] J. Taylor, M. Brandbyge, and K. Stokbro, “Theory of rectification in four wires: The role of electrode coupling,” *Physical Review Letters*, vol. 89, no. 13, p. 138301, 2002.

- [134] L. P. Biro, P. A. Thiry, P. Lambin, C. Journet, P. Bernier, and A. A. Lucas, "Influence of tunneling voltage on the imaging of carbon nanotube rafts by scanning tunneling microscopy," *Applied Physics Letters*, vol. 73, pp. 3680–3682, Dec. 1998.
- [135] N. García, C. Ocal, and F. Flores, "Model theory for scanning tunneling microscopy: Application to Au(110)(1x2)," *Physical Review Letters*, vol. 50, pp. 2002–2005, June 1983.
- [136] E. DiMasi, M. Aronson, J. Mansfield, B. Foran, and S. Lee, "Chemical pressure and charge-density waves in rare-earth tritellurides," *Physical Review B*, vol. 52, pp. 14516–14525, Nov. 1995.
- [137] R. Patschke and M. G. Kanatzidis, "Polytelluride compounds containing distorted nets of tellurium," *Physical Chemistry Chemical Physics*, vol. 4, pp. 3266–3281, July 2002.
- [138] C. Malliakas, S. J. L. Billinge, H. J. Kim, and M. G. Kanatzidis, "Square nets of tellurium: rare-earth dependent variation in the charge-density wave of RETe₃ (RE = rare-earth element)," *Journal of the American Chemical Society*, vol. 127, pp. 6510–1, May 2005.
- [139] W. Tremel and R. Hoffmann, "Square nets of main-group elements in solid-state materials," *Journal of the American Chemical Society*, vol. 109, pp. 124–140, Jan. 1987.
- [140] E. DiMasi, B. Foran, M. C. Aronson, and S. Lee, "Quasi-two-dimensional metallic character of Sm₂Te₅ and SmTe₃," *Chemistry of Materials*, vol. 6, pp. 1867–1874, Oct. 1994.
- [141] N. Ru and I. Fisher, "Thermodynamic and transport properties of YTe₃, LaTe₃, and CeTe₃," *Physical Review B*, vol. 73, Jan. 2006.
- [142] V. Brouet, W. Yang, X. Zhou, Z. Hussain, N. Ru, K. Shin, I. Fisher, and Z. Shen, "Fermi surface reconstruction in the CDW state of CeTe₃ observed by photoemission," *Physical Review Letters*, vol. 93, Sept. 2004.
- [143] C. D. Malliakas and M. G. Kanatzidis, "Divergence in the behavior of the charge density wave in RETe₃ (RE = rare-earth element) with temperature and RE element," *Journal of the American Chemical Society*, vol. 128, pp. 12612–3, Oct. 2006.
- [144] W. Lin, H. Steinfink, and E. J. Weiss, "The phase equilibria and crystal chemistry of the rare earth group VI systems. III. Neodymium-Tellurium," *Inorganic Chemistry*, vol. 4, pp. 877–881, June 1965.

- [145] B. K. Norling and H. Steinfink, “The crystal structure of Neodymium tritelluride,” *Inorganic Chemistry*, vol. 5, pp. 1488–1491, Sept. 1966.
- [146] A. Tomic, Zs. Rak, J. P. Veazey, C. D. Malliakas, S. D. Mahanti, M. G. Kanatzidis, and S. H. Tessmer, “Scanning tunneling microscopy study of the CeTe₃ charge density wave,” *Physical Review B*, vol. 79, p. 085422, Feb. 2009.
- [147] A. Tomic, *Scanning Tunneling Microscopy of Complex Electronic Materials*. PhD thesis, Michigan State University, 2008.
- [148] Y. Iyeiri, T. Okumura, C. Michioka, and K. Suzuki, “Magnetic properties of rare-earth metal tritellurides RTe₃ (R=Ce,Pr,Nd,Gd,Dy),” *Physical Review B*, vol. 67, p. 144417, Apr. 2003.
- [149] H. Kim, C. Malliakas, A. Tomić, S. Tessmer, M. Kanatzidis, and S. Billinge, “Local atomic structure and discommensurations in the charge density wave of CeTe₃,” *Physical Review Letters*, vol. 96, p. 226401, June 2006.